Advanced Wavefront Control with Linear and Nonlinear Metasurfaces

A thesis submitted for the degree of

Doctor of Philosophy of

The Australian National University

Lei Wang

汪磊

Nonlinear Physics Centre,
Research School of Physics and Engineering

April 2018

Australian National University

Declaration

This thesis is an account of research undertaken in the Nonlinear Physics Centre within the Research School of Physics and Engineering at the Australian National University between Oct 2013 and Oct 2017 while I was enrolled for the Doctor of Philosophy degree.

The research has been conducted under the supervision of Prof. Yuri Kivshar, Dr. Sergey Kruk and Prof. Dragomir Neshev. However, unless specifically stated otherwise, the material presented within this thesis is my own original work.

None of the work presented here has ever been submitted for any degree at this or any other institution of learning.

10th April 2018

Publications

Journal Publications

The publications mentioned in this thesis are marked with an $*$

1. Sergey Kruk, Alexander Poddubny, **Lei Wang**, Alexey Slobozhanyuk, Daria Smirnova, Alexander Shorokhov, Ivan Kravchenko, Barry Luther-Davies, and Yuri Kivshar. ***Nonlinear light generation from nanoscale topological edge states***. Nature Nanotechnology 14, 126–130, Dec 2018.

2. $*$ **Lei Wang**, Sergey Kruk, Kirill Koshelev, Ivan Kravchenko, Barry Luther-Davies, and Yuri Kivshar. ***Nonlinear wavefront control with all-dielectric metasurfaces***. Nano Letters,18(6):3978-3984, May 2018.

3. $*$ Sergey S. Kruk, Rocio Camacho-Morales, Lei Xu, Mohsen Rahmani,Daria A. Smirnova, **Lei Wang**, Hark Hoe Tan, Chennupati Jagadish,Dragomir N. Neshev, and Yuri S. Kivshar. ***Nonlinear optical magnetismrevealed by second-harmonic generation in nanoantennas***.Nano Letters,17(6):39143918, May 2017.

4. $*$ **Lei Wang**, Sergey Kruk, Lei Xu, Mohsen Rahmani, Daria Smirnova, Alexan-der Solntsev, Ivan Kravchenko, Dragomir Neshev, and Yuri Kivshar. ***Shaping the third-harmonic radiation from silicon nanodimers***.Nanoscale, 9(6):22012206, 2017.

5. $*$ **Lei Wang**, Sergey Kruk, Hanzhi Tang, Tao Li, Ivan Kravchenko, Dragomir N.Neshev, and Yuri S. Kivshar. ***Grayscale transparent metasurface holograms***. Optica, 3(12):1504, Dec 2016.

6. $*$ R. Camacho-Morales, M. Rahmani, S. Kruk, **Lei Wang**, L. Xu, D.A.Smirnova, A.S. Solntsev, A. Miroshnichenko, H.H. Tan, F. Karouta, S. Nau-reen, K. Vora, L. Carletti, C. De An-

gelis, C. Jagadish, Y.S. Kivshar, andD.N. Neshev. ***Nonlinear generation of vector beams from AlGaAs nanoantennas***. Nano Letters, 16(11):71917197, 2016.

7. ∗ **Lei Wang**, A.S. Shorokhov, P.N. Melentiev, S. Kruk, M. Decker, C. Helgert,F. Setzpfandt, A.A. Fedyanin, Y.S. Kivshar, and D.N. Neshev. ***Multipolar third-harmonic generation in fishnet metamaterials***.ACS Photonics,3(8):14941499, 2016.

8. ∗ Katie E. Chong, **Lei Wang**, Isabelle Staude, Anthony R. James, Ja-son Domin-guez, Sheng Liu, Ganapathi S. Subramania, Manuel Decker,Dragomir N. Neshev, Igal Brener, and Yuri S. Kivshar. ***Efficient polarization-insensitive complex wavefront control using huygens' metasurfaces based on dielectric resonant meta-atoms***.ACS Photonics, 3(4):514519, Mar 2016

Media Release

1. ***Grayscale transparent metasurface holograms***. Optica, 3(12):1504,(2016) is highlighted in ***Metasurfaces: Efficient holograms*** . Nature Photonics 11, 76 (2017). This work is also reported by ABC news Star Wars-style holograms one step closer to being in the palm of your hand

2. ***Shaping the third-harmonic radiation from silicon nanodimers*** is selected as the 2017 "hot article" on Nanoscale

Conference Publications

The conference presentation that I performed is marked with ∗.

1. ∗ **Lei Wang**, A. Shorokhov, P. Melentiev, S. S. Kruk, M. Decker, C. Helgert,F. Setzpfandt, A. Fedyanin, Y. Kivshar, and D. N. Neshev, ***Multipolar analysis of the third harmonic radiation pattern from fishnet metamaterials***, in Nonlinear Photonics, pp. NW3A4, Optical Society of America,2016.

2. ∗ **Lei Wang**, S. S. Kruk, M. Rahmani, Y. Kivshar, and D. N. Neshev, ***Nonlinear beam shaping with Si nanodisks***, in Non-

linear Photonics, pp. NW3A2,Optical Society of America, 2016.

3. R. Camacho-Morales, M. Rahmani, S. Kruk, **Lei Wang**, L. Xu, A. Miroshnichenko, D. Smirnova, H. Tan, F. Karouta, S. Naureen,et al., ***Shaping the radiation pattern of second-harmonic generation from AlGaAs nonlinear nanoantennas***, in Nonlinear Photonics, pp. JW6A5, Optical Society of America, 2016.

4. K. E. Chong, **Lei Wang**, I. Staude, S. Kruk, A. James, J. Dominguez, G. S.Subramania, M. Decker, I. Brener, D. N. Neshev, et al.,***Highly-efficient polarization insensitive holograms based on dielectric metasurfaces***, in CLEO: QELS Fundamental Science, pp. FTh1D1, Optical Society of America, 2016.

5. K. Chong, **Lei Wang**, I. Staude, A. James, J. Dominguez, G. Subramania,S. Liu, M. Decker, D. N. Neshev, I. Brener,et al., ***Highly-efficient all-dielectric huygens' surface holograms (conference presentation)***, in Meta-materials X, vol. 9883, p. 988308, International Society for Optics andPhotonics, 2016.

6. $*$ **Lei Wang**, A. S. Shorokhov, P. N. Melentiev, S. Kruk, M. Decker, C. Helgert,F. Setzpfandt, A. A. Fedyanin, Y. S. Kivshar, and D. N. Neshev, ***Multipolar origin of the third harmonic generation from fishnet metamaterials***,in CLEO: QELS Fundamental Science, pp. FW4A2, Optical Society of America, 2016.

7. S. S. Kruk, **Lei Wang**, K. Wang, M. Parry, H.-P. Chung, H. Tao,I. I. Kravchenko, A. Sukhorukov, D. N. Neshev, and Y. S. Kivshar, ***All-dielectric transparent metasurfaces for holography and quantum tomography (conference presentation)***, in Active Photonic Platforms IX,vol. 10345, p. 1034529, International Society for Optics and Photonics,2017.

8. $*$ **Lei Wang**, S. S. Kruk, H. Tang, T. Li, I. Kravchenko, D. Neshev, andY. Kivshar, ***Highest efficiency grayscale all-dielectric meta-holograms***, in Lasers and Electro-Optics Europe & European Quantum Electronics Conference (CLEO/Europe-EQEC, 2017 Conference on), pp. 11, IEEE, 2017.

9. ∗ **Lei Wang**, L. Xu, S. S. Kruk, D. A. Smirnova, D. Neshev, andY. Kivshar, ***Nonlinear mirror with all-dielectric metasurface***, in Lasers and Electro-Optics Europe & European Quantum Electronics Conference(CLEO/Europe-EQEC, 2017 Conference on), p. CD 4 3, Optical Society of America, 2017.

10. M. d. R. C. Morales, M. Rahmani, S. S. Kruk, **Lei Wang**, L. Xu, D. A.Smirnova, A. S. Solntsev, A. E. Miroshnichenko, H. H. Tan, F. Karouta,et al., ***Highly directional second-harmonic generation from AlGaAs nanopar-ticles (conference presentation)***, inNonlinear Optics and Applications X,vol. 10228, p. 102280H, International Society for Optics and Photonics,2017.

11. D. N. Neshev, S. S. Kruk, M. Rahmani, M. del Rocio Camacho-Morales,**Lei Wang**, L. Xu, D. Smirnova, A. S. Solntsev, and Y. S. Kivshar, ***Nonlinear frequency conversion with all-dielectric nanoantennas (conference presentation)***, in Metamaterials, Metadevices, and Metasystems 2017, vol. 10343,p. 103430H, International Society for Optics and Photonics, 2017.

12. M. d. R. C. Morales, M. Rahmani, S. S. Kruk, **Lei Wang**, L. Xu, D. A.Smirnova, A. S. Solntsev, A. E. Miroshnichenko, H. Tan, F. Karouta,et al.,***Directional second harmonic generation from AlGaAs nanoantennas (conference presentation)***, in Metamaterials, Metadevices, and Metasystems2017, vol. 10343, p. 103430J, International Society for Optics and Photon-ics, 2017.

13. M. Rahmani, S. Kruk, R. Camacho-Morales, L. Xu, **Lei Wang**, A. Mirosh-nichenko, D. Smimova, H. Tan, F. Karouta, S. Naureen,et al., ***Giant enhancement and control of second-harmonic radiation from AlGaAs nanoantennas***, in Lasers and Electro-Optics Pacific Rim (CLEO-PR), 2017 Conference on, pp. 13, IEEE, 2017.

14. S. S. Kruk, L. Xu, R. Camacho-Morales, M. Rahmani, **Lei Wang**, D. A.Smirnova, G. Zhang, H. H. Tan, C. Jagadish, Y. S. Kivshar, et al., ***Magnetic vs electric second-harmonic generation from***

AlGaAs nanoantennas,in Lasers and Electro-Optics (CLEO), 2017 Conference on, pp. 12, IEEE,2017.

15. S. S. Kruk, **Lei Wang**, H. Tang, B. Hopkins, A. Miroshnichenko, T. Li,I. Kravchenko, D. Neshev, and Y. Kivshar, ***Broadband transparent all-dielectric metasurfaces***, in CLEO: QELS Fundamental Science,pp. FTu3G3, Optical Society of America, 2017.

To the ones loved me & I loved

Acknowledgments

I would like express my greatest gratitude to all the people who have contributed to the success of my doctoral research. Thank you Prof. Yuri Kivshar for supporting me throughout the difficult times, providing guidance, foresight and precious opportunities. His optimism and inspiration eased up the anxiety. I really appreciate Dr. Sergey Kruk for his heroic efforts to lead the way by example, with goal-orientated decision-making and real knowledge out of practice, on the thorny road of honor in physics researching. Prof. Dragomir Neshev introduced me to ANU and his excellent management of the laboratory is also of great importance for the success execution of vital experiments.

I wish to thank Dr. Lei Xu and Dr. Daria Smirnova for their contribution in theories and as pioneers for the programming that enabled the numerical calculations of nonlinear optics. Lei Xu's patient explanations allowed me to gradually be able to perform numerical calculations with COMSOL multiphysics, which paves the way to further improvements of the intelligent simulation method. Prof David Powell, Dr. Mingkai Liu, and Dr. Sergey Kruk all give useful suggestions regarding the CST studio for simulations in linear optics. Mr Kirill Koshelev also contributed with theories and inspiring discussions.

Another key person is Ivan Kravchenko from Oak Ridge National Laboratory in the US who kindly helped us for silicon nano fabrication that produced robust samples for measurements. Barry Luther-Davies from Laser Physics Centre, ANU provides the nice opportunity for us to use his prototype femtosecond tunable lasers that extend our ability for broadband spectra resolved measurements.

I acknowledge financial support from the Australian Research Council (ARC), scholarship support from the Australian National University.

And above all, I wish to thank my mother Yujian Zhao 赵坚玉 and father Zhiqun Wang 汪智群.

Abstract

Metasurfaces offer unique opportunities for functional flat optics and allow controlling the transmission, reflection, and polarization of light. In particular, all-dielectric resonant metasurfaces have reached remarkable efficiencies and performances. The meta-atoms based on generalized Huygens' principle give flexible full-range phase modulation with nearly no loss. Holographic calculations can carefully map out the spatial arrangement of the meta-atoms and exploit the potential of the metasurface platform for wavefront control. Such advanced and complex wavefront engineering is fully studied and extended to the nonlinear regime, where the nonlinear optical response of metasurfaces opens up new degrees of freedom. This offers a paradigm shift in nonlinear optics. The nonlinear metaholograms are expected to revolutionize subwavelength photonics by enhancing substantially the nonlinear response of natural materials combined with an efficient control of the phase of their nonlinear waves. It is believed that the joint effects of advanced wavefront control in linear and nonlinear optics could eventually lead to integrated photonic computing and nanophotonics quantum circuits.

In this thesis, the development of the nonlinear holographic metasurfaces is presented in a progressive order. In Chapter 1, we provide a comprehensive introduction to the development of metasurfaces, followed by the motivation of creating practical nanophotonic devices. Chapter 2 explains the principles of designing holographic Metasurfaces and phase modulating meta-atoms. We demonstrate a complex wavefront control using the highly efficient polarization-insensitive holographic Huygens' metasurface based on resonant silicon meta-atoms. Moving forward, we demonstrate the transparent meta-holograms based on silicon metasurfaces that allow high-resolution grayscale images to be encoded. The holograms feature the highest diffraction and transmission efficiencies, and operate over a broad spec-

tral range. Chapter 3 explores various types of nonlinear nano-antennas. The multipolar nature of nonlinear resonance is firstly proved by experiment using a nonlinear setup. Our method of optical diagnostics provides a fast and convenient way to acquire the information on materials' nonlinear responses, and it links the nonlinear behaviors of materials to their intrinsic properties. Both numerically and experimentally, the third-harmonic generation (THG) from silicon dimers composed of pairs of two identical silicon nanoparticles demonstrates the multipolar harmonic modes near the Mie resonances that allow shaping of directionality of nonlinear radiation. Efficient control of both electric and magnetic components of light leads to the enhancement of nonlinear effects near electric and magnetic Mie resonances with an engineered radiation directionality. Second harmonic generation (SHG) from III-V based nano-structures reveal that AlGaAs nanodisk antennas can emit second harmonic in preferential direction with a backward-to-forward ratio of up to five, and they can also generate complex vector polarization beams, including beams with radial polarization. We distinguish experimentally the contribution of electric and magnetic nonlinear response by analyzing the structure of polarization states of SHG vector beams. The transition between electric and magnetic nonlinearities is controlled continuously by tuning polarization of an optical pump. Finally, Chapter 4 presents a general theoretical approach and experimental platform for nonlinear wavefront control with highly-efficient nonlinear dielectric metasurfaces. This approach is based on the generalized Huygens' principle extended to nonlinear optics and it allows creating arbitrary phase gradients and wavefronts via excitation of electric and magnetic Mie-resonance multipoles. Based on our concept, we design and demonstrate experimentally the first nonlinear all-dielectric metasurface that generates a third harmonic signal with a high precision in its wavefront control. Multipolar analysis and numerical calculations are performed over a broad pump spectral range with comparisons to the experimental results. Chapter 5 summarizes the key achievements of this work and discusses the future applications based on these results.

Contents

Introduction

1.1 Thesis Statement

Metasurfaces are ultra-thin patterned structures that emerged recently as planar metadevices capable of reshaping and controlling incident light. They are composed of resonant subwavelength elements that are distributed spatially across a surface. Due to resonant scattering, each element can alter the phase, amplitude, and polarization of the incoming light. The ability to perform wavefront control using optical metasurfaces has gained significant attentions in recent years, as it provides a route to ultrathin optics that can potentially replace all bulky optical components. A number of studies have demonstrated the wavefront control capabilities of optical metasurfaces by realizing various flat optical elements, including beam deflectors, beam shapers, flat lenses, and holograms. Metasurface holograms, in particular, represent the ultimate examples of complex wavefront controls, as they can transform an incident plane wave into a desired arbitrary wavefront in the far-field region. All-dielectric resonant nanophotonic structures can substantially lower the absorption losses and drastically enhance the overall efficiency, especially in the transmission regime. Recently, we have seen a number of demonstrations of all-dielectric metasurfaces with ever-increasing transmission efficiencies, in both the near-infrared and visible spectral ranges, including full phase and polarization control. This makes dielectric metasurfaces a promising novel platform for advanced wavefront control.

Nonlinear nanophotonics has attracted a lot of attention due to the fact that a small volume of nanoparticles can create surprisingly strong nonlinear effects. This is at the heart of mod-

ern nanophotonics that aims toward efficient light manipulation at the nanoscale, enabling the design of ultrafast compact optical devices for fully-functional photonic circuitry and advanced metadevices. Nonlinear metasurfaces are expected to meet the growing demand for tailored nonlinear optical response realizing, for example, nonlinear optical chirality, nonlinear geometric Berry phase, and nonlinear wavefront engineering. Several recent pioneering demonstrations of nonlinear metasurfaces for the wavefront control are based on plasmonic designs employing a geometric phase. Different design strategies have been implemented to boost nonlinear performance of plasmonic and hybrid metasurfaces such as resonant coupling of meta-atoms. However, the overall efficiency of the nonlinear frequency conversion in such planar plasmonic nanostructures remained very small, being of the order of 10^{10}.

Dielectric resonant nanostructures have great efficiencies since their optical losses at visible and near-IR wavelengths are almost negligible. Such structures are composed of nanoparticles that can support electric and magnetic Mie-type resonances enabling directional scattering of light by compact optical nanoantennas. For dielectric nanoparticles, nonlinear effects can be enhanced substantially near the resonances which may involve a higher-order multipolar response. Therefore, all-dielectric Mie-resonant nanostructures have recently been suggested as an important pathway to enhance the nonlinear efficiency beyond the limits associated with plasmonics. Indeed, more efficient third-harmonic generation (THG) in individual Si and Ge nanoresonators has been demonstrated recently by several groups showing a huge enhancement of the conversion efficiency by optical pumping in the vicinity of the magnetic dipole Mie resonance. Si and Ge are of a paramount interest for nonlinear photonics as they offer superior nonlinear characteristics while allowing for a potentially low-cost CMOS-compatible fabrication(CMOS stands for Complementary Metal-Oxide-Semiconductor Transistor). Conversion efficiencies of the order of 10^6 have been achieved experimentally in both individual dielectric nanoparticles and all dielectric metasurfaces. These results clearly illustrate the great potential

of all-dielectric resonant nanostructured surfaces for nonlinear nanophotonics and meta-optics.

This thesis aims to explore the advanced wavefront control of metasurfaces in both linear and nonlinear optics. In linear optics, we focus on the all-dielectric resonance phase modulation with generalized Huygens' principle and use holographic methods to realize sophisticated wavefront control with arbitrary complexity as well as being efficient, high in quality and good in performance. In nonlinear optics, we study nonlinear properties from the level of single nanoantennas, and move towards large-scale spatially distributed complex systems. We target the challenge of achieving all-dielectric nonlinear holographic metasurfaces that have strong advantages of efficiencies and phase modulation performances, and may lead to new breakthroughs in quantum optics and photonic computing.

In this chapter, a brief introduction to the development of nanophotonics is given in Section 1.2. In Section 1.3, the scope of the research is explained by showing its potentials in a few key areas of science development. The motivation and outline of the thesis is shown in Section 1.4.

1.2 Nanophotonics and Meta-optics

1.2.1 From Metamaterials to Metasurfaces

Metamaterials come into the view of researchers from early 21st century. They represent a large class of densely packed structured building blocks that are much smaller than the wavelength of the electromagnetic field. From microwave to visible light, studies of subwavelength structures unveiled the Mie-like resonances of these building blocks, opening the door to a world of new possibilities. With the advanced technology of nano fabrications like Focused ion beam (FIB) and Electron beam lithography (EBL), magnetic dipole resonances can be produced by shrinking the size of macroscopic electromagnets such that their resonances enter the optical regime. Examples of metamaterial structures fabricated through composition and periodic repetition of metallic and dielectric elements are illustrated in Figure 1.1;

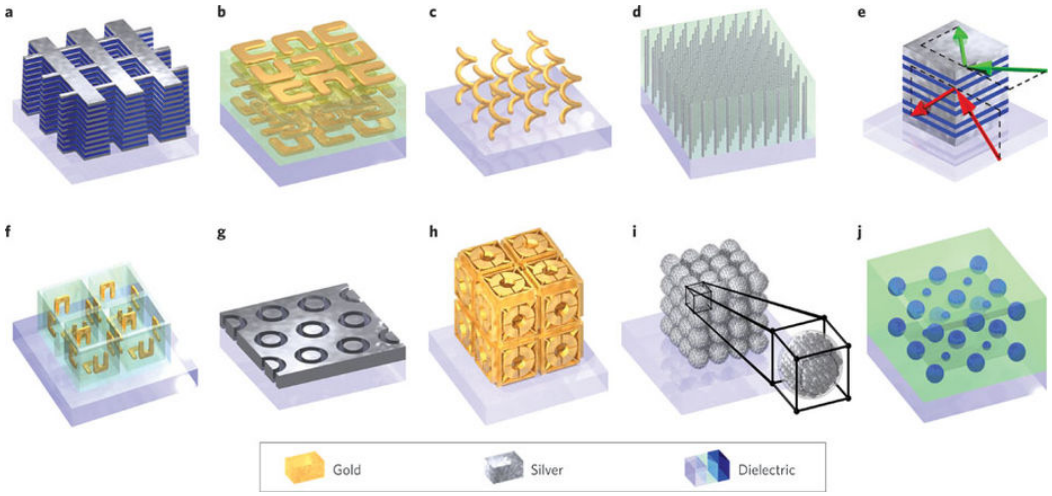

Figure 1.1: Past achievements of three-dimensional photonic metamaterials. Adopted from [1]. a, Double-fishnet negative-index metamaterial with several layers. b, 'Stereo' or chiral metamaterial fabricated through stacked electron-beam lithography c, Chiral metamaterial made using direct-laser writing and electroplating. d, Hyperbolic (or 'indefinite') metamaterial made by electroplating hexagonal-hole-array templates e, Metaldielectric layered metamaterial composed of coupled plasmonic waveguides, enabling angle-independent negative n for particular frequencies. f, SRRs oriented in all three dimensions, fabricated using membrane projection lithography. g, Wide-angle visible negative-index metamaterial based on a coaxial design. h, Connected cubic-symmetry negative-index metamaterial structure amenable to direct laser writing. i, Metal cluster-of-clusters visible-frequency magnetic metamaterial made using large-area self-assembly. j, All-dielectric negative-index metamaterial composed of two sets of high-refractive-index dielectric spheres arranged on a simple-cubic lattice.

Metasurfaces became a logical extension of the metamaterials concept with regards to its practical applications. They are thin-layer subwavelength patterned structures with strong light interaction. Typically with only a single structured layer, metasurfaces benefit from many aspects compared with metamaterials. The simplified physics bring ease to researchers for theoretical analysis and more energy reservation for designing advanced and complex functionalities. Numerical simulations are also easier in terms of computing power requirements. With similar performance or functionalities compared to metamaterials, metasurfaces also enjoy the benefit of faster fabrication and higher success rate as they don't require extreme precision for the multiple exposures, developments and depositions in the multi-layer fabrication process. Metasurfaces will also, when in practical applications, reduce the production cost and increase the robustness of the device. Therefore in recent years, it can be observed that there is a moving trend from metamaterials to metasurfaces for practical nanophotonic devices.

1.2.2 Plasmonic and Dielectric Metasufaces

Metasurfaces, two-dimensional lattices of subwavelength resonators, consist of subwavelength elements (usually called meta-atoms) that can manipulate the lightmatter interaction using a very compact platform. In contrast to conventional optical elements, metasurfaces with spatially varying arrangements of meta-atoms allow control of the polarization, phase, and amplitude of light [2–5], offering unique opportunities for functional flat optics.

Plasmonic metasurfaces are composed of metal elements with strong localized surface plasmon resonances. The coupling of the electromagnetic field to the electron oscillations in the metal plasma allows many ways to manipulate the light. Figure 1.2(a,c,e) show case examples of such plasmonic metasurfaces that are capable of controlling the wavefront of light with ever increasing complexity. However most of the plasmonic devices only have less than 1% efficiency in transmission mode while having better performance in reflection mode. And the ohmic losses, heating and low damage thresholds pose substantial restrictions on

the achievable performance of the plasmonic devices exploiting metallic components. Moreover the localized plasmonic resonance offers only π phase modulation and full 2π phase delay can only be achieved with hybridization of resonance phase and geometric (Berry) phase [6], which requires circular polarized light as input. This requirement will obstuct nanophotonic integrations as most solid state laser diodes produce linear polarized light responding to the crystal axes of its gain medium. The precious metals like gold and silver used in plasmonic metasurfaces will also increase the production cost. Overall the disadvantages of plasmonic metasurfaces greatly limit their application.

All-dielectric metasurfaces have reached remarkable efficiencies, often matching or outperforming conventional optical elements and plasmonic metasurfaces in both transmission and reflection mode [4, 5, 13]. The nanoparticles here are made of high refractive index dielectrics and semiconductors (such as silicon, germanium, tellurium, GaAs, AlGaAs, GaP), which do not suffer from large intrinsic absorption at the visible, infrared and telecom frequencies, are emerging as a promising alternative to plasmonic nanostructures for nanophotonic applications [14,15]. Such high-permittivity nanoparticles exhibit strong interaction with light due to the excitation of the Mie-type resonances they sustain. Both these electric and magnetic resonances can be spectrally controlled and engineered independently, and therefore all-dielectric nanostructures offer unique opportunities for nanophotonics.

1.2.3 Nonlinear Metasurfaces

By now, many phenomena have been demonstrated successfully in linear optics, however, nonlinear metasurfaces are expected to meet the growing demand for tailored nonlinear optical response [16] realizing, for example, nonlinear optical chirality, nonlinear geometric Berry phase, and nonlinear wavefront engineering. Several recent pioneering demonstrations of nonlinear metasurfaces for wavefront control [17–22] were based on plasmonic designs employing a geometric phase. Different design strategies were implemented to boost nonlinear performance of

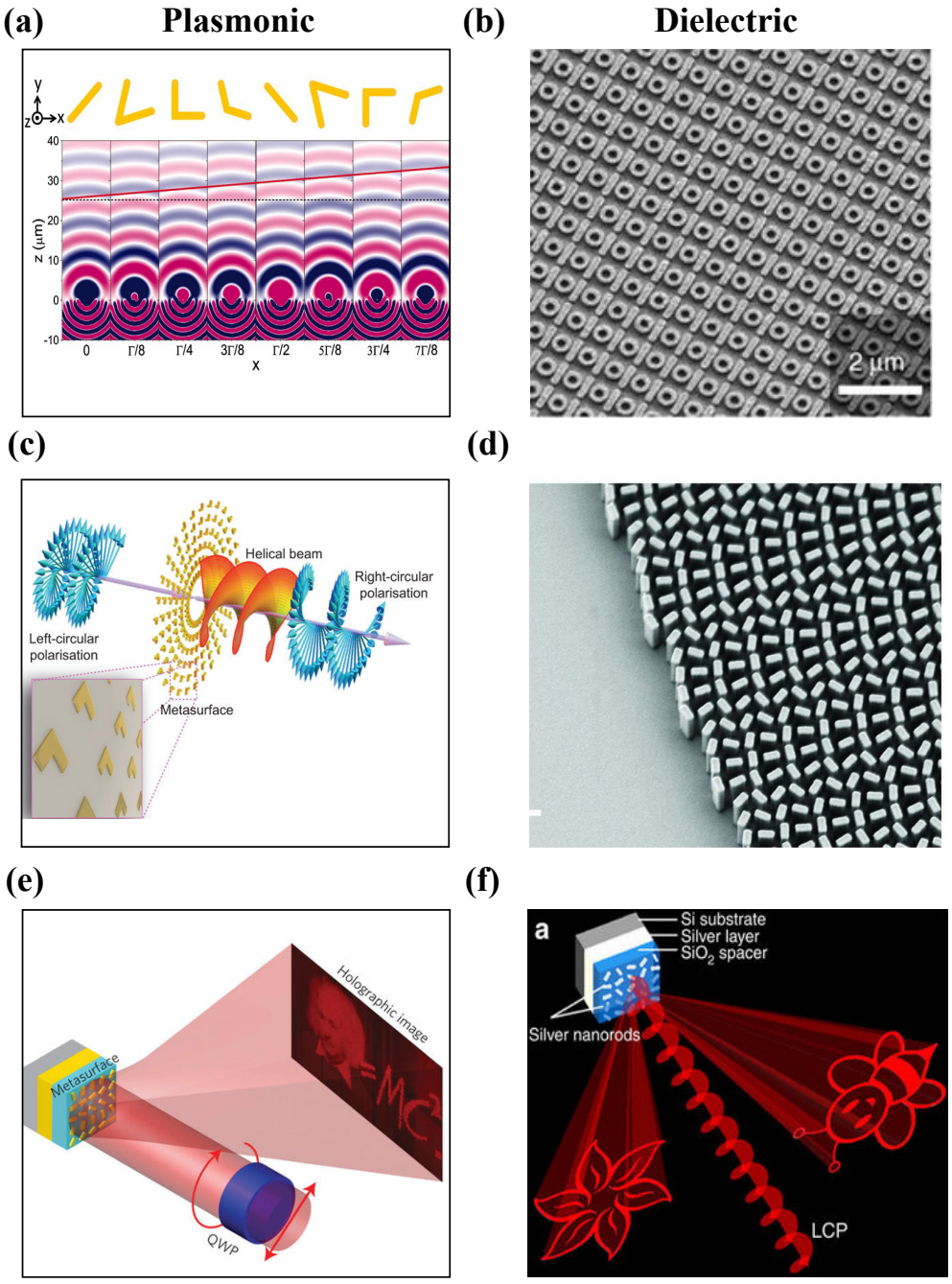

Figure 1.2: Development of metasurfaces. Plasmonic metasurfaces for (a) wavefront control with geometric and resonance phase hybrid [7], (c) polarization control with geometric phase [8], (e) holographic display with geometric phase [9]. Dielectric metasurfaces for (b) high-quality factor (Q-factor) resonances [10], (d) diffraction-limited focusing and subwavelength resolution imaging [11], (f) helicity multiplexed meta-hologram [12].

plasmonic and hybrid metasurfaces [23–25] such as resonant coupling of meta-atoms. Examples of nonlinear plasmonic metasurfaces is shown in Figure 1.3(a,c,e).

All-dielectric Mie-resonant nanostructures have recently been suggested as an important pathway to enhance the nonlinear efficiency beyond the limits associated with plasmonics [30]. Indeed, more efficient THG in individual Si and Ge nanoresonators has been recently demonstrated by several groups, showing a huge enhancement of the conversion efficiency by optical pumping in the vicinity of the magnetic dipole Mie mode or composite resonances [31–33], see Figure 1.3(b,d,f). Si and Ge are of a paramount interest for nonlinear photonics as they offer superior nonlinear characteristics while allowing for a potentially low-cost CMOS-compatible fabrication [34] (CMOS stands for Complementary Metal-Oxide-Semiconductor Transistor). Conversion efficiencies of the order of 10^6 have been achieved experimentally in both individual dielectric nanoparticles and dielectric metasurfaces [35]. These results clearly illustrate the great potential of all-dielectric resonant nanostructured surfaces for nonlinear nanophotonics and meta-optics.

1.3 Research Scope

The research of advanced wavefront control with linear and nonlinear metasurfaces is in frontline of modern science and technology. The ability to arbitrarily control the wavefront can find its application in many fields. Multiplexed optical fiber communications, single fiber endoscope and neural sensor, parallel direct laser writing, spectroscopy, microscopy, hyperspectral imaging, LIDAR (light detection and ranging) and other phased array imaging and so many other technologies that are seeking the advantage of compact and capable metasurfaces for securing the leading position for the future. Here I focus on the potential of photonic computing by combining the wavefront control technique and nonlinear metasurfaces. It is estimated that nanophotonics can contribute to the improvement of clock distribution and communication between computers, creating optoelectronic

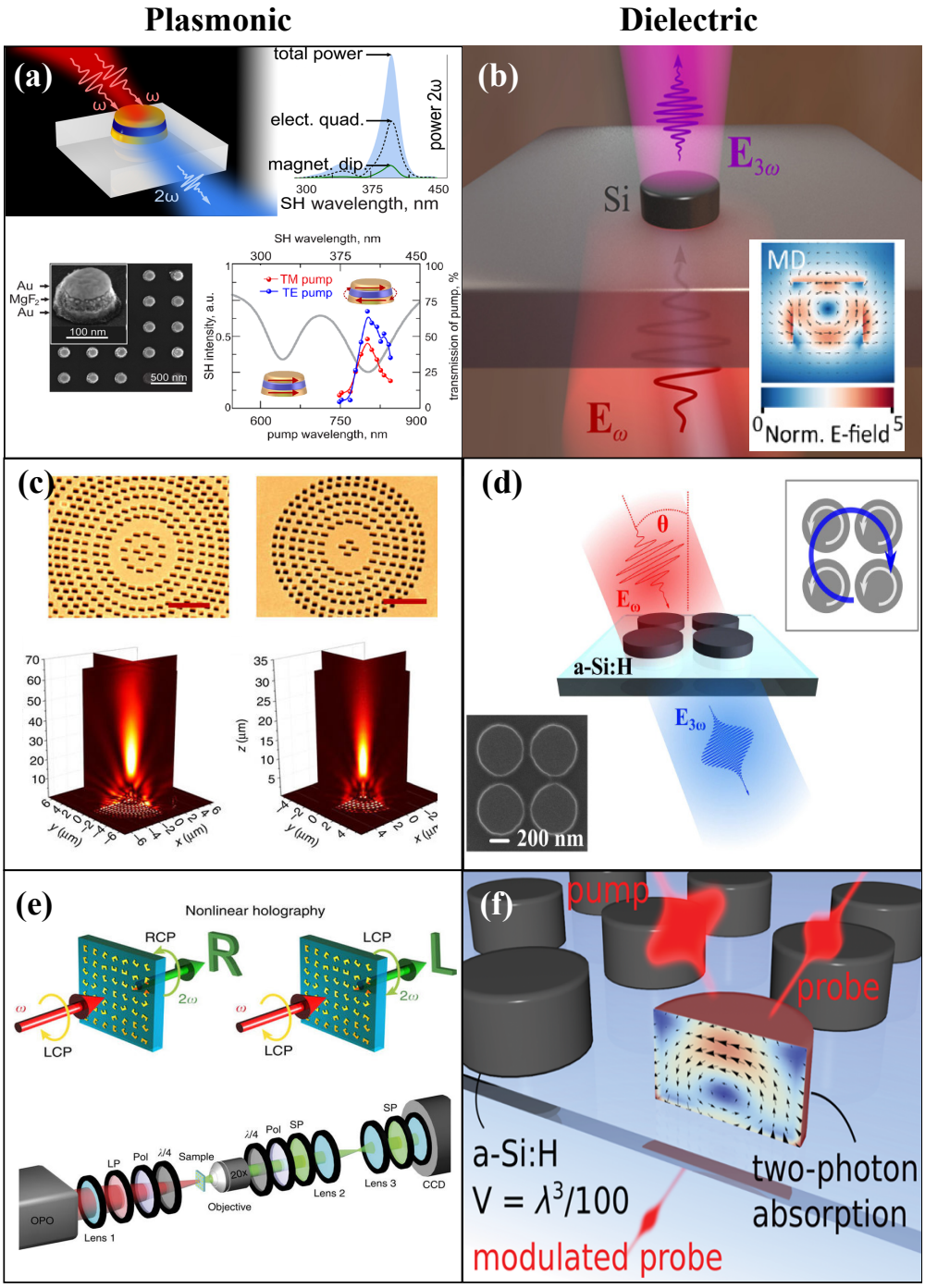

Figure 1.3: Nonlinear Metasurfaces. Plasmonic nonlinear metasurfaces: (a) Study of enhanced SHG with multipole resonance in metal-dielectric-metal nanostructure array [26], (c) nonlinear wavefront control with geometric phase [20], (e) spin and wavelength multiplexed nonlinear metasurface holography with geometric phase [22]. Nonlinear dielectric metasurfaces: (b) Enhanced Third-Harmonic Generation in Silicon Nanoparticles [27], (d) All-dielectric oligomers [28], (f) Optical switching with nonlinear dielectric nanostructures [29].

integrated circuits and in the future, enabling optical quantum computing.

Computers today are growing ever more sophisticated. The key component, microprocessors, are now immensely powerful, capable of executing complex instructions at a faster rate than ever before. More great advances for better computing technology are surely in demand for increasingly globalized societies, yet it is not known if Moores Law can stand up against these unprecedented technical challenges when the dimensions of transistors reach the physics limits. Gate leakage, heat dissipation and higher requirements for fabrication impact the development and from Figure 1.4 we can see the growth has softened since 2006. The continued forward march of microprocessor technology depends as much on pure computing research as it does on cutting edge developments in other fields of science. The engine of microprocessor development in the 21st century may well be the creation of new miniaturization that permit ever more transistors to be placed on a microchip, or innovative forms of computing units that may revolutionize the industry.

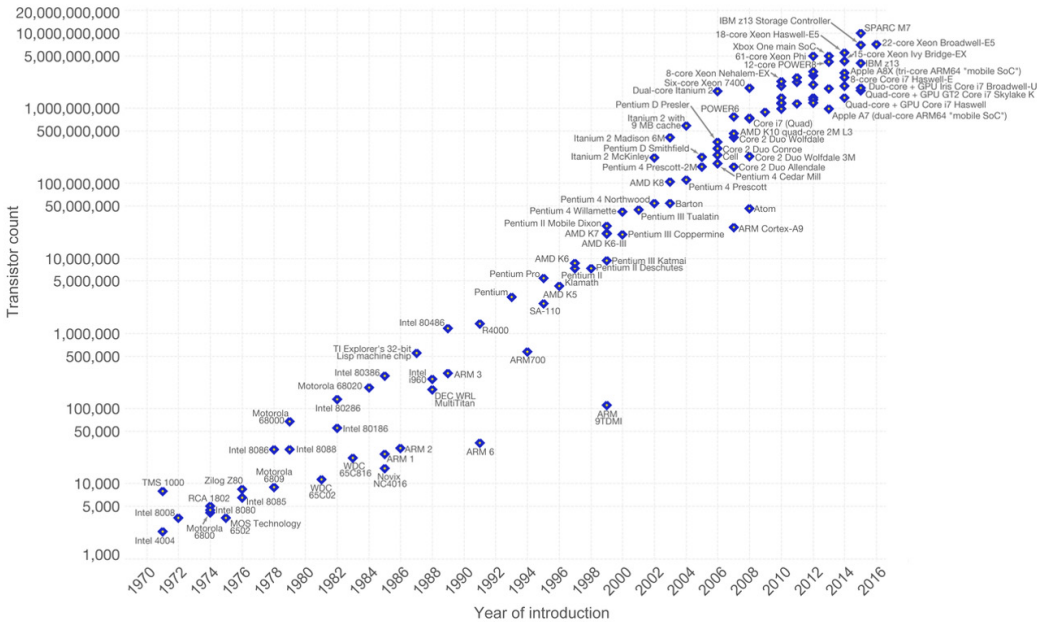

Figure 1.4: The number of transistors on integrated circuit chips.Adopted from [36].

Moore's Law describes the empirical regularity that the number of transistors on integrated circuits doubles approximately every two years. Figure 1.4 shows the statistics of the exponen-

tially growing number of transistors in a log scale plot. Gordon Moore also predicted that chip performance would double every 18 months with a combination effect of more transistors and the transistors being faster. Behind this regularity hide countless science and technologies innovations that researchers strive to achieve from antiquity to the present.

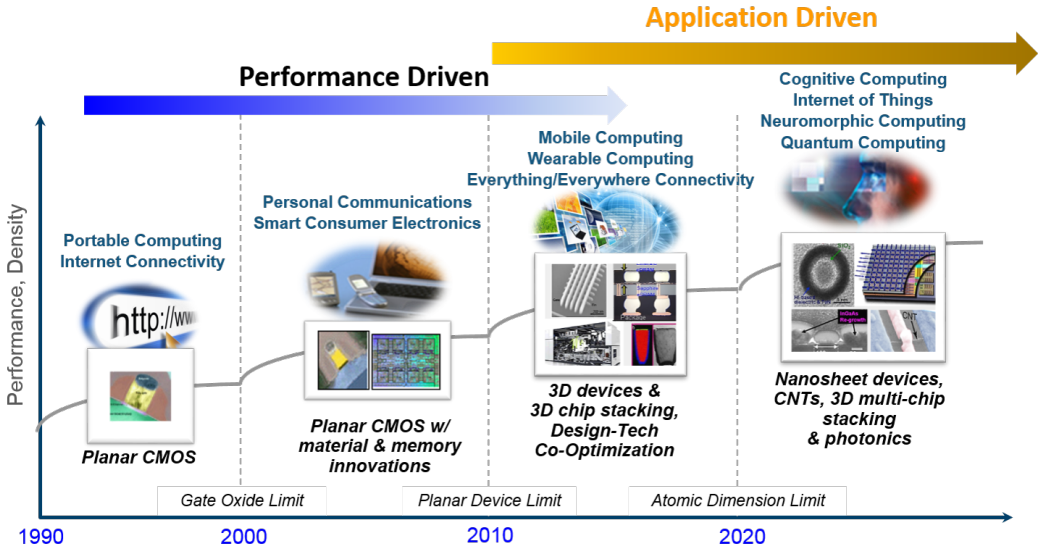

Figure 1.5: Silicon technology scaling. From [37].

The invention of the complementary metal-oxide-semiconductor (CMOS) process by Frank Wanlass in 1963, and a number of advances in CMOS technology by many workers in the semiconductor field since the work of Wanlass, have enabled the extremely dense and high-performance ICs that the industry makes today. The field effect transistor (FET) has been the work horse of modern processors since the 1960s. With scaling to ever smaller dimensions, came the need for process and architecture innovation. Planar FETs had reached the end of its lifespan with need for a dramatic change in device layout, giving way to 3-Dimensional architectures that were first commercialized in 2012 for 22nm technologies. The 3D transistor architectures like finFET from IBM and Tri-gate from Intel keeps up with the Moore's Law, while reducing the leakage and saving power. New materials like SiGe, extreme ultraviolet (EUV) lithography and nanosheet transistors are reported to have contribution in the latest 5nm devices in 2017 Figure 1.5.

Regardless of the increasing cost for the size shrinkage and delicate 3D fine structures for new transistors with reduced gate leakage, performance boost of the electronics will reach the atomic dimension limit, in which the thermal effect and quantum tunneling interrupts the operation. The effective mass of electrons causes gate delays and increases the time for signal propagation, limiting the CPU (Central Processing Unit) clock frequency within the range of GHz. Moreover, heat dissipation become one of the principle limiting factors on computing speed. As the size shrinks, communication wirings between the transistor become denser, yet their resistance increase with narrower cross-sections. The equivalent item to the heat density of a modern CPU chip is ranking up from a nuclear reactor, to a rocket nozzle and going to be similar to the surface of the sun. The long going heat dissipation challenge encourages CPU manufacturers to look into alternative way for inner-chip communication using integrated photonic chips inspired by the success of optical telecommunications.

Conventional computers today transfer data with electrons traveling along electrical links, but researchers hope higher data-transfer speeds can be achieved by sending photons on optical links. Figure 1.6(a) is the close-up photo shows an IBM chip wired up with both electrical and optical links so the inner-chip communication is achieved with photons at high speed (up to 25 Giga bit per second) and low heat generation. ultra-high speed photonic telecommunication is also used between clusters of supercomputers.

However the electron to photon signal conversion will lose up to 30% of the energy. So the researchers keep looking for all-optical computing devices. The fundamental building block of modern electronic computers is the transistor. To replace electronic components with optical ones, an equivalent optical transistor is required. This leads to the significant challenge to optical computing, that computation is a nonlinear process in which multiple signals must interact. Light, which is an electromagnetic wave, can only interact with another electromagnetic wave in the presence of electrons in a material, and the strength of this

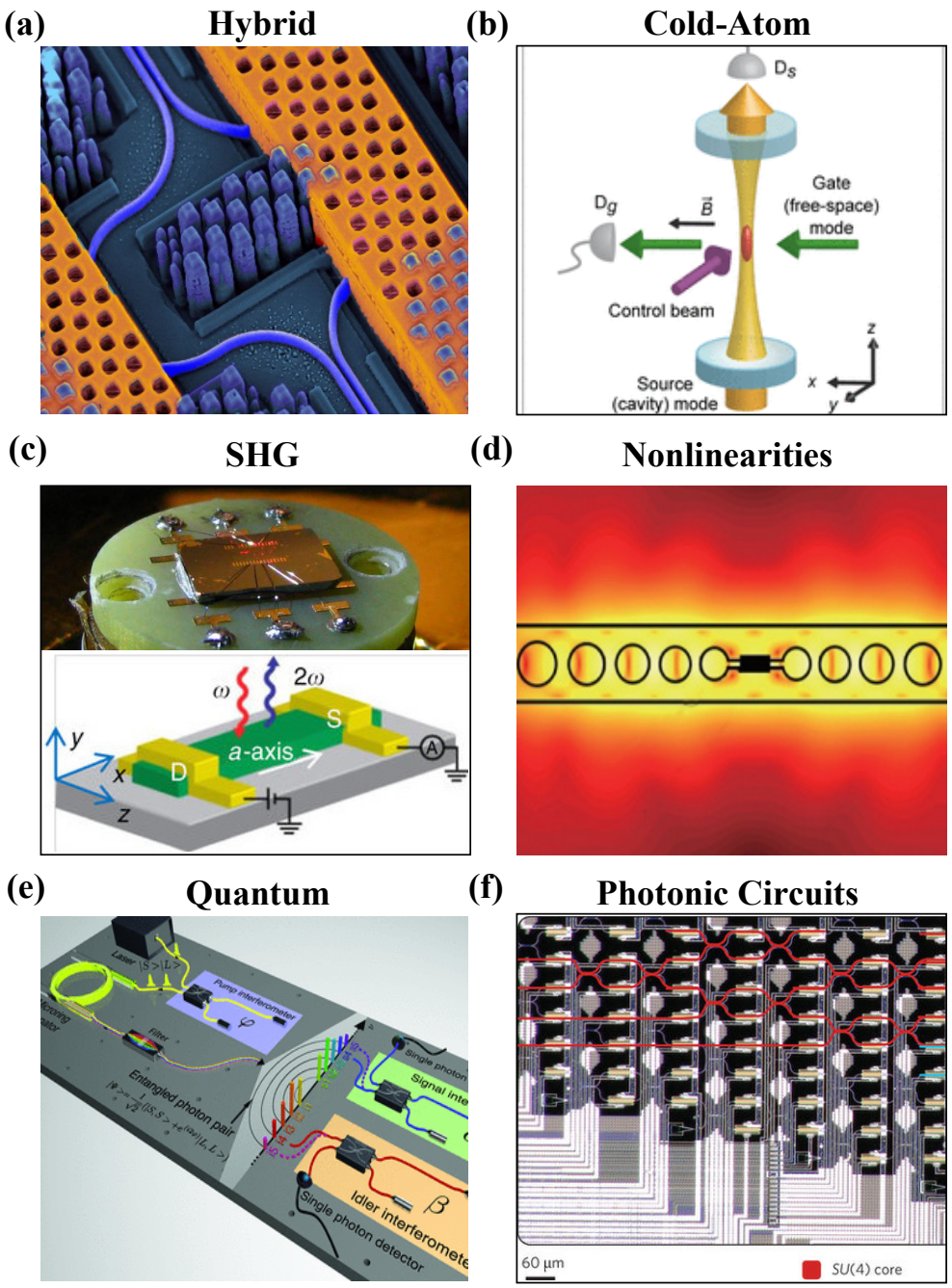

Figure 1.6: Photonic computing. (a) Hybrid photonic chip with both electrical links, shown in yellow, and optical waveguides, shown in blue. (from IBM research) (b) Single photon transistor with cold atom. Adopted from [38]. (c) SHG modulation transistor on CdS, from [39]. (d) Single photon nonlinearities by self similar nanocavity design, picture taken from [40]. (e) Multiphoton entangled quantum states with integrated frequency combs. From [41]. (f) Deep learning with coherent nanophotonic circuits [42].

interaction is much weaker for electromagnetic waves, such as light, than for the electronic signals in a conventional computer. This may result in the processing elements for an optical computer requiring more power and larger dimensions than those for a conventional electronic computer using transistors.

Photonic gates can be achieved using materials with a nonlinear refractive index. In particular, materials where the intensity of incoming light affects the intensity of the light transmitted through the material in a similar manner to the current response of a bipolar transistor. Such an 'optical transistor' can be used to create optical logic gates, which in turn are assembled into the higher level components of the computer's CPU. Figure 1.6(b) [38] shows an all-optical transistor gated by single photon stored by cryogenic cold atoms. Figure 1.6(c) [39] demonstrate high contrast SHG modulation on semiconducting CdS, claimed to be the first optical transistor comparable to electrical ones. Figure 1.6(d) [40] shows the theory of ultrasmall mode volume from self-similar nanocavity design that will allow single-photon second order nonlinearities and possible photonic computing devices.

There is a misconception that since light can travel much faster than the drift velocity of electrons, and photons being weight-less and at frequencies measured in THz, optical transistors should be capable of extremely high frequencies. However, electromagnetic waves obey the transform limit, therefore the response rate of optical transistor is still limited by its spectral bandwidth. In fiber optic communications, practical limits such as dispersion often constrain channels to bandwidths of around 10 GHz, only slightly better than many silicon transistors. Obtaining dramatically faster operation than electronic transistors would therefore require practical methods of transmitting ultrashort pulses down highly dispersive waveguides. In our research we also notice the importance of bandwidth of our linear (Section 2.4) and nonlinear (Section 4.3) meta-hologram devices.

With multi-photon interactions and nonlinearities of metasurfaces, it is plausible to look toward optical quantum computing. For instance, Figure 1.6(e) [41] demonstrate the generation of

multiphoton entangled quantum states by means of integrated frequency combs, which is compatible with existing fiber and semiconductor technology. The results demonstrate a possible scalable and practical platform for quantum technologies.

There are also unconventional approaches to use photonic devices to assist computing. Instead of building a general purpose photonic computer, using photonics to accelerate a certain computing insensitive function in a task or algorithm can be much more practical. One example is using deep learning with coherent nanophotonic circuits to solve the nonlinear activation function in neural network in order to boost deep learning and AI training, see Figure 1.6(f) [42]. There are also reports of various computing problems that can be resolved with clever photonic designs. Optical solution for bounded NP-complete problems like the traveling salesman problem (TSP) is demonstrated in [43]. The power of optics in this method is realized by using a fast matrixvector multiplication between a binary matrix, representing all feasible TSP tours, and a gray-scale vector, representing the weights among the TSP cities. The multiplication is performed optically by using an optical correlator, which compares two signals by utilizing the Fourier transforming properties of a lens. Recently a practical method to optically evaluate a complex-to-complex discrete Fourier transform is achieved by [44]. The research scope is schematically demonstrated in Figure 1.7.

1.4 Thesis Motivation and Outline

The efficient wavefront control of light that combines both linear and nonlinear optic processes may pave the way to functional flat optics, optical telecommunication, photonic computing and optical quantum computing. The motivation of my PhD thesis is to explore the theories and methods for experimental realizations of such advanced wavefront controls in both linear and nonlinear regime with a single device made from all-dielectric metasurfaces. The challenges involved to achieved this goal are listed below.

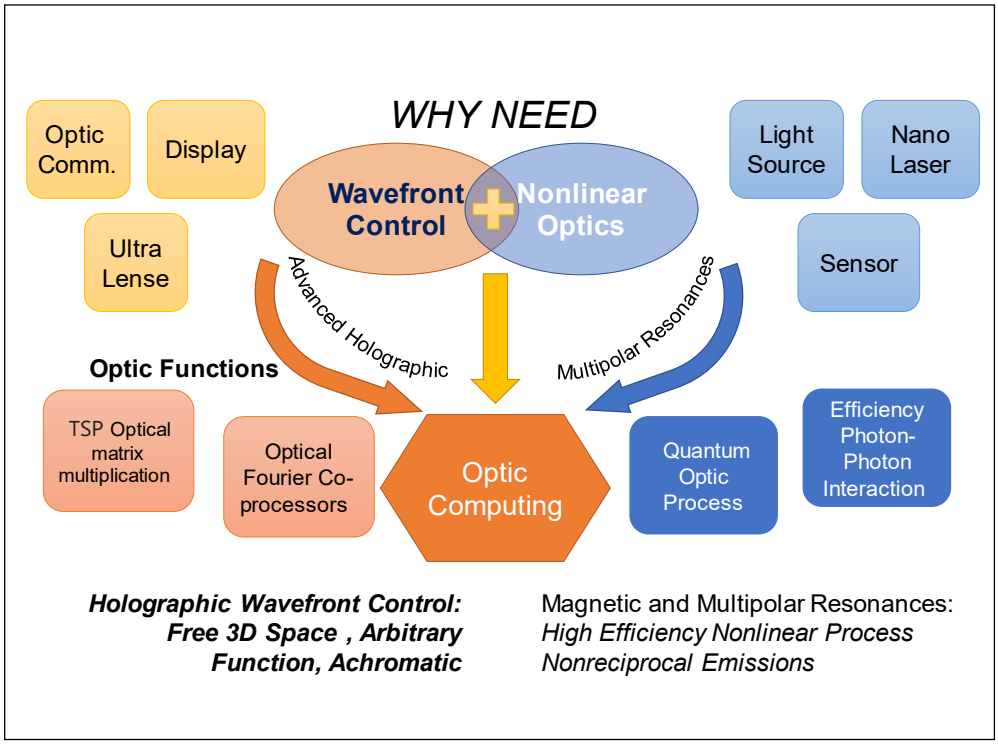

Figure 1.7: Research scope of wavefront engineering and nonlinear optics. We looked into the state of the art wavefront control technology (colored as orange) and the nonlinear optics (colored as blue) in Nano photonics, each of them has proven applications and opportunities for further developments. These two are combined in the research of wavefront control of nonlinear optics, where multipolar resonanced of nano particles are used to realize full range phase control of third harmonic generation and holographic techniques can be implemented in the creation of advanced functionalities towards further possibilities in optic computing.

- How to find the high efficiency phase modulating meta-atoms?
- What is the method for calculating the spatial arrangements of the meta-atoms for specific functionalities?
- How to combine multiple functionalities, such as the efficient nonlinear generation and full-range wavefront control functions, into a single metasurface?
- How to functionalities and accurately perform the numerical simulations for the nonlinear process?
- How to characterize the performance of our linear and nonlinear meta-devices?

In this thesis, we realize an arbitrary wavefront control with metasurface at high efficiency. In Chapter 2, we demonstrate a polarization-insensitive holographic Huygens' metasurface based on dielectric resonant meta-atoms capable of complex wavefront control at telecommunication wavelengths. This metasurface produces a hologram image in the far-field region with 82% transmittance efficiency and 40% imaging efficiency (Section 2.3). Next, we create the transparent meta-holograms (Section 2.4) based on silicon metasurfaces that allow high-resolution grayscale images to be encoded. The holograms feature the highest diffraction and transmission efficiencies demonstrated up to date, and they operate over a broad spectral range. This revolutionary development of generalized Huygens' meta-holograms is demonstrated as the transparent grayscale holographic display that achieved over 90% efficiency at 99% fidelity, which is the highest up to the report date. Such an efficient complex wavefront control shows that generalized Huygens' metasurfaces based on resonant dielectric meta-atoms provide a big step toward practical applications of metasurfaces in wavefront design related technologies. The workflow of designing holographic metasurfaces is explained in Section 2.2.

Then in Chapter 3 the nonlinear properties of nanostructures are studied, and the methods to analyze and modulate the nonlinear resonance and nonlinear radiation pattern, directionality

and polarization states are found out. The multipolar resonance nature of the nonlinear process in metasurfaces are firstly experimentally demonstrated in Section 3.3. Rich information of how to tune the multipolar resonances with all-dielectric dimer nanoantennas is showcased in Section 3.4. The THG from symmetric silicon nanodimers is studied numerically and experimentally to control directionality of the third - harmonic radiation with the multipolar interference effects and near-field enhancement. Effective shaping and switching of the nonlinear third harmonic radiation pattern, its intensity and directionality are achieved successfully. Section 3.2.3 reveals the key component for these experiments, which is the confocal setup I build for back focal plane (BFP) imaging in nonlinear optic measurements. More research in SHG on III-V materials are also conducted using the nonlinear setup as mentioned in Section 3.5.

Finally, in Chapter 4 the wavefront control techniques and the studies of nonlinear nanostructures are combined for the designs of the nonlinear wavefront control in all-dielectric metasurfaces. The platform used in this demonstration is THG from Silicon-on-insulator. We have developed a novel concept of the phase modulation of nonlinear radiation in all-dielectric metasurfaces engineered into functional nonlinear metasurfaces using intelligent designing programs, described in Section 4.2. Theoretic and experimental results including metasurfaces for nonlinear beam deflection at 92% precision, nonlinear special lenses, nonlinear hologram and nonlinear polarization rotations are explained in Section 4.3. This approach is based on the generalized Huygens' principle extended to nonlinear optics, and it allows creating arbitrary phase gradients and wavefronts by excitation of multipoles.

Linear Wavefront Control

2.1 Introduction

The field of holography has gone through several revolutions triggered by new technologies. Initially holographic methods were applied in electron microscopy [45], the invention of lasers brought their practical implementation in optics. The development of computer-generated holography has further advanced this field. And today the next revolutionary step in holographic optics is driven by the enormous progress in our ability to structure materials at the nanoscale. [9, 12, 46–48] Several developments of optical meta-Holograms are reported [9, 49–53] aiming at applications such as holographic displays, data storage, and optical tweezers.

Many metasurfaces to date are based on plasmonic elements that are intrinsically lossy in the optical spectral region due to the absorption in metals. [2, 54]. Although capable of phase control, the efficiencies of the plasmonic devices are usually reported around 1% or avoided mentioning. The large absorption also introduces heating [55] and lowers the damage threshold of the plasmonic devices, therefore making them more suitable for heating [56] instead of optical applications. These issues have triggered a rapid move toward all-dielectric metasurfaces that enable ultrahigh efficiency. Indeed, efficiencies of meta-Holograms that exceed 80% have been demonstrated recently [4, 9]. Most all-dielectric metasurfaces [13, 49, 57–59] utilized what is called geometric phases [60] for wavefront control. The need for the ability to control the optical phase-front in the full range of 0–2π imposes more restrictions on the design parameters of metasurfaces, therefore leading to the introduction of several

undesirable losses, including reflection, diffraction, and cross-polarization conversion losses. The concept of Huygens dielectric metasurfaces [61,62] has proven to be an important advance for achieving full phase control and high transmittance efficiencies.

Huygens metasurfaces rely on the overlap of the electric and magnetic resonances of the high-index dielectric nanoparticles to provide full phase coverage and absorption losses are negligible due to the use of low-loss dielectric materials. Our research team experimentally demonstrated the Huygens' dielectric meta-Hologram [63] that produces an arbitrarily designed hologram image to showcase the complex wavefront control. This device achieved a 82% transmittance efficiency and a 40% diffraction efficiency. The latter value represents the percentage of transmitted light which propagates into the desirable region. It enables a new way to create highly efficient holograms with single-step patterning.

Following up and furthermore, I designed theoretically and realize experimentally the new generation of greyscale transparent meta-holograms [64, 65] with superior performances. We employ the concept of the multi-resonant response based on the generalized Huygens' condition [5]. The hologram is composed of sub-diffraction lattices of high aspect ratio silicon nano-pillars, each supporting several electric and magnetic Mie resonances [66]. The nano-pillars feature a size-dependent phase delay which allows to achieve the 2π phase variations spatially across the hologram with over 2π variation across the operational spectral bandwidth. Based on this principle, we fabricate ultra-high resolution (33600 DPI) meta-holograms and demonstrate experimentally holographic grayscale image display with high efficiency and fidelity. Its transmission efficiency is more than 90% and the diffraction efficiency exceeds 99%, which scores the highest among all the latest development of meta-Holograms. This study can offer practical solutions for a diverse range of efficient wave-shaping applications.

Section 2.2 gives a brief introduction to the numercal calculation method for computer generated holograms (CGH) using the

band-limited angular spectrum method and Gerchberg-Saxton Algorithm. The work in the Section 2.3 showcase the creation of all dielectric meta-Hologram composed of silicon nano-disks. This work is published as [63] and I undertook the task of creating the program code for calculating the phase only masks using the band-limited angular spectrum (BL-AS) method and GerchbergSaxton (GS) algorithm. Section 2.4 demonstated the advanced techniques to design and fabricate transparent meta-hologram with the hightest efficiency reported to date. This is published in paper [64] and reviewed by [65], [67] and etc. I lead this project and am responsible of numerical calculations of the nano pillars, design of the hologram, building up the setup for experiment measurements and its theoretical analysis.

2.2 Theory and Design Methods

Holographic metasurfaces represent the ultimate examples of complex wavefront control. By engineering the subwavelength nanostructures, a complete set of phase modulating elements can be formed to allow full range 2π phase control of its transmission or reflection with great efficiencies. These elements when assembled, can transform arbitrary incident light into any desired output wavefront. Depending on the required functionality, the mapping from input wavefront to the output can be realized by calculating the spatial arrangement of the phase elements. The high performance of the subwavelength phase elements as well as the on-demand flexibility of the holographic method enable the great potential of meta-Holograms in a vast range of optic applications.

The general approach to design meta-Holograms is composed of three steps shown in Figure 2.1. Firstly, an on-demand digitized phase only hologram is calculated using computer generated hologram (CGH) methods. For simplicity a square lattice is used for the 2D spatial distribution where its resolution is related to the lattice constant. The 0-2π phase is also digitized in equal intervals as phase steps marked by an integer label. Another step is to find a suitable set of nanostructures or so called meta-atoms.

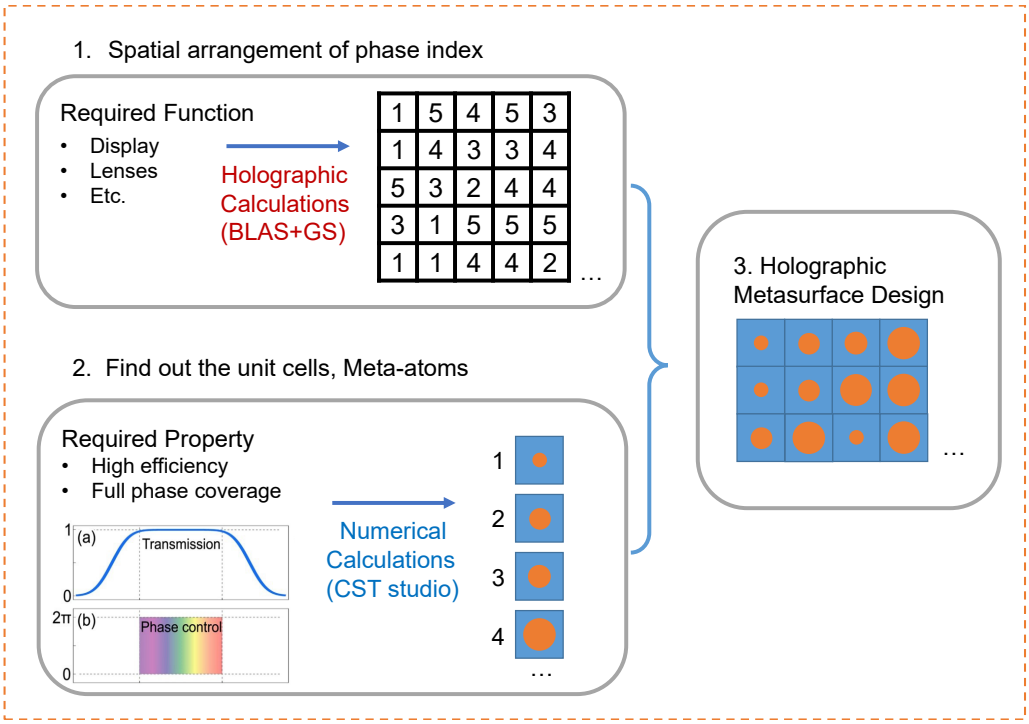

Figure 2.1: (a) Digital holographic calculation for the spatial distribution of the phase elements (phase-mask). (b) Meta-atoms design to realize high transmission (or reflection) and full range phase control among a set of unit cells. (c) Fabrication of the metasurfaces based the phase-mask and the unit cells design.

They are selected as the building blocks of the metasurface. They should fulfill both requirements of uniform and near unity transmission (or reflection, depending on the needs), as well as being able to cover the full phase range. This set of unit-cells are then labeled by the same integers by the matching phase shifting steps they provide. Eventually the meta-Hologram is fabricated as the combined product of the chessboard-like 2D spatial distribution and the designed set of the unit-cells.

2.2.1 Angular Spectrum Method

In our works I utilize the band-limited angular spectrum (BL-AS) method [68] for calculating wave propagation in free space. This method enables fast and accurate numerical calculation for both near field and far field free space propagations. The method can be briefly overviewed by tracking the formula derivation from the Maxwell Equations Eq. (2.1) that describe the classical elec-

tromagnetism and optics.

$$\begin{aligned} \nabla \cdot \mathbf{E} &= \frac{\rho}{\varepsilon_0} \\ \nabla \cdot \mathbf{B} &= 0 \\ \nabla \times \mathbf{E} &= -\frac{\partial \mathbf{B}}{\partial t} \\ \nabla \times \mathbf{B} &= \mu_0 \mathbf{J} + \mu_0 \varepsilon_0 \frac{\partial \mathbf{E}}{\partial t} \end{aligned} \tag{2.1}$$

The Helmholtz equation Eq. (2.2) can be derived from Eq. (2.1) by applying the variables separation technique, which represents a time-independent form of the wave equation.

$$\nabla^2 A + k^2 A = 0 \tag{2.2}$$

Using the mathematical relation known as the Green's Theorem, one of the solutions to the wave equation called the Rayleigh-Sommerfeld formula Eq. (2.3) can be found, where $r' = [(x - x')^2 + (y - y')^2 + z^2]^{1/2}$ and λ is the wavelength. $g(x, y, 0)$ and $g(x, y, z)$ are the complex field distribution at the source plane and the target plane. Figure 2.2.

$$g(x, y, z) = \int\int g(x', y', 0) \frac{exp(i2\pi r' \lambda^{-1})}{r'} \frac{z}{r'} \left(\frac{1}{2\pi r'} + \frac{1}{i\lambda} \right) dx' dy' \tag{2.3}$$

The angular spectrum method is equivalent to the Rayleigh-Sommerfeld formula. [69] The integral can be rewritten in the convolution form with a propagation kernel $h(x, y, z)$,

$$g(x, y, z) = g(x, y, 0) * h(x, y, z) \tag{2.4}$$

where the $*$ denotes 2D convolution with respect to x and y. The kernel is given by Eq. (2.5)

$$h(x, y, z) = \frac{exp(i2\pi r' \lambda^{-1})}{r'} \frac{z}{r'} \left(\frac{1}{2\pi r'} + \frac{1}{i\lambda} \right) \tag{2.5}$$

By applying Fourier Transform on each side of Eq. (2.4) and using the Convolution Theorem, the convolution is rewritten as $G(u, v; z) = G(u, v; 0) H(u, v; z)$. The angular spectrum $G(u, v; 0)$

and transfer function $H(u,v;z)$ are retrieved by Fourier transform of the initial field $g(x,y,0)$ and kernel $h(x,y,z)$. Using $\mathcal{F}$ to represent Fourier transform and $\mathcal{F}^{-1}$ for inverse Fourier transform, the field distribution $g(x,yz)$ at target plane can be calculated as following

$$\begin{aligned} g(x,y,z) &= \mathcal{F}^{-1}\{G(u,v;0)H(u,v;z)\} \\ &= \mathcal{F}^{-1}\{\mathcal{F}[g(x,y,0)]\mathcal{F}[h(x,y,z)]\} \\ &= \mathcal{F}^{-1}\{\mathcal{F}[g(x,y,0)]exp[i2\pi w(u,v)z]\} \end{aligned} \tag{2.6}$$

where $w(u,v)$ is given by

$$w(u,v) = \begin{cases} (\lambda^{-2} - u^2 - v^2)^{1/2} & \cdots u^2 + v^2 \leqslant \lambda^{-2} \\ 0 & \cdots elsewhere \end{cases} \tag{2.7}$$

A carefully calculated band limit is applied to the transfer function $H(u,v;z)$ in order to reduce the numerical errors produced in far field. To speedup calculation, the Fourier transform $\mathcal{F}$ is replaced by Fast Fourier transform (FFT). The overall workflow of the BL-AS method is summarized in Figure 2.2. The accuracy of the BL-AS method is proved applicable to both far field and near field propagation. [68] The Fourier method, or called Fraunhofer diffraction is a simplified method accurate in far field. But it contains error in near-field and near-to-far transaction region. Another simplified method is Fresnel diffraction which is only accurate in near field. These two methods are approximation of RayleighSommerfeld diffraction and FresnelKirchhoff Diffraction. The RayleighSommerfeld diffraction use Fourier transforms and is easier to use here. With band-limited kernel, the method we used here can provide accurate result that cover the whole region from near-field to far-field.

2.2.2 Gerchberg-Saxton Algorithm

The next step is to create the phase-only holograms from the desirable image. For a conventional hologram which has both phase and amplitude modulation, the hologram creation is simply performing a backward propagation $\mathcal{P}(-z)$ using the BL-AS

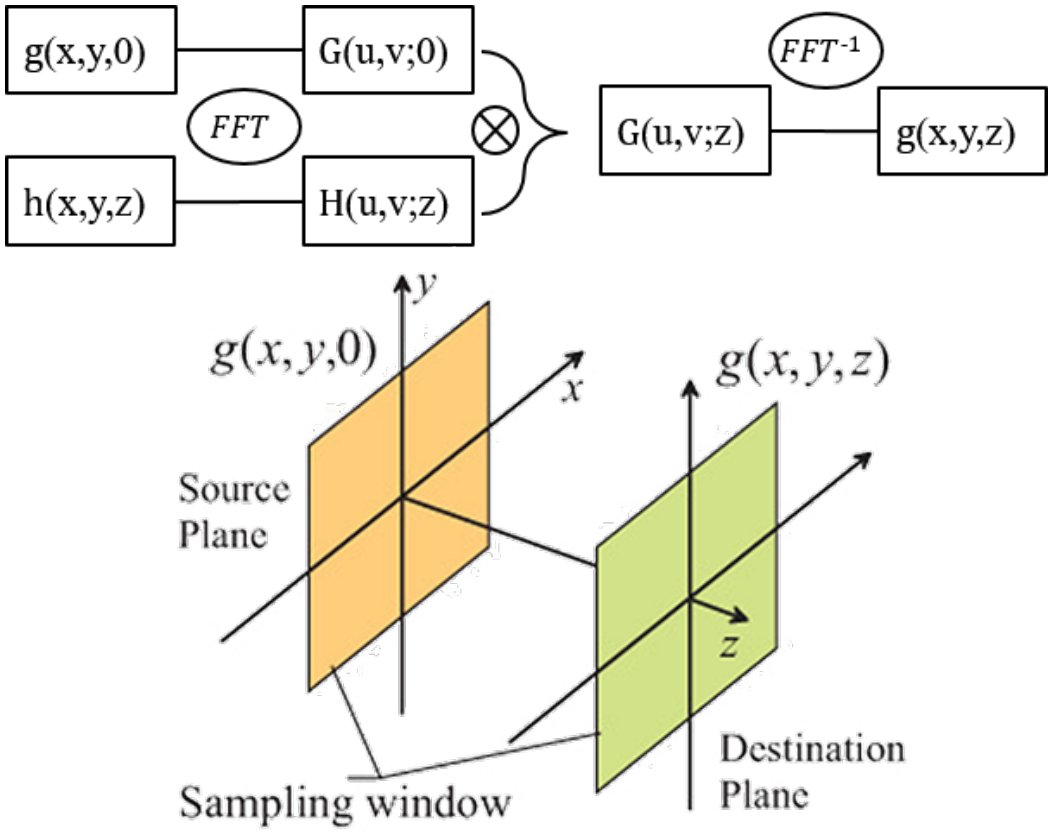

Figure 2.2: The Workflow of the band-limited angular spectrum method .

method. However it is more complex to find the elements that control both phase and amplitude. The other important issue is amplitude modulation will greatly reduce the transmission efficiency of the device. Therefore a method to generate phase-only hologram from given image is an essential part of designing the meta-Hologram.

Figure 2.3 illustrates the Gerchberg-Saxton (GS) algorithm [70] for calculating the phase only holograms. This is an iterative error-reduction method that applies constrains to the amplitude of the complex field $g(x,y,z) = A(x,y,z)exp(i\phi(x,y,z))$ while numerically calculating the forward and backward propagation between the source plane $z = 0$ and the target plane $z = z_1$. It starts with a desirable amplitude at target plane $A_1(x,y,z_1)$ given by the square root of the design image intensity. A_1 is combined with a random phase distribution to form the initial target complex field.

After applying the backward propagation operator $\mathcal{P}(-z_1)$ using the BL-AS method Eq. (2.6), the complex field at the source

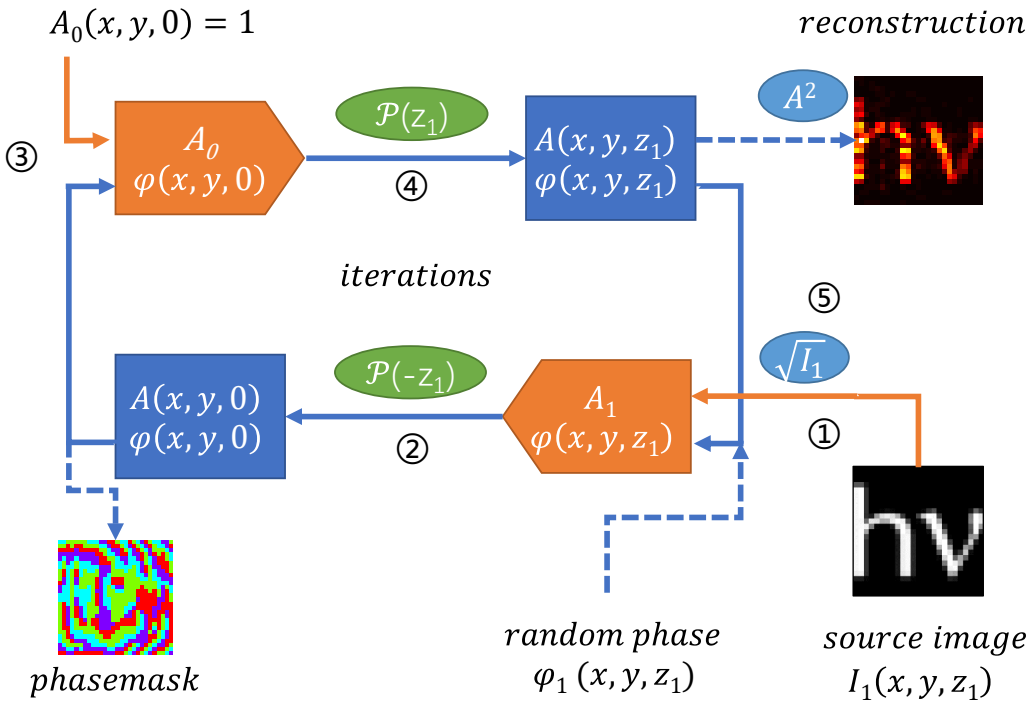

Figure 2.3: Diagram for Gerchberg-Saxton algorithm

plane is calculated and its amplitude is replaced with a uniform amplitude $A_0(x,y,0)=1$. Similarly the constrained source field forward propagate to the target plane by applying operator $\mathcal{P}(z_1)$, and then the amplitude of the target field is enforced with the desirable one A_1. This process continues for several iterations (usually N<50) until the quality of the reconstructed image becomes stable, and the phase at the source plane at the final iteration is extracted to form the phase-only hologram.

In practice the focus spot of a laser beam is used as the source to create the holographic display. So it is better to consider the amplitude distribution of Gaussian beam at beam waist in the source plane. Another constraint of digitized phase levels can also be applied to the iteration in order to limit the total number of phase control elements and simplify the fabrication process. Weighted constrains and many other techniques can be used upon the GS algorithm to further improve the imaging quality, e.g. reducing speckle noise and etc.

In the theory of this design, the incident is a plane wave with no relative phase difference. The plane wave doesnt exist in real life, so a loosely focused Gaussian beam is the best approxima-

tion in experiments as it also has a flat phase profile at the waist. In practice we use a long focal length lens, so it is not very sensitive and is not very difficult to reach the correct position. Moreover the phase shift of metasurface can be adjusted to compensate the phase profile of the incident beam, if certain applications require not at beam waist situations.

The free space act as a low pass filter, so the more distance light propagates, the more information it lost. It is hard to project clear holographic images at very long distance, similarly, it is hard to image details of distant stars, as the radiation is more and more like spherical wave at very long distance. Here we used a proper distant to have a sharp image. Also, the radiation of each meta-atom is considered as spherical waves, but in real life the amplitude might be different at large angles. So here we choose the scale of holographic image and hologram itself so that the maximum angle from hologram to image is within a certain limit.

2.3 Huygens Meta-Hologram

In our work of Huygens Meta-Hologram, we employ silicon nano-disks as meta-atoms for phase control. The array of these nano-disks forms a phase-only hologram which is capable of projecting a lens-less image of letters "*hν*" at given distance, as shown in Figure 2.4

All nano-disks forming the metasurface have the same diameter and the same height and are embedded into a 580 nm thick layer of silicon dioxide (silica). The height of the silicon nano-disks is set to h = 243 nm. The diameter of d = 534 nm has been chosen to tune the electric and magnetic dipole resonances into spectral overlap, which enables a 2π phase shift at the resonance, thereby providing a full range of accessible phase values.

The spatial gradient of transmittance phases in the source plane is obtained by the local variation of the lattice periodicity a. Since a variation of lattice periodicity would lead to a spectral shift of the resonance, the spatial transmittance phases introduced at a particular frequency would then be dependent

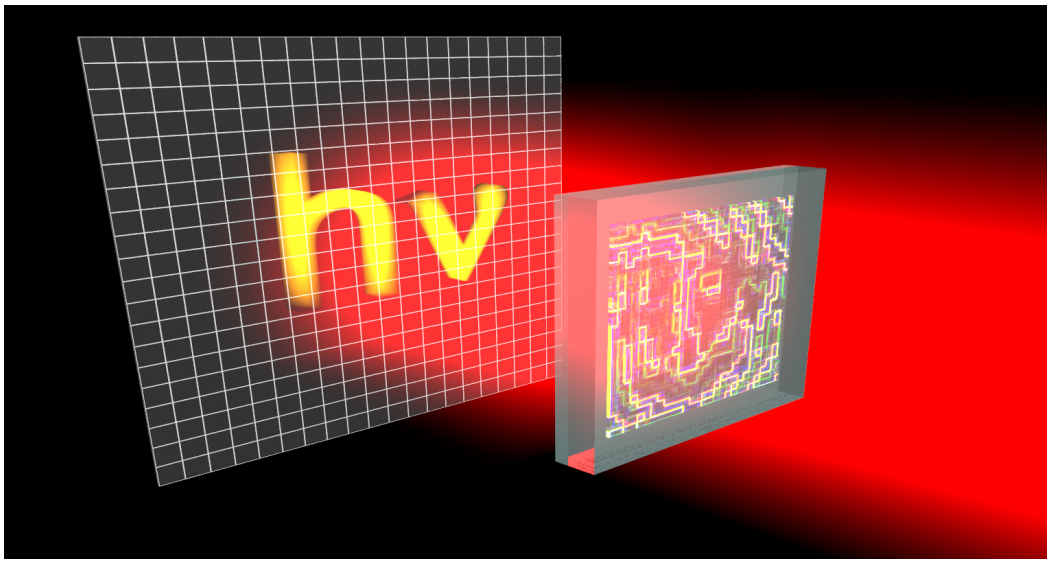

Figure 2.4: Concept image of the Huygens' metasurface hologram. The infrared 1447nm laser passes through the metasurface composed of Huygens' meta-atoms and the phase of the transimited wavefront is modulated to reconstruct a 2D image of letters "*hv*".

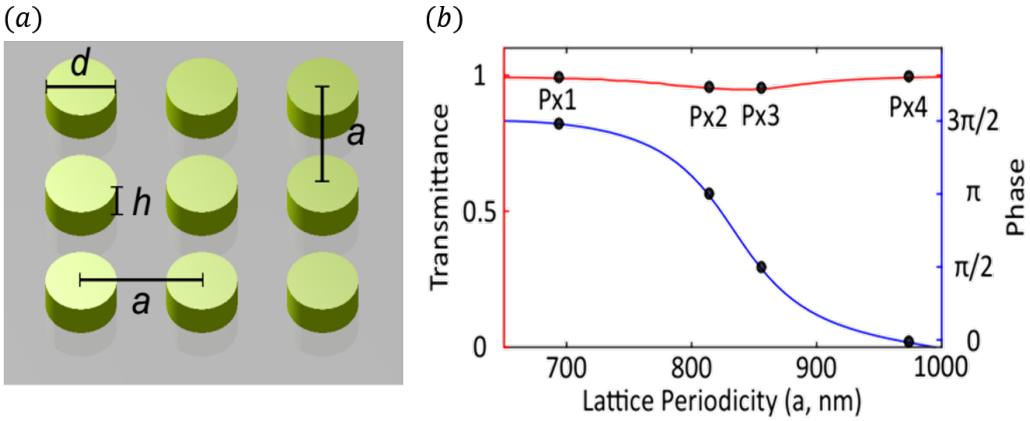

Figure 2.5: (a) Nano-disk array and disk geometry definition. (b) The phase and amplitude of the nanodisk array with fixed disk size and variable lattice period

on the range of lattice periodicity selected. Our operation wavelength of 1477 nm is chosen such that the silicon nanodisk arrays with the selected parameters provide the largest range of transmittance phases for a physically realizable variation of lattice periodicity, as well as the highest transmittance across the same range of lattice periodicity values. Figure 2.5 (b) shows the numerically calculated transmittance intensities and phases of the four optimized silicon nanodisk arrays.

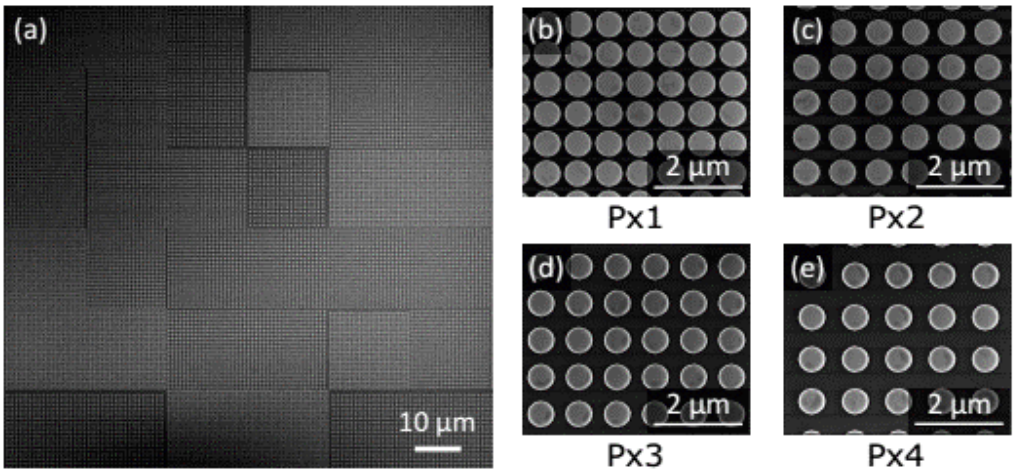

Figure 2.6: SEM image of a part of the metasurface (a) 6x6 pixel area. (b) Examples of 4 types of disk array with different lattice constant to as the four level phase control elements

We use the letter "*hv*" as the desirable image. The four level phase mask is calculated using the methods described in Section 2.2. The phase mask Figure 2.7 (b) is translated into the Silicon nano disk arrays mentioned above and fabricated using electron-beam lithography (EBL). The four phase levels in this case are achieved with period of a_{Px1} = 695 nm, a_{Px2} = 815 nm, a_{Px3}= 855 nm, and a_{Px4} = 975 nm. Each disk array forms a supercell as the pixel for the hologram. The meta-Hologram is composed of 28×28 pixels with pixel size of $17.35 \times 17.35 \mu m$. The SEM pictures of the sample can be seen in Figure 2.6.

The 1447nm laser is illuminating on the sample and the transmitted wavefront is captured by an infrared (IR) camera Figure 2.7 (e), which matches very well with the theoretic prediction Figure 2.7 (c). The phase profile of the sample is also measured using a MachZehnder interferometer setup, shown in Figure 2.7 (f). We define two quality factors to characterize the

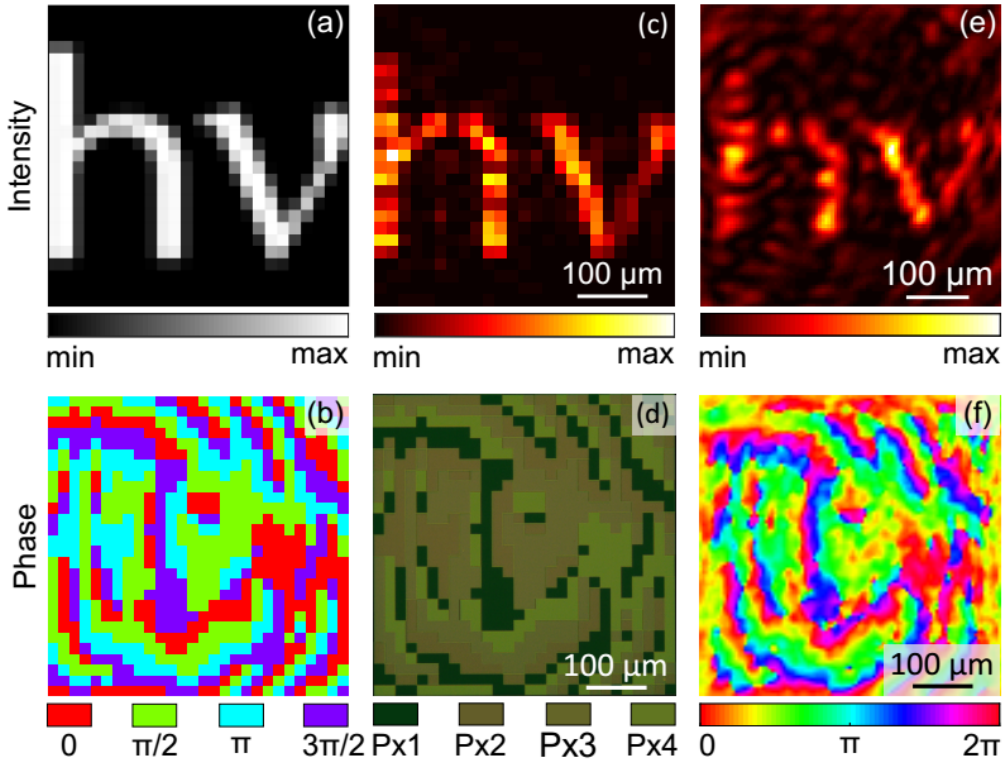

Figure 2.7: Theoretic and experimental results for designing and characterizing the Huygens Meta-Hologram. (a) Desirable image intensity (b) Calculated 4 level phasemask (c) Calculated reconstruction image with 4 phase level hologram (d) sample image in microscope (e) Measured image display (f) Measured phase profile.

performance of our device, the transmission efficiency and the diffraction efficiency. The first term quantifies the transfer efficiency of light after passing through the Meta-Hologram, which can be calculated by dividing the measured light power through the hologram by the light power through a blank substrate of same size. The second term, diffraction efficiency, characterized the ability of the hologram to deliver light into desirable directions. Here it is measured as the ratio of diffracted light power that generate the "*hv*" letters to the total transmitted power. The measured transmission efficiency of this Huygens Meta-Hologram device is over 82% and its diffraction efficiency of around 40%.

In this metasurface, limited by the design of meta-atoms, the phase is tuned by changing the lattice constant. So, each pixel required a small array and the pixel size is not subdiffractional. This also result in low total resolution which will reduce high-frequency information (details of the hologram) to be created. The phase steps are also low. All these factors will reduce the diffraction efficiency, which is seen as the artifacts around the main holographic image. Indeed, here we define the diffraction efficiency as: for the 82% transmitted light, 40% of it is diffracted in directions within the desired image.

2.4 Transparent Meta-Hologram

To further boost the performance. I use the generalized Huygens' principle [5] for selecting phase control elements. This type of high aspect ratio pillars made of high-index Silicon enable phase modulation by individual nanostructure with uniform and near unity transmission. As each pixel only needs one subwavelength nano pillar, they can form an ultra-high resolution hologram. Thus these elements allow for creating transparent meta-Hologram with high fidelity and efficiencies.

The design of the phase elements for the meta-holograms is calculated by numerical simulations with CST Microwave Studio. They are composed of polycrystalline-Silicon (p-Si) nanopillars with height (H) of 865 nm and arranged into a square lattice with a lattice constant (P) of 750 nm. Figure 2.8 (a) shows

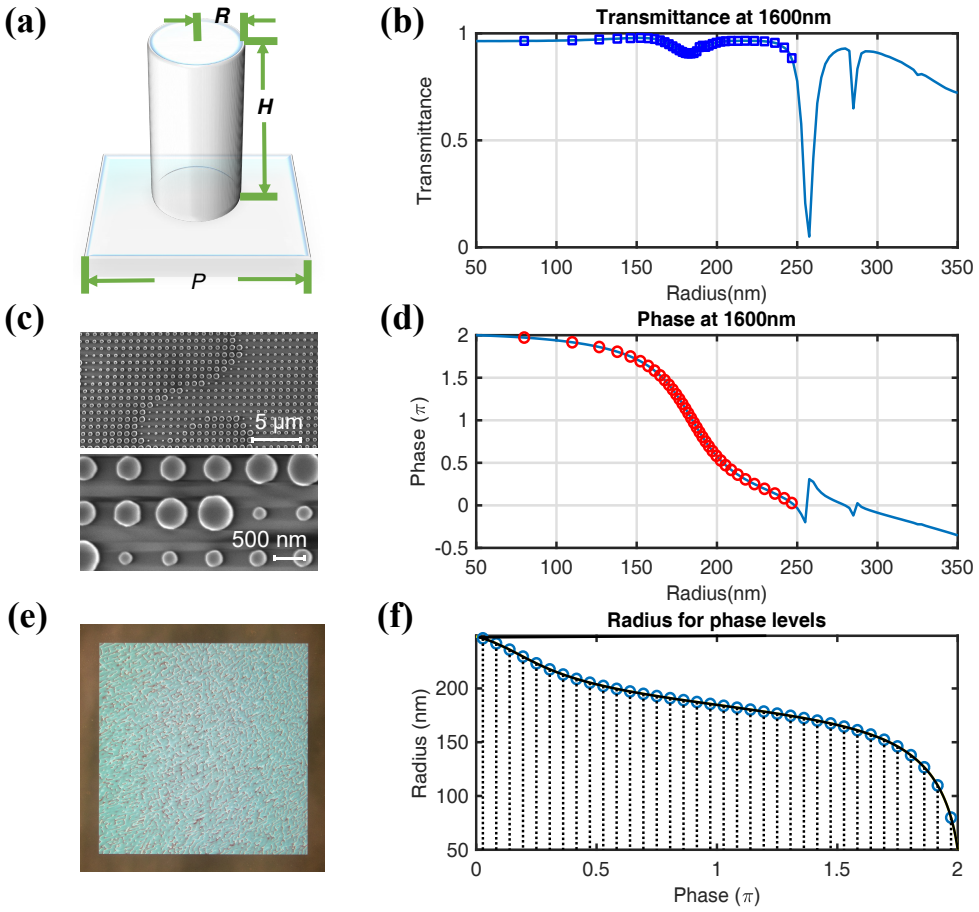

Figure 2.8: Design of the phase elements of the meta-hologram (a) Geometry of the Silicon nano pillar. (c) Scanning electron microscope images of fabricated meta-holograms. (b) Transmittance and (d) Phase shift of the Silicon pillar lattice at 1600nm. Blue Curves are calculated data. Dots are the corresponding values of the selected 36 elements. (e) Visible light dark-field microscope images of a meta-Hologram. This image resembles a layout of the designed phase mask, since the nanopillars of different sizes scatter different visible wavelengths (f) Selected Radii for the 36 step phase levels.

an example of the unit cell. The geometry of the cylindrical pillars are marked by radius=R, height=H, and lattice constant=P. Notice the lattice period is chosen to have weak coupling effect between the lattice neighbors, therefore the periodic boundary condition used in the simulation will best match the actually complex arranged metasurface with periodic lattice but different sized pillars. The transmittance and phase shift vs various radii (R) of the nano pillars in a periodic boundary condition at 1600nm wavelength are calculated. The optical properties of the lattices with various radii are shown in Figure 2.8 (b) transmittance and (d) phase shift. It can be seen that 2π phase shift can be achieved with radii (R) ranging from 79 nm to 212 nm and the transmittance curve is always near unity. These are the key factors to create a high performance phase-only hologram. Another factor is the number of phase levels used in the hologram. Ideally continuous phase can be used but for fabrication a limited number of shapes is preferred. So a total of 36 evenly spaced phase levels are selected as shown in Figure 2.8(f). Each subwavelength nano-pillar can serve as a pixel for the hologram, which allows for ultra-high resolution. The fabricated sample can be viewed in SEM pictures (Figure 2.8(c)) and visible optical microscope image (Figure 2.8).

To demonstrate the capability of the meta-Hologram, the holographic display functionality is presented. The source image can be arbitrary and will easily apply to other cases with minor modifications. Figure 2.9 shows the design of the phase only hologram. Notice the binary source image of Maxwell equations Figure 2.9(a) has more information of its complex shapes and the grayscale source image of kangaroo Figure 2.9(b) has more information in its intensity. The band-limited angular spectrum method and the Gerchberg-Saxton algorithm discussed in Section 2.2 are used to calculated the corresponding phasemasks as shown in Figure 2.9(c) and (d). The BL-AS method can also predict the reconstruction of the images shown in Figure 2.9(e) and (f).

To fabricate the metasurfaces we deposit poly-silicon on a silica wafer with low-pressure chemical vapor deposition. We use

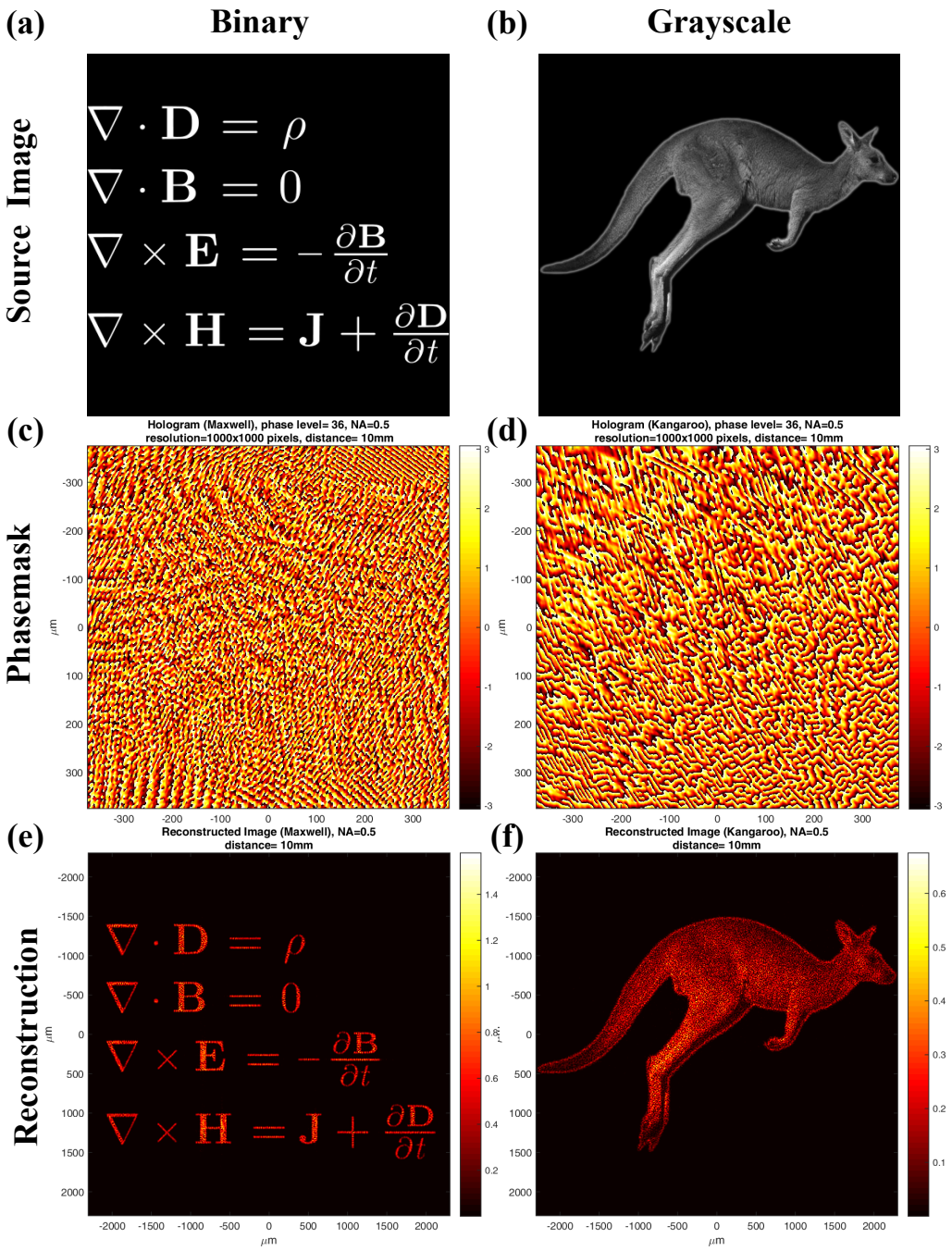

Figure 2.9: Design of the phase-only hologram. (a) Binary (b) and grayscale source images for the display. (c) and (d) Calculated 36 level phasemasks. (e) and (f) Calculated reconstruction

electron beam lithography (EBL) to define the geometry of nanopillars and reactive ion etching to translate the geometry into silicon. These holograms have sizes of 0.75 mm and produce 5 mm large images at a distance of 10 mm. The resolution is 33600 DPI with a million pixels and 36 phase levels. Figure 2.10(a) shows the 3D illustration of a local area of the meta-hologram in bird eye view. With illuminated with an infrared 1600nm laser, the meta-hologram will modulate its wavefront and create a lens-less real space image after propagation of a certain distance. Concept image of the propagation is shown in Figure 2.10(b) that demonstrate the intensity of the beam along the propagation axis.

With the self-imaging property of the holographic display, the experimental measurements is relatively simple. An adjustable mechanic aperture is used as a window between a 4f optic system, matching the incident beam shape to that of the hologram. Two lenses are used to adjust the size of the reconstructed image into suitable size that matches the CCD chip of the IR camera. We experimentally observe holographic images on an infrared camera by illuminating the samples with a collimated laser beam of a matching size. The measured results: second row of Figure 2.10(c) and (d), show good fidelity compared to theory: first row of Figure Figure 2.10 (c) and (d).

Next, we study the operational bandwidth of the meta-holograms in terms of their transmission and diffraction efficiencies. The diffraction efficiency is defined as the power concentrated in the holographic image referenced to the total power transmitted by the hologram. To define the operation bandwidth, we use lasers tunable in the spectral range 1360-1650 nm and perform the same measurements with adjusted focus. Part of the results are shown in Figure 2.11(a) with five specific wavelengths. We also performed numerical study of the transmission and phase spectra versus the radius of nanopillars, shown in Figure 2.12, and calculated the efficiency spectra theoretically. Figure 2.11(c)(d) show the experimentally measured (dots) and numerically calculated spectra (curves) for both transmission and diffraction efficiencies. These results demonstrate that our transparent meta-holograms produce greyscale high-resolution images, and they

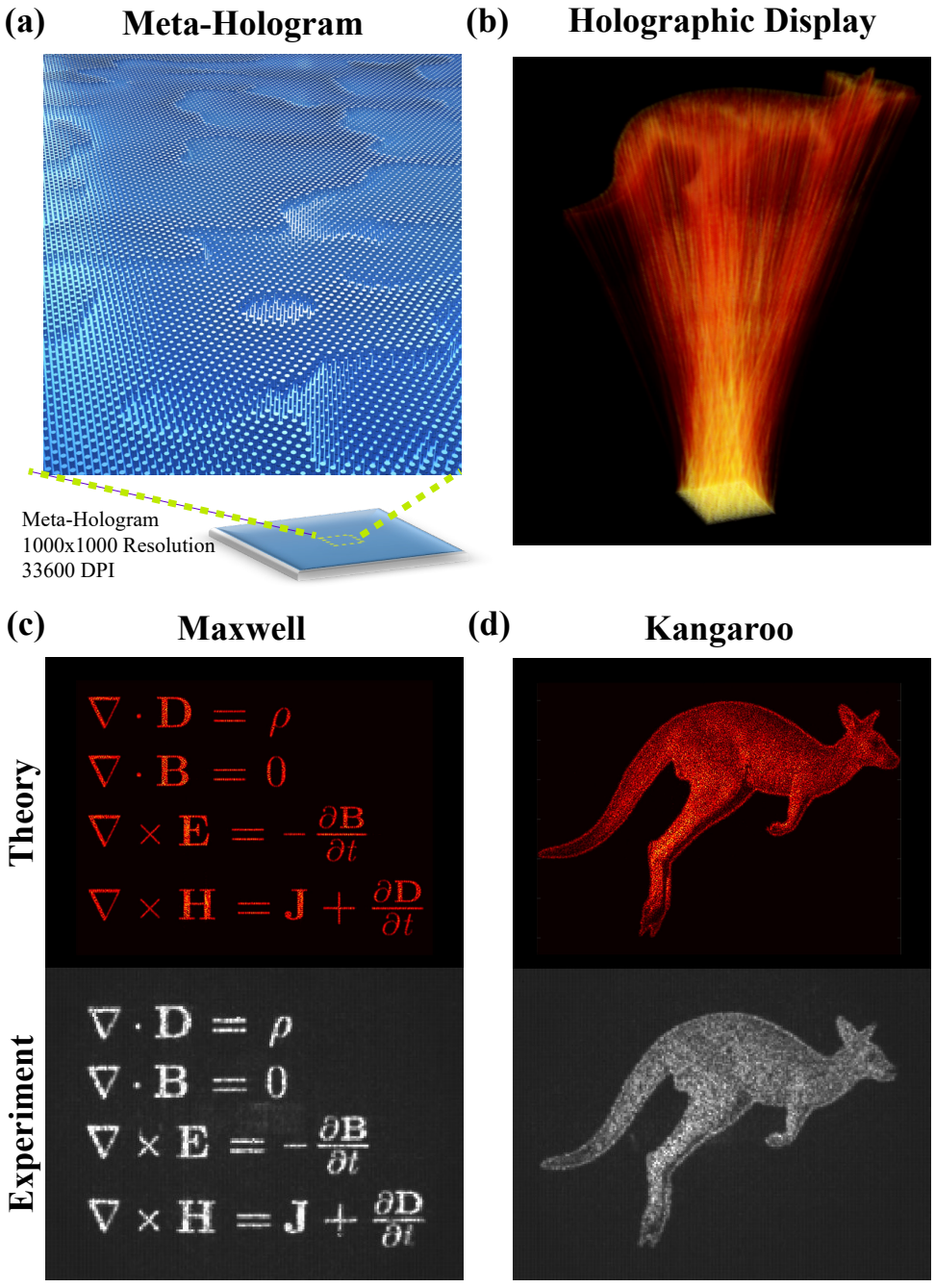

Figure 2.10: Experiment results of the meta-hologram. (a) Detailed local illustration of the meta-Hologram. (b) Concept of the wavefront control and self imaging of the holographic display by numerical calculation of light propagate after the hologram. (c) Theoretical and (d) experimental holographic images from two holographic displays under illumination with the wavelength of 1600 nm.

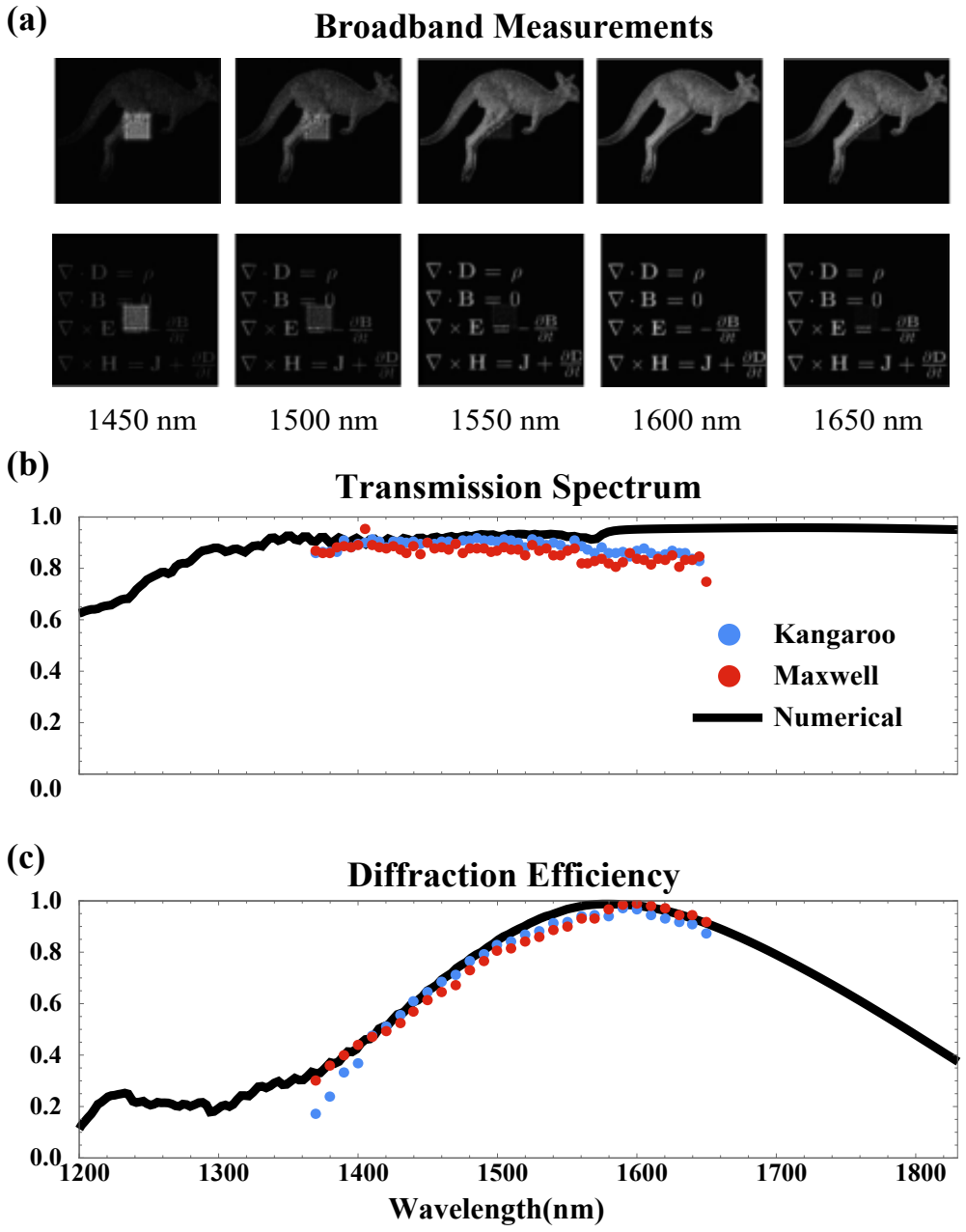

Figure 2.11: Broadband performance. (a) Samples of measured images five specific laser wavelengths. (b) Measured (dots) and numerical calculated (line) transmission spectrum. (c) Diffraction efficiency vs wavelength

transmit over 90% of light with diffraction efficiency over 99% at 1600 nm wavelength. The overall efficiency is above 80% within a 180 nm spectral bandwidth, and it is above 50% within a 360 nm bandwidth. To the best of our knowledge, this is the highest efficiency of any meta-holograms demonstrated up to date which are capable to reproduce greyscale images over a broad spectral range.

The design approach is both scalable to the visible spectral region and potentially compatible with high index materials such as Ge, GaAs, TiO_2 or diamond.

2.5 Summary

All-dielectric resonant nanophotonics [66] can drastically enhance the transmission efficiencies, but so far a majority of demonstrated metasurfaces operate in a narrow frequency range. We established the general approach to create meta-Holograms with all dielectric nano-structures using the Huygens principle. The first attempt described in Section 2.3 [63] proved the design methods with binary image display function for binary images of simple shapes. Then advanced techniques are used in the following work Section 2.4 [64] that demonstrate transparent metasurface holograms allowing encoding of high-resolution greyscale images or complex binary images over a broad spectral range. Our hologram has the highest efficiency reported to date (see Figure 2.13). Composed of subdiffractional resolution phase modulating nanopillars, each single pillar has near unity efficiency, symmetrically shaped and works as one pixel, our metasurface device is a phase-only hologram discretized into abundant phase levels that overcomes common problems of metasurface holograms such as polarization dependence, zero or high order diffraction, low fill factor, twin images and disruptive cross talk.

In this chapter we demonstrated our phase modulating dielectric metasurfaces composed of Silicon nano particles. There are several properties of the Silicon based platform: Highly transparent from near-IR to mid-IR ranges, high refractive index and possibility of convenient industrial adaptation, that might ben-

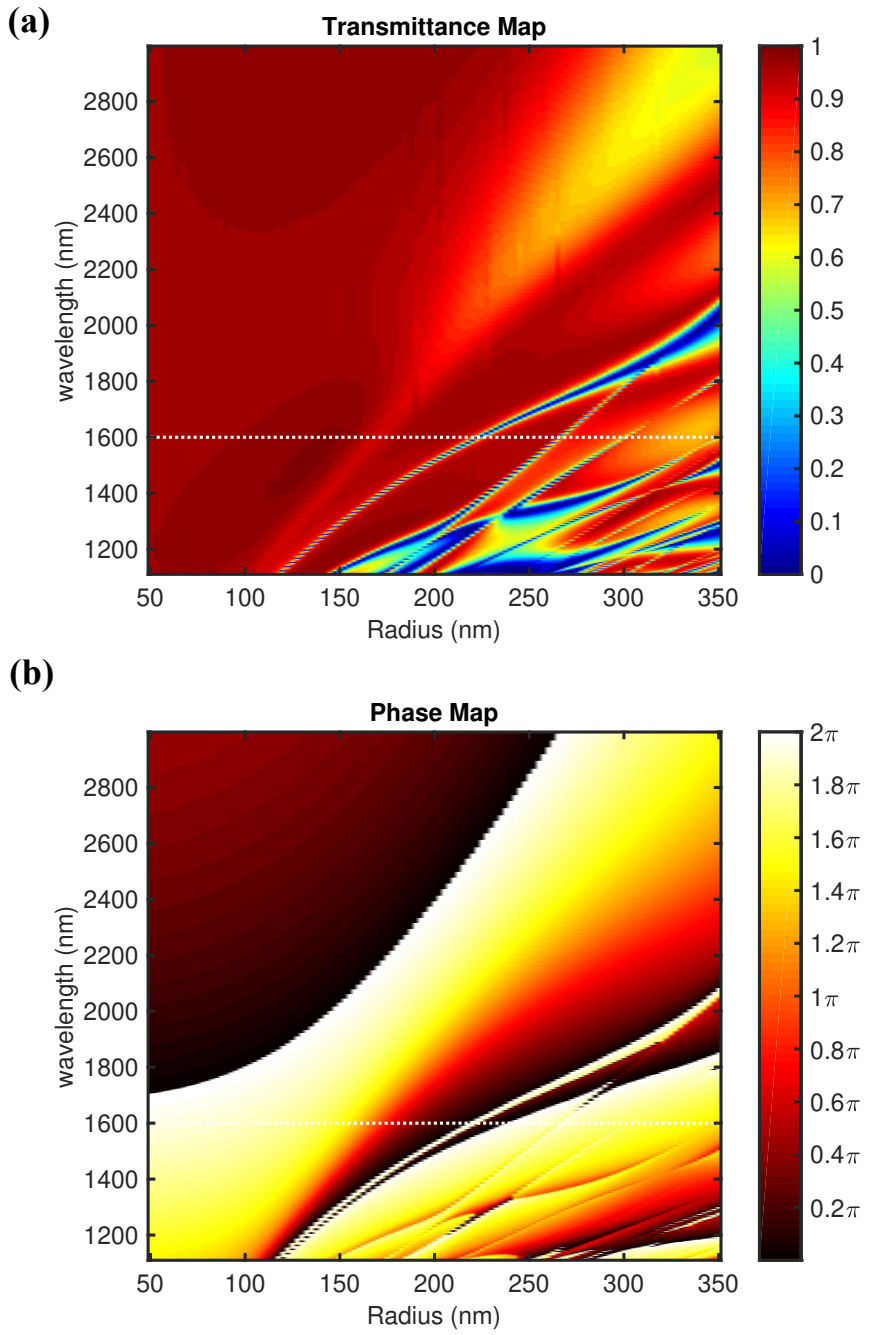

Figure 2.12: Numerical Calculations of broadband properties of the nanopillars array. (a) Transmission map vs Radius and wavelength. (b) Phase shift map (wrapped to 0-2π).

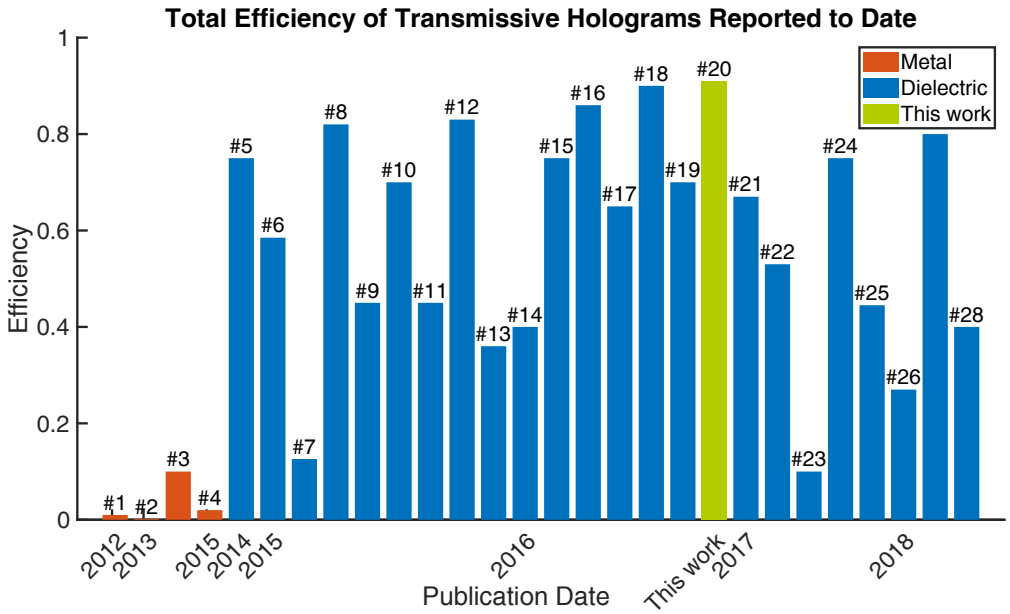

#1. F. Aieta & F. Capasso, Nano Lett., 2012; #2. F. Zhou & W. Cai, OPTICS EXPRESS, 2013; #3. X. Ni & V. Shalaev, Light: Science & Applications, 2013; #4. L. Huang & S. Zhang, Nature Comms, 2015; #5. D. Lin & M. Brongesma, Science, 2014; #6. T. Matsui & H. Iizuka, Opt Lett, 2015; #7. F. Aieta & F. Capasso, Science, 2015; #8. A. Arbabi & A. Faraon, Nat Comms, 2015; #9. Y. F. Yu & A. Kuznetsov, Laser Photonics Rev, 2015; #10. K. Chong & Yu. Kivshar, Nano Lett., 2015; #11. M. Shalaev & N. Litchinitser, Nano Lett., 2015; #12. A. Arbabi & A. Faraon, Nature Nanotech, 2015; #13. A. Zhan & A. Majumbar, ACS Photon, 2015; #14. K. Chong & Yu. Kivshar, ACS Photon, 2016; #15. M. Khorasaninejad & F. Capasso, Sci. Adv., 2016; #16. M. Khorasaninejad & F. Capasso, Science, 2016; #17. E. Arbabi & A. Faraon, Optica, 2016; #18. S. Kruk & Yu. Kivshar, APL Photonics, 2016; #19. A. Arbabi & A. Faraon, Nature Comms, 2016; #20. L. Wang & Yu. Kivshar, Optica, 2017; #21. Z. Zhou & T. Krauss, ACS Photon, 2017; #22. W. Chen & F. Capasso, Nano Lett., 2017; #23. R. Paniagua-Dominguez & A. Kuznetsov, ArXiV, 2017; #24. D. Sell & J. Fan, Nano Lett., 2017; #25. Q. Wang & W. Zhang, ACS Photonics, 2017; #26. Z. Li & C. Qiu, Light: Science & Applications, 2018; #27. K. Huang and H. Liu, ArXiV, 2018; #28. G. Lee and B. Lee, Nanoscale, 2018;

Figure 2.13: Chart for comparing the transmission efficiency of the holograms in chronological order. Our dielectric transparent hologram reaches the highest rank at 90% efficiency.

efit further development in applications like laser communication, Laser Radar (LADAR), fiber optic communications etc. This wavefront control method using dielectric metasurfaces can also easily adapt to other operating wavelengths by carefully choosing the material. For instance, titanium dioxide (TiO_2) can be used for visible ranges [11]. In this work we design the device to have the maximum performance and resonance overlap at optimized frequency. The broadband performance is measured in experiment and further analysis.

Nonlinear Nanostructures

3.1 Introduction

Nonlinear optical phenomena play an essential role in many areas of modern physics ranging from quantum optics to Electro-optics engineering. Research in the field of nonlinear optics led to a number of major technological breakthroughs. One particular important application is nonlinear frequency conversion, dealing with the generation of new optical frequencies in nonlinear processes. This nonlinear effect is the key element in modern laser physics where femtosecond lasers, whether optical parametric oscillator or optical parametric amplifier, are essentially made of optical resonators and nonlinear optical crystals. Another wide area is concerned with the effects of optical nonlinearities in various situations, from the propagation of intense ultrashort pulses in optical fibers, in supercontinuum generation, to optical signal processing.

Resonant photonic nanostructures can boost nonlinear optical effects with strong confinement of the local electromagnetic fields, which offers versatile opportunities for implementing nonlinear optics in a subwavelength fashion. Localized plasmonic resonances from metallic structures and Mie-type multipolar resonances and optically-induced magnetic response in all-dielectric nanostructures both exhibit potentials for boosting the nonlinear conversion efficiency as well as control the scattering behaviors for various applications. The study of nonlinear Nano-antennas becomes a developing field with many useful applications for a design of quantum light sources, nanolasers, sensors, and ultrafast compact metadevices. To achieve the desired functionalities, it is essential to gain flexible control over the near- and far-field

properties of the nanostructures. Thus, both modal and multipolar analyses are widely exploited for engineering nonlinear scattering from resonant nanoscale elements, in particular for enhancing the near-field interaction or tailoring the far-field multipolar interference for optimization of the radiation directionality.

In Chapter 2 the wavefront control of metasurfaces for the linear optics is studied both theoretically and experimentally. So it is natural to extend such functionalities to nonlinear optics. Therefore the nonlinear nano-optics of various kinds of nano-antennas are studied in this chapter in order to assist design of phase elements for nonlinear holograms discussed in Chapter 4.

Section 3.2 briefly reviews the general idea of nonlinear optic response and the multipole decomposition methods for theoretical analysis [31]. Then the experimental methods for measuring the nonlinear radiation pattern is explained in Section 3.2.3. Two particular cases, the multipolar THG in metal-insulator-metal structure (see Section 3.3) and in all-dielectric nano-structures (see Section 3.4) are studied both theoretically and experimentally as discussed in the following sections. I lead these two projects by both theory and experiment, the results are published in [33, 71]. The nonlinear optics setup (see Section 3.2.3) that I developed is also used for researches of second harmonic generation (SHG) from nanostructures made from III-V material, as discussed in Section 3.5 and published as [72, 73].

3.2 Theory and Methods

3.2.1 Nonlinear Harmonic Generation

Within the macroscopic description utilizing macroscopic Maxwell's equations Eq. (2.1), nonlinear optics employs the nonlinear constitutive relations. For example, in the electric dipole approximation of light-matter interaction, the material response in a non-magnetic medium can be specified by the nonlinear relationship between the applied electric field **E** and induced polarization **P**

as

$$\mathbf{P} = \epsilon_0 \left[\overleftrightarrow{\chi}^{(1)} \cdot \mathbf{E} + \overleftrightarrow{\chi}^{(2)} : \mathbf{EE} + \overleftrightarrow{\chi}^{(3)} : \mathbf{EEE} + \dots \right] , \tag{3.1}$$

written in the form of an asymptotic expansion in a Taylor series. Here, the first term corresponds to the linear regime at weak excitation fields, and $\overleftrightarrow{\chi}^{(N)}$ are the N-th order susceptibility tensors of rank $N+1$, which capture both the polarization dependent nature of the parametric interaction as well as the symmetries of the concrete material. Since the optical nonlinearities of natural materials are rather weak, the nonlinear scattering manifests at sufficiently strong applied electromagnetic fields, achievable with powerful coherent light sources, lasers. Given the fact that considerable amounts of electromagnetic energy can be confined to tiny volumes in nanoparticles or even smaller hot spots, they enable the down-scaling of the required optical powers, because the power of SHG/THG has quadratic/cubic dependency on the pump power.

Symmetry considerations appear of particular importance in nonlinear optics. For instance, the second-order nonlinear effects are inhibited in the bulk of such uniform centrosymmetric media, such as plasmonic metals and group IV semiconductors, within the electric dipole approximation of the light-matter interaction because of the symmetry constraints, while no such restriction exists for third-order processes [74].

However, the inversion symmetry is broken at interfaces, thus enabling the second-order nonlinear processes from surfaces of isotropic crystals due to the electric-dipole surface contribution to the nonlinear polarization. Its sensitivity to surface properties is used in probing techniques. The bulk nonlinear polarization arises from higher-order nonlocal magnetic-dipole and electric-quadrupole interactions with light at the microscopic level. To account for the multipolar orders, the effective light-matter interaction Hamiltonian [75,76] is expanded as such

$$H_{\text{int}} = -\mathbf{p} \cdot \mathbf{E} - \mathbf{m} \cdot \mathbf{B} - \mathbf{Q} : \nabla \mathbf{E} + \dots , \tag{3.2}$$

where the electric dipole $\mathbf{p}$, magnetic dipole $\mathbf{m}$ and electric quadrupole

moments **Q** are here interpreted as operators. For instance the SHG is commonly supported by the III-V material such as GaAs and AlGaAs and THG is supported by Silicon due to their particular symmetries of the crystal structures.

3.2.2 Multipole decomposition

Generally, in the problems of both linear and nonlinear scattering at arbitrary nanoscale objects, multipole decomposition of the scattered electromagnetic fields provides a transparent interpretation for the measurable far-field characteristics, such as radiation efficiency and radiation patterns, since they are essentially determined by the interference of dominating excited multipole modes [77–83].

In terms of the electric a_E and magnetic a_M scattering coefficients, the total time-averaged scattered power (energy flow) is given by

$$W_s = \frac{\pi |E_0|^2}{2\eta k^2} \sum_{l=1}^{\infty} \sum_{m=-l}^{l} (2l+1) \left(|a_E(l,m)|^2 + |a_M(l,m)|^2 \right), \quad (3.3)$$

revealing the input of each multipolar excitation (namely, dipole at $l = 1$, quadrupole at $l = 2$, octupole at $l = 3$, etc). Here, $k = \omega\sqrt{\epsilon\mu}$ is the wavenumber in the medium, $\eta = \sqrt{\mu/\epsilon}$ is the impedance, E_0 is an electric field amplitude factor, l and m are angular momentum (orbital) and magnetic quantum numbers, respectively. Equation (3.3) is written in SI units under normalization accepted in Ref. [83]. To describe the radiation from arbitrary localized sources, the multipole coefficients $a_{E,M}$ can be retrieved either through the volume integration of the source current density distribution, or by taking angular integrals of radial (or angular) components of the numerically pre-calculated electromagnetic field with spherical harmonics over a spherical surface enclosing a scatterer. If no analytical solution can be obtained, the field at the surface of such a sphere can be found with the use of numerical codes or modern commercial full-wave solvers.

Assuming the far-field asymptotic of the outgoing spherical

wave, the field expansion into the vector spherical harmonics $\mathbf{X}_{l,m}(\theta,\phi)$ recovers the directional dependence of the radiation as follows

$$\frac{dP(\theta,\varphi)}{d\Omega} = \frac{\pi|E_0|^2}{2\eta k^2}\left|\sum_{l=1}^{\infty}\sum_{m=-l}^{l}(-i)^{l+1}(2l+1)\right.$$
$$\left.\cdot\left(i^l a_M(l,m)\mathbf{X}_{l,m} + i^{l+1}a_E(l,m)\hat{\mathbf{r}}\times\mathbf{X}_{l,m}\right)\right|^2, \quad (3.4)$$

defined as a power per unit solid angle Ω in spherical coordinates $\{\theta,\varphi\}$, $\hat{\mathbf{r}}$ denotes the unit radius vector. The scattered electric far-field can be also conveniently expressed through the decomposition in Cartesian multipolar terms [77] as a sum

$$\mathbf{E}_{\text{sca}} = \mathbf{E}_{\text{ED}} + \mathbf{E}_{\text{MD}} + \mathbf{E}_{\text{EQ}} + \ldots = \frac{k^2}{4\pi\varepsilon_0}\frac{e^{ikr}}{r}\left\{[[\hat{\mathbf{r}}\times\mathbf{p}]\times\hat{\mathbf{r}}]\right.$$
$$\left. - \frac{1}{c}[\hat{\mathbf{r}}\times\mathbf{m}] - \frac{ik}{6}[[\hat{\mathbf{r}}\times\mathbf{Q}(\hat{\mathbf{r}})]\times\hat{\mathbf{r}}] + \ldots\right\}, \quad (3.5)$$

where $\mathbf{p}$, $\mathbf{m}$ and $\mathbf{Q}$ are the electric dipole (ED), magnetic dipole (MD) and electric quadrupole (EQ) leading moments, respectively, and ϵ_0 is the vacuum permittivity. Tuning the contributions of different-order multipole moments is used to engineer the scattering and tailor the emission directionality of optical nanoantennas [84–93]. In particular, the first Kerker condition for overlapped and balanced orthogonal electric and magnetic dipoles represents an example of *unidirectional scattering* [94] from a single-element antenna. The scattering is interferencially suppressed in either backward or forward direction, if the relation $1/\epsilon_0 p_x = \pm\eta m_y$ holds for the only non-negligible Cartesian electric p_x and magnetic m_y dipolar moments induced in a particle along the x and y axes, respectively. Developing this concept, the directionality of the scattering can be improved through the interference of properly excited higher-order electric and magnetic modes [95–99].

However, as discussed e.g. in Refs. [100, 101], the local-field

features and far-field properties are intimately linked in the nonlinear response of nanostructures. A formal way to quantify this effect is based on the Lorentz reciprocity theorem. Particularly, this method allows one to predict the metamaterial nonlinearity by using linear calculations [101], and to express the excitation coefficients of spherical multipoles, the radiated field is decomposed into, through the overlap integrals of the nonlinear source and the respective spherical modes [102]. In this regard, two key ingredients to realize strong nonlinear response from nanostructures are usually emphasized: the local field enhancement and modal overlaps. For instance, the efficiency of harmonic generation can be strongly enhanced in nanostructures, provided the pump or generated frequency matches the supported resonance [103], especially, if the geometry is doubly resonant [24,104–107], i.e. sustains resonances at both the fundamental and harmonic frequencies, and spatial distribution of the nonlinear source is such that it strongly couples the corresponding modes.

For metamaterials, the applicability of simple estimates based on the nonlinear oscillator model [108,109] and Miller's law [110, 111] is limited to the specific cases only [101, 112], e.g. odd in frequency third-harmonic generation [113–115]. In fact, the character and efficiency of the nonlinear response in nanostructures is highly affected by many factors [116], including variations in their size, shape, material filling fractions, quality of samples, interparticle interactions, spatial symmetries of both geometry and excitation beams, linear scattering properties. Nonetheless, to a large extent, the key governing features may be approached with the analysis of the unique resonant behaviour of these artificial materials [117], as well as strengths and mutual interference of the leading excited or generated field multipoles [118].

3.2.3 Nonlinear Setup

To experimentally study the radiation pattern of the nonlinear generation, the switchable back-focal plane (BFP) imaging technique is used. First the real space image of the sample surface is turned into focus with the real space imaging mode. Then we in-

sert the BFP lens so that the Fourier space image of the radiation can be captured. The location of the BFP lens is pre-calibrated with a green laser and grating sample, so that the BFP lens is at focal length away from the back focal plane of the collecting objective. Therefore all the THG light emitted from the sample at the same angle will reach the same spot at the camera CCD. The capture Fourier plane image is corresponding to the angular distribution of the radiation pattern. See Figure 3.1.

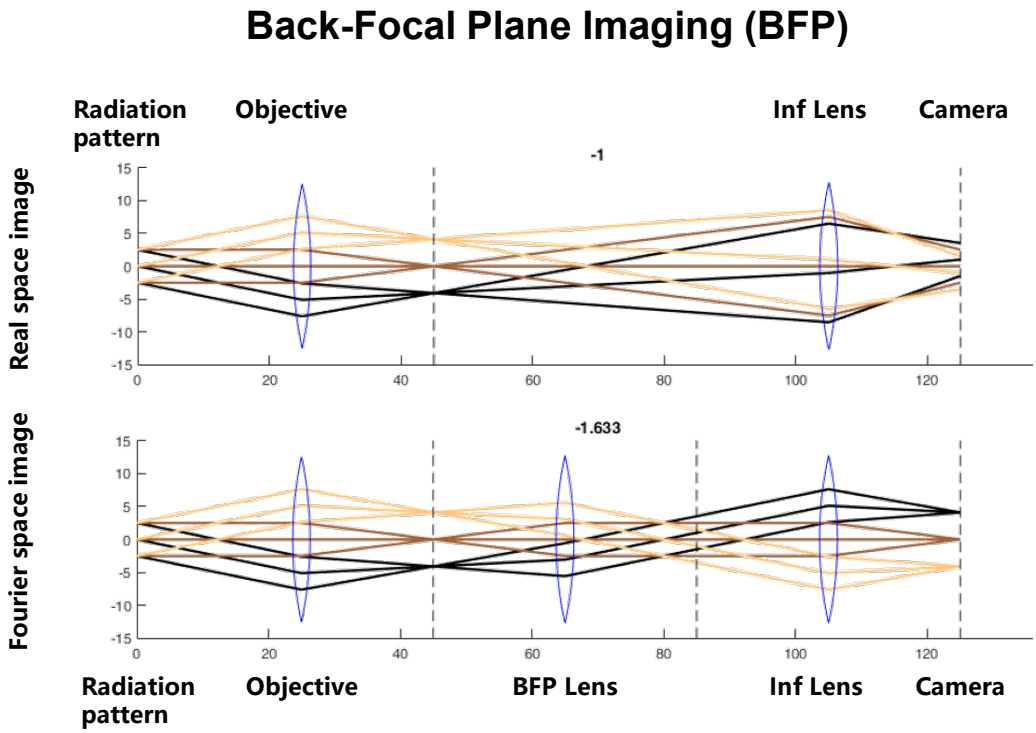

Figure 3.1: Light path (not to scale) of the infinite corrected microscopic imaging and back focal plane imaging.

The nonlinear optics setup is built with the BFP imaging principle. As shown in Figure 3.2, we utilize two BFP arms, one on each side of the sample. The infrared femto-second laser is introduced into the optical axis using a dichroic mirror that is almost 100% reflective to the IR wavelength and transparent to TH wavelength. The IR objective in the backward arm also serves for focusing the pump on the sample, exciting the nonlinear harmonic generation. The generated nonlinear signal is collected by the objectives on each side and filtered by the selected filters, so that only the signal of interest can pass through and the reflected or transmitted pump laser is blocked. The filters can be bandpass

filters for TH or SH signals for fixed wavelength experiments or dedicated short pass filters for TH or SH in spectroscopy measurements. Since the light is infinite corrected, waveplates and analyzers can be added to study the polarization of the signal.

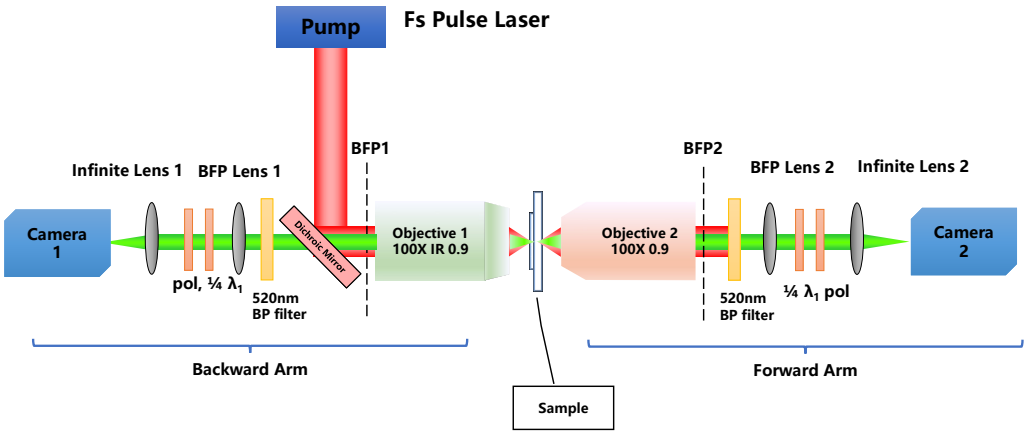

Figure 3.2: A general illustration of the nonlinear optic setup. Details can vary depending on the specific needs of the experiments

3.3 Multipolar THG from MIM Nanostructrues

While more accurate models taking into account the multipolar contribution of the nonlinear response have been theoretically developed [119, 120], the experimental techniques for such nonlinear multipolar analyses remain under developed. This is an enduring problem and a number of indirect techniques have been tested. The multipolar contribution of the SHG process in plasmonic metasurfaces was possible to derive through the analysis of the nonlinear interference in forward/backward directions and for different incident polarizations [121–124]. Other indirect techniques also include non-collinear SHG [125] and multipolar decomposition through the analyses of the broad spectrum nonlinear response of magnetic plasmonic metasurfaces [26]. However, the direct measurement of the different multipolar contributions from metamaterials with defined magnetic response has not been demonstrated to date.

Here, we demonstrate such direct measurement by analyzing the radiation pattern of THG from an optical metasurface of metal-dielectric-metal fishnet metamaterials in the vicinity of

their optically-induced magnetic resonances. The multipolar radiation pattern of the THG signal is measured by a Fourier imaging technique. Fitting the measured radiation pattern to the radiation patterns of different multipolar contributions from the constituents of the metasurface shows that the observed third harmonic radiation of the fishnet sample is a result of an interference between the magnetic and electric multipolar contributions of the nonlinear material polarization. The concept of this process is shown in Figure 3.3. Our results give a direct evidence of the higher order multipolar contribution to the harmonic generation from magnetic metamaterials.

3.3.1 Experimental arrangements

The analysis of the radiation pattern of emission from optical nanoantennas has been recently used as an experimental tool to identify the superposition of the involved electric and magnetic multipolar contributions [99, 126–129]. Such analysis should also be applicable for the case of the nonlinear (second and third harmonic) emission [130–134], however the experimental multipolar characterisation of the harmonic radiation from nonlinear nanoantennas is still lacking. A Fourier analysis of the second harmonic radiation from multipolar nanoantennas was recently performed in Refs. [135, 136], however the multipolar contributions of this emission was not established. Here we perform such analysis, for the first time, to identify the multipolar origin of the harmonic generation process in metamaterials with magnetic response.

In our studies we use metal-dielectric-metal fishnet structure in the vicinity of optically-induced magnetic resonances (Figure 3.3). The fishnet metamaterials are exemplary structures with a well studied linear magnetic response [137,138] due to the excitation of anti-parallel currents in the top and bottom metal layers. The nonlinear response of fishnets has also been experimentally studied for optical switching with fast [139] or slow nonlinearity [140], as well as for harmonic generation [141, 142]. Ref. [142] has been specifically focused on the exploration of harmonic contributions different from the electric dipolar response

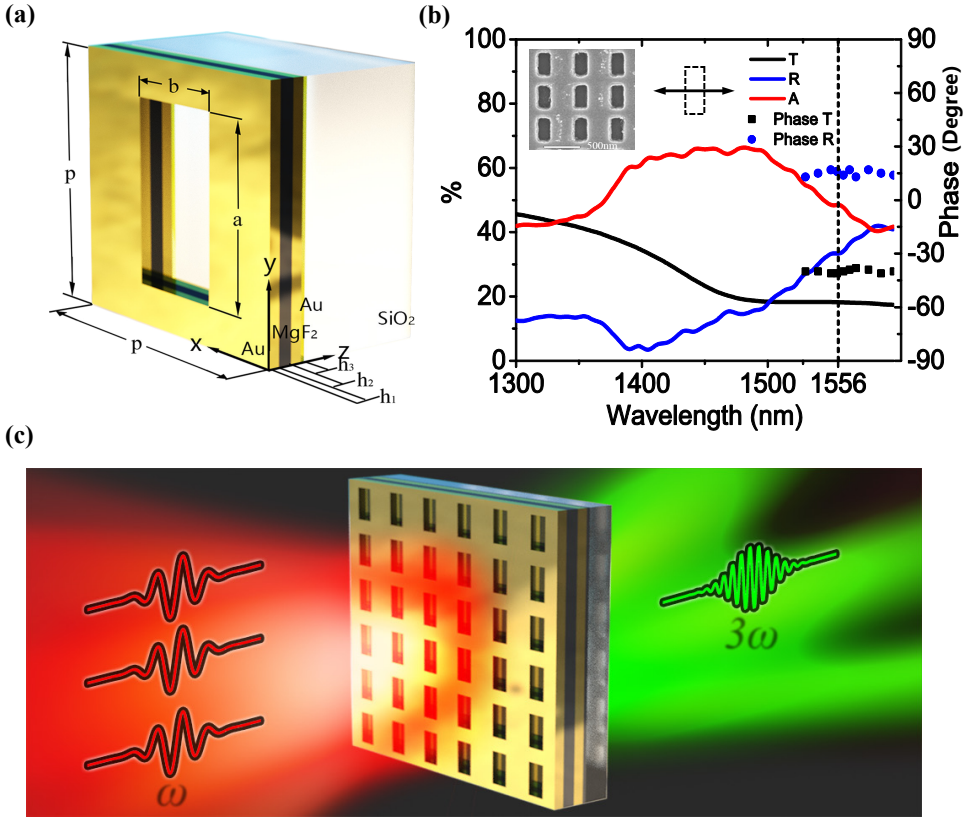

Figure 3.3: (a) Geometry of our fishnet metamaterial. The sizes are: $p = 500\,\text{nm}$; $a = 350\,\text{nm}$; $b = 190\,\text{nm}$; $h_1 = h_3 = 20\,\text{nm}$; and $h_2 = 25\,\text{nm}$. (b) Measured transmission (black curve), reflection (blue curve) and absorption (red curve) spectra of the fishnet for horizontal polarization of the incident light (i.e. electric field is parallel to the short side of the rectangular holes). Experimentally measured phase (dots) spectra of the fishnet metamaterial. The inset shows a scanning electron micrograph image of the fabricated sample. The vertical dashed line indicates the spectral position of the fundamental wavelength.(c) Concept of the multipolar THG from fishnet

through angular dependent THG measurements. However, only indirect evidence of non-dipolar nonlinear terms was provided. A direct quantification of the higher order multipolar terms in the THG process is still missing.

To provide a quantitative experimental analysis of the harmonic generation process in magnetic metamaterials, we fabricated a sample of a fishnet metamaterial using electron beam lithography. The metamaterial consists of a tri-layer $Au/MgF_2/Au$ structure perforated with holes periodically. Figure 3.3(a) shows the dimensions of the structure, and the inset in Figure 3.3(b) shows a scanning electron micrograph. We measure the transmission and reflection spectra of the fishnet in order to determine the resonant absorption in the structure and to identify the position of the magnetic resonance [see Figure 3.3(b)]. We note that the magnetic properties of the fishnet metamaterials are present only for horizontal polarization [143] [as marked in Figure 3.3(b)], while for vertical polarization the structure is not transmissive. The resonance in the absorption spectrum was found to be around 1450 nm and is associated with magnetic resonance in the structure. In our experiments we optically pump the fishnet metamaterial at fundamental wavelength of 1556 nm, which is on the long-wavelength side of the maximal absorption wavelength, however within the resonance width.

We next numerically calculate the linear response of the fishnet structure at 1556 nm wavelength using Lumerical FDTD solutions shown in Figure 3.4(b). Figure 3.4 (a)(c) depicts the calculated electric field magnitude inside the fishnet metamaterial at the fundamental wavelength, showing 23-fold enhancement of the local field (in comparison to the incident field) inside the middle dielectric layer. Figure 3.4(a) illustrates the electric field magnitude in the xy cross section placed in the middle of the MgF_2 layer. The dashed white line shows the location of the rectangular hole. The xz cross section of the electric field magnitude is shown in Figure 3.4(c). The cross section is taken through the center of the hole. The field distribution indicates that a standing wave is formed in the center of the dielectric layer by two plasmon currents, propagating in opposite directions at the inter-

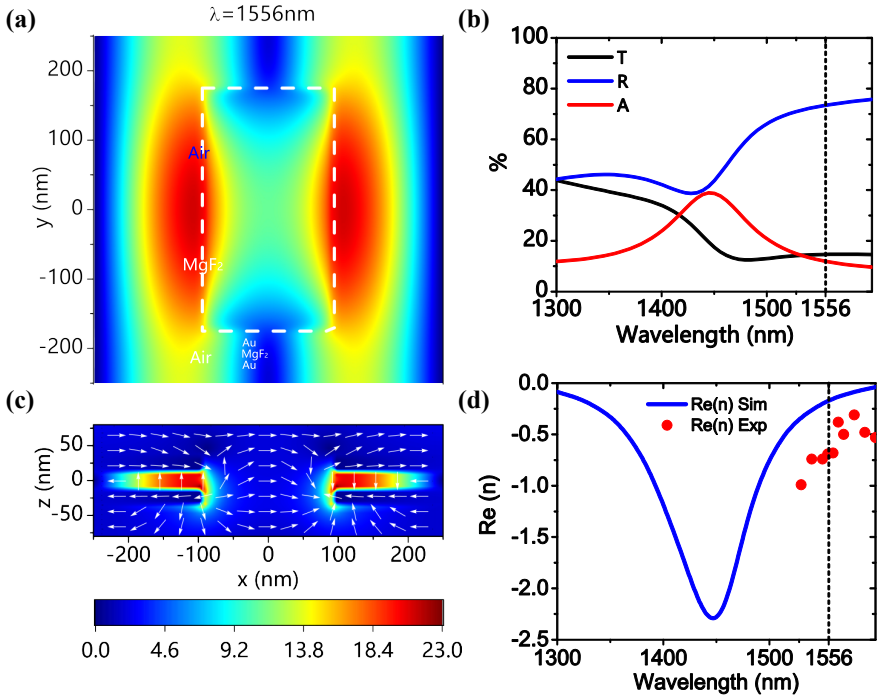

Figure 3.4: Calculated electric field magnitude normalized to the incident field amplitude inside the fishnet sample at the pump wavelength. (a) *xy* cross section of the field taken through the center of the MgF_2 layer. Dashed line shows the location of the rectangular hole. (b) Simulated linear spectrum of Fishnet. (c) *xz* cross section of taken through the center of the hole. (d) Comparison of effective refractive index, real part.

faces between top and bottom gold layers and the dielectric slab [visualized by the vectorial *E*-field distribution in Figure 3.4(c)]. These plasmon currents in Au layers together with the displacement currents running through the MgF_2 spacer form effective optical magnetic response under the incident pump excitation. This is confirmed by the extraction of the effective index of the fishnet structure [144], which becomes negative at the position of the absorption resonance, including the position of the fundamental wave Figure 3.4(d).

We also experimentally determine the effective refractive index as well as the electric and magnetic surface polarizabilities of the metamaterial for linear horizontal polarization. For this purpose we measure the amplitude and phase of both transmission and reflection using interferometry methods similar to Ref. [145], see Figure 3.3(b). The phase measurements are performed in the spectral range $1530 - 1605\,\text{nm}$, which is defined by the spectral range of our laser light source used for the interferometry. We

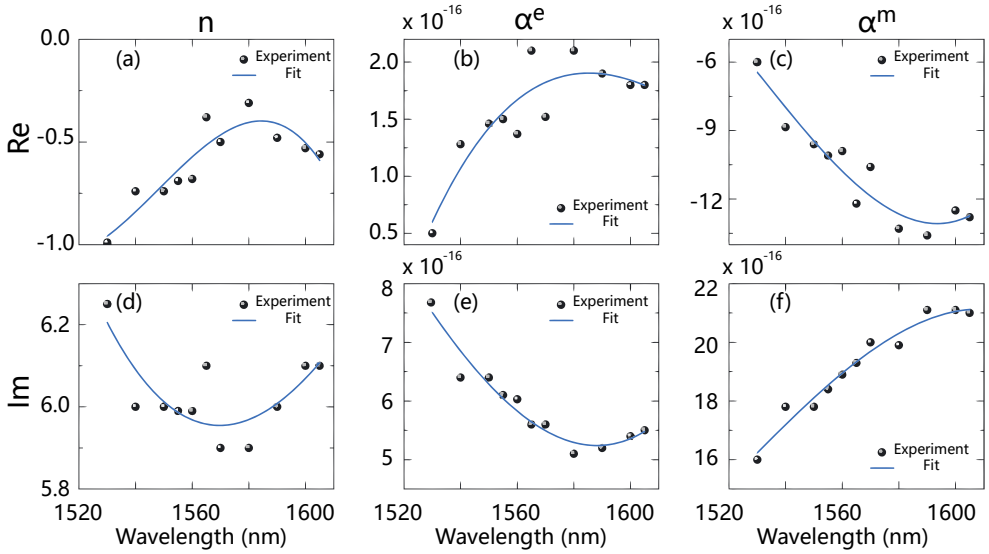

Figure 3.5: Experimentally extracted effective parameters of the fishnet metamaterial: real parts (a-c) and imaginary parts (d-f) of effective refractive index (a,d), surface electric polarizability (b,e) and surface magnetic polarizability (c,f).

then use inverted Fresnel equations to extract the effective refractive index [144] and surface polarizabilities [146] of the structure, see Figure 3.5. In particular, we find that at the pump wavelength of 1556 nm the structure exhibits negative magnetic polarizability and negative refractive index of $n = -0.62$, which matches the calculated values as seen in Figure 3.4(d).

Next we investigate the THG in our fishnet metamaterial. Since the THG process is extremely sensitive to the nanostructure resonances, which enhance the local electric field [17, 27, 147–149], we expect enhanced nonlinear response from our fishnet metamaterials in the vicinity of its resonances. Also, as mentioned above, the fishnet has magnetic resonance, verified by numerical calculations of linear field distribution and experimental measurements of its negative refractive index, we are interested to find directly the link between its magnetic resonance of linear response to the multipolar properties of the THG in the nonlinear process. The third harmonic generation (THG) is a nonlinear process that is independent on the symmetry (centro-symmetric or anisotropic) of the constituent elements of the structure, making it attractive for the investigation on nonlinear optical phenomena in nanophotonics.

In our experimental study we use the experimental setup de-

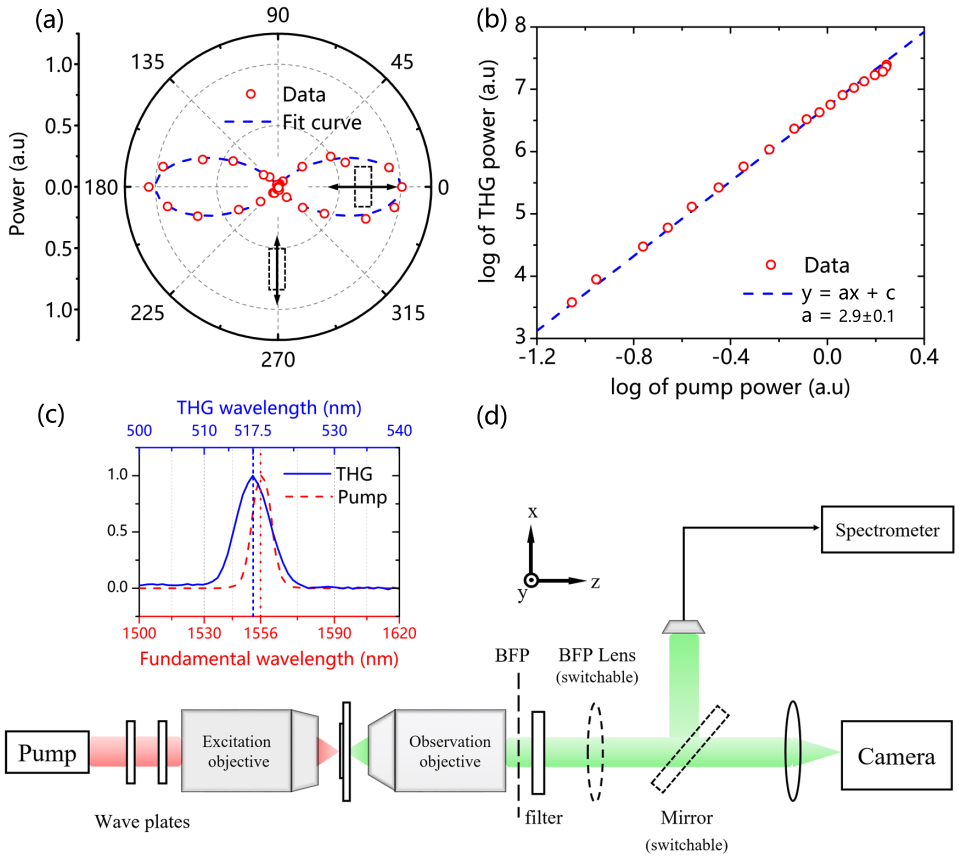

Figure 3.6: (a) The pump polarization dependency of the THG signal in polar coordinate. Zero angle corresponds to the case when the pump polarization is in the x direction. (b) The pump power dependency of the THG signal. The THG signal power as a function of the pump power, shown in a log scale, reveals a linear relation of $y = a * x + c$, where $a = 2.9 \pm 0.1$, which matches the expected cubic relation between the pump and the THG signal power. (c) Measured THG and pump spectra (normalized to max value). The red curve represents the pump spectrum, the red x axes is centered at the pump wavelength (1556 nm). The blue curve depicts the spectrum on the observed third harmonic on a axes corresponding to one third of the fundamental wavelength. (d) Scheme of the experimental setup. The polarization of the pump beam is manipulated by a half-waveplate. The THG is generated and observed by a confocal microscopic setup. Bandpass filter at the THG wavelength is used for the radiation pattern imaging.

picted in Figure 3.6. A femtosecond Er^{3+}-doped fiber laser ($\sim$ 500 fs, repetition rate of 5 MHz) with the central wavelength of 1556 nm is used as a pump. The short femtosecond pulses allow to achieve strong peak intensity and low average power at the same time, which prevents thermal damage of the sample. The pump laser beam passes through a quarter and half waveplates, which provides linear output polarization with controllable orientation.

An infrared objective lens (Olympus LCPlanN $100\times, NA = 0.85$) is used to focus the pump laser beam onto the sample top gold surface to a diameter of $\sim 2\,\mu$m), exciting approximately twelve unit-cells of the structure, see Figure 3.7. The output emission pattern is then represented a superposition of the radiation patterns from several localized third harmonic emitters, positioned in a periodic array. The THG signal is collected by a confocal visible objective (Olympus MPlanFL $50\times, NA = 0.8$). The metal surface of the sample is facing the pump laser. Then the third harmonic radiation is either launched into a spectrometer (Ocean Optics 6500), or sent to a Peltier-cooled camera with an infinity-corrected objective to build a real-space image. For the imaging purposes, a 520 nm ($\pm$10 nm) bandpass filter is used to transmit the third harmonic radiation only, thus preventing unwanted transmission at fundamental wavelength to be captured by the camera. A switchable mirror is used to change the beam path between the spectrometer and the camera. A switchable back focal plane lens is also placed in the back focal plane (BFP) of the observation objective in order to capture the Fourier space image of the third harmonic radiation (i.e. the angular distribution of the radiation pattern).

Figure 3.6(a) shows the dependency of the third harmonic intensity versus the direction of polarization of the pump. In the polar coordinate system the zero angle corresponds to the horizontally-polarized pump, as indicated in the figure. The radial coordinate represents the THG signal power, measured by the spectrometer. Figure 3.6(b) shows the power dependency of the THG. The pump power is adjusted with a continuously variable neutral density filters and is monitored by a power me-

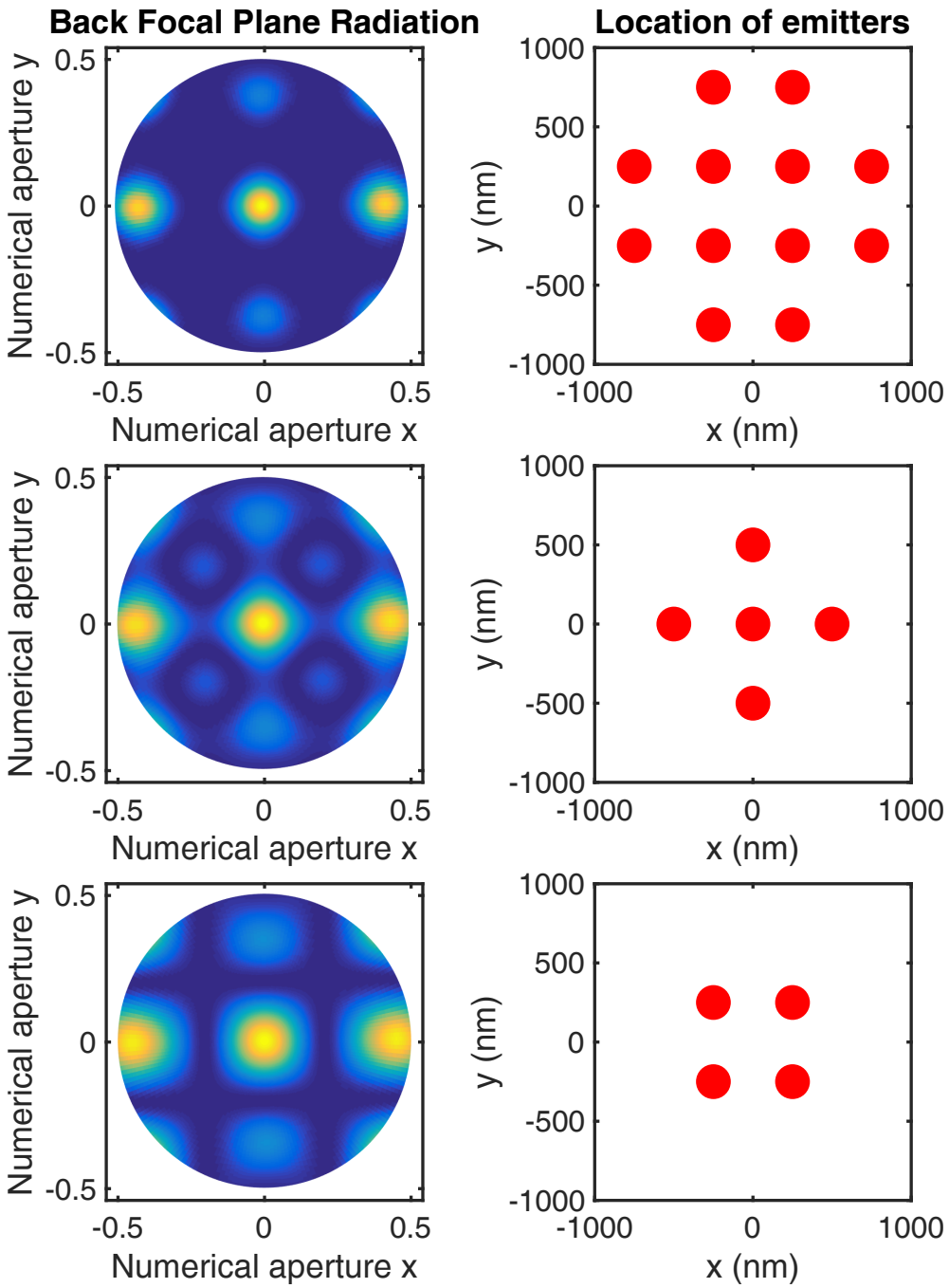

Figure 3.7: Comparison of multipole emitter array types. (a) Red dots on the right picture represent the array locations of the multipole emitters. It consider only the 12 fishnet unit cells within the Gaussian beam waist of the pumps focal spot. The calculated back focal plane image is derived from the superposition of these multipole emitters in this array. (b) The calculated back focal plane image of multipole model. The same complex amplitudes of ED, MD and EQ is used but only 5 emitters are included in the array. The general radiation features are the same as that in (a). (c) The case with 4 emitters. It can be seen the BFP radiation of 12 multipole emitters, in (a), has the best match with the experimental result in Figure 3.7 (a).

ter. The logarithm of THG power, y, has an approximately linear relation of $y = a * x + c$, where $a = 2.9 \pm 0.1$ and x is the pump power, that gives us $P_{THG} = C * P_{pump}^{2.9\pm0.1}$, which matches well the expected cubic relation between the pump and the THG power. Figure 3.6(c) shows the spectra of the pump (red dashed curve, bottom axis) and THG (blue curve, top axis). The overlap between the THG and the pump spectra confirms that measured signal is indeed a third harmonic and not photoluminescence from the sample. Note that the presence of the plasmonic resonances at the fundamental frequency can substantially change spectrum of the THG emission [150]. The measured blue spectral shift of THG emission ($\sim 1.2\,\text{nm}$) is a consequence of magnetic resonance of the fishnet being blue-shifted in comparison to the fundamental wavelength.

3.3.2 THG radiation pattern and multipole analysis

To analyze the nonlinear properties of the fishnet sample we measure the directionality of the third harmonic radiation. For this we build a back-focal plane image of the THG on the camera. We observe three distinct maxima located along the x-direction as seen in Figure 3.8(a). The circular boundary around the figure represents the numerical aperture of our system, which is limited by the total internal reflection in the substrate and equals 0.54. We then numerically calculate the THG far-field radiation pattern of the fishnet sample for the resonant excitation using Lumerical software [see Figure 3.8(b)]. The calculations show a good qualitative match with our experiments.

In order to gain a deeper insight to the origin of the THG radiation pattern we use the multipole model to analyze its spatial structure. For this we start with expansion of the vector potential in the far zone ($kr \gg 1$) in powers of k considering the dimension of the source to be small compared to wavelength ($kd \ll 1$):

$$\lim_{kr\to\infty} \mathbf{A}(\mathbf{x}) = \frac{\mu_0}{4\pi}\frac{e^{ikr}}{r}\sum_n \frac{(-ik)^n}{n!}\int \mathbf{J}(\mathbf{x}')(\mathbf{n}\cdot\mathbf{x}')^n d^3x', \tag{3.6}$$

where $\mathbf{x}$ is the vector from origin $(0,0,0)$ to a certain point (x_1, x_2, x_3)

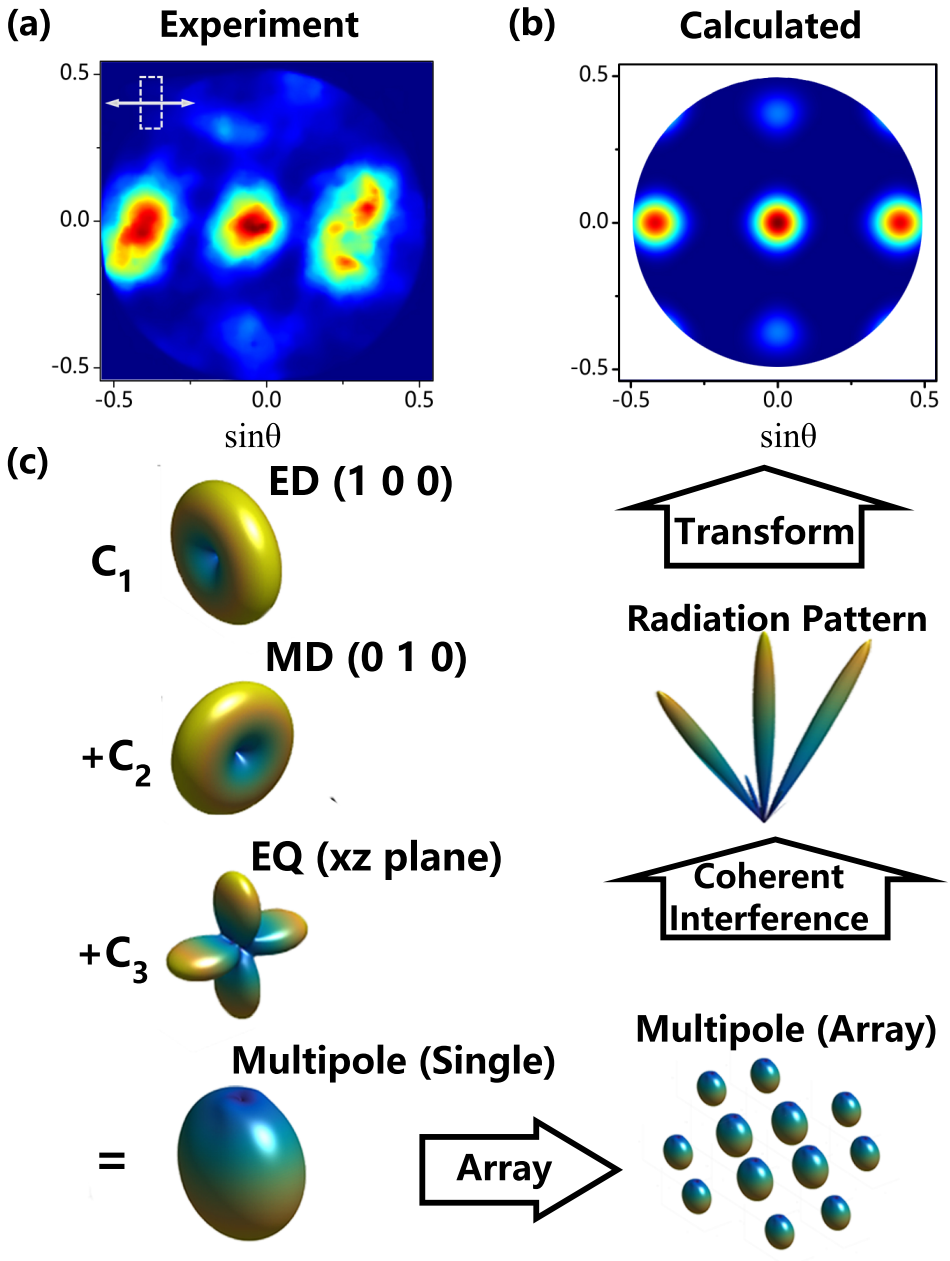

Figure 3.8: (a) Measured directionality of the THG radiation. The numerical aperture of the captured THG signal is 0.54 limited by the total internal reflection in substrate. (b) THG far-field radiation pattern of the fishnet sample for the resonant excitation case. (c) Calculated Fourier space image of the radiation from the array of multipoles under the Gaussian excitation. (d) Radiation pattern of different multipoles.

in the far zone, $\mathbf{n}$ is the unity vector in direction of $\mathbf{x}$, r is the length of $\mathbf{x}$, $\mathbf{x}'$ is the vector from origin to a certain source point, $\mathbf{J(x)}'$ is the current density [151].

The first term gives the electric dipole (ED) radiation:

$$\mathbf{H}_{ED} = \frac{ck^2}{4\pi}(\mathbf{n} \times \mathbf{p})\frac{e^{ikr}}{r}, \tag{3.7}$$

where the ED moment $\mathbf{p} = \int \mathbf{x}'\rho(\mathbf{x}')d^3x'$, $\rho(\mathbf{x}')$ is the charge density distribution, and $Z_0 = \sqrt{\mu_0/\epsilon_0}$ is the free space impedance.

The next terms of the expansion give a magnetic dipole (MD) and an electric quadrupole (EQ) response. The MD term can be written as:

$$\mathbf{H}_{MD} = \frac{k^2}{4\pi}(\mathbf{n} \times \mathbf{m}) \times \mathbf{n}\frac{e^{ikr}}{r}, \tag{3.8}$$

where $\mathbf{m} = \frac{1}{2}\int(\mathbf{x}' \times \mathbf{J}(\mathbf{x}'))d^3x'$ is the MD moment.

The EQ radiation is represented as:

$$\mathbf{H}_{EQ} = -\frac{ick^3}{24\pi}\Big(\mathbf{n} \times \mathbf{Q}(\mathbf{n})\Big)\frac{e^{ikr}}{r}. \tag{3.9}$$

Vector Q(n) = (Q_1 Q_2 Q_3) is defined as $Q_\alpha = \sum_\beta Q_{\alpha\beta}n_\beta$, where $\alpha, \beta = 1, 2, 3$. $Q_{\alpha\beta} = \int(3x'_\alpha x'_\beta - r'^2\delta_{\alpha\beta})\rho(\mathbf{x}')d^3x'$ is the quadrupole moment tensor.

The spatial orientations of the multipoles can be predefined by the simulated field results in Figure 3.4. The collective charge motion in the metal is considered as oscillator along the xz plane. Therefore the symmetric resonance will create parallel currents with ED radiation while the antisymmetric resonance leads to anti-parallel currents with MD radiation. The antisymmetric charge distribution along the xz plane gives rise to the EQ with only $Q_{xz} = Q_{xz} \neq 0$. The corresponding radiation patterns of the considered multiple terms are shown in Figure 3.8(d).

The electromagnetic field of the THG could be considered as the coherent superposition of the fields emitted by various multipoles. Considering only the first three terms, the total field can be written as: $\mathbf{H}_{multi} = C_1\mathbf{H}_{ED} + C_2\mathbf{H}_{MD} + C_3\mathbf{H}_{EQ}$, where C_α are complex coefficients. The electric field is $\mathbf{E}_{multi} = Z_0\mathbf{H}_{multi} \times \mathbf{n}$. In these equations the relative amplitudes and phase of the multi-

poles are fitting parameters. Then the radiation pattern could be calculated via the time-averaged Poynting vector given by $\langle \mathbf{S} \rangle = \frac{1}{2} Re(\mathbf{E}_{multi} \times \mathbf{H}^*_{multi})$. The radiation power distribution can be written as the power radiated per unit angle: $\frac{dP}{d\Omega} = \mathbf{n} \cdot \langle \mathbf{S} \rangle r^2$.

Due to the larger size of the focal spot of the pump laser (diameter of around 2 μm) in comparison to the period of the fishnet (0.5 μm) in our analysis we also consider the nonlinear emission from an array of third harmonic emitters: the central unit cell and the second nearest neighbors. The multipole model also takes this array effect into account by considering each unit cell as an individual multipolar emitter. Their phases and amplitudes are defined by the Gaussian beam profile of pump with a corresponding waist size. We also take into account the effect of the substrate on the effective period of the emitter array. Then the resulting field takes the form:

$$\mathbf{H}_{array}(\mathbf{x}) = e^{\frac{-s_n^2}{w^2}} \sum_{\mathbf{s}_n} \mathbf{H}_{multi}(\mathbf{x} - \mathbf{s}_n), \tag{3.10}$$

where s_n is the vector from origin to the location of the n-th element of the array, w is the beam waist size.

From our analysis we obtain that the THG emission is a coherent superposition of an electric dipole, a magnetic dipole and an electric quadrupole mode. The amplitude ratios of the multipolar modes are $A_{ED}/A_{EQ} = 1.58$ and $A_{MD}/A_{EQ} = 1.33$. Since our experimental measurements provide us only with the intensities of THG, we could not uniquely identify the set of relative phases. Therefore, our multipolar analysis results in two sets of phase differences that give identical results (for the same amplitude ratios). One set is $\varphi_{ED} - \varphi_{EQ} = -0.25\pi$ and $\varphi_{MD} - \varphi_{EQ} = 0.92\pi$, while the other set is $\varphi_{ED} - \varphi_{EQ} = -0.75\pi$ and $\varphi_{MD} - \varphi_{EQ} = 0.08\pi$. The calculated Fourier space image of the multipolar radiation is shown in Figure 3.8(c), and agrees very well with the experimental measurements. These results also agree qualitatively with earlier theoretical results of the complementary metal-dielectric-metal structures [26].

To perform multipole decomposition described in Eq. (3.3), both the phase and amplitude of the phase is required. How-

ever, in this section we want to verify the multipole nature of the metasurface from its experimentally measured radiation pattern which we only record the amplitude. That is why here we use approximations by fitting. From Eqs. (3.7)–(3.9), we find out the far-field radiation pattern of the first three terms of the multipole decomposition and fit their complex coefficients so that an array of the fitted multipole will exhibit the same radiation pattern as recorded in our experiment. Due to this reason, we stated that the phase difference of the multipoles might have multipole fitting solutions. But through this analysis we know at least that the magnetic dipole mode indeed exists in this metasurface and its amplitude is comparable to the electric dipole mode.

3.4 Multipolar THG from Dielectric Nanostructrues

While the MIM nanostructures discussed in previous Section 3.3 show interesting results, it is known that metallic structures have limitations in their efficiency and functionalities at optical frequencies imposed by Ohmic losses, small mode volumes and low laser damage threshold. This limits the further progress and applications of nonlinear optics at the nanoscale.

Dielectric resonant nanostructures can overcome many of such problems since their optical losses in visible and near-IR wavelengths are almost negligible [66]. Such nanoparticles can support electric and magnetic Mie-type resonances enabling directional scattering of light by compact optical nanoantennas [86,87, 152–154]. For dielectric nanoparticles, nonlinear effects can be enhanced substantially near the resonances which may involve higher-order multipolar response [72, 155–158]. The interference of these multipoles defines the conversion efficiency of the nonlinear process [31].

Silicon (Si) nanoparticles were first explored for nonlinear effects at the nanoscale due to their large third-order nonlinear susceptibilities [155, 159, 160]. The study of THG from isolated silicon nanodisks revealed that the field localization at the magnetic resonance can result in two orders of magnitude enhancement of the harmonic intensity with respect to unstructured bulk

silicon [155, 160]. Later, third-harmonic was studied in Ge nanodiscs [161]. The study revealed the importance of interference effects. In particular, it demonstrated enhancement of the third harmonic by the excitation of the near-field anapole mode. These findings suggest novel opportunities for engineering the nonlinear response at the nanoscale with dielectric resonant nanostructures.

Pairing up two isolated nanoparticles and creating dimer nanoantennas enriches multipolar behavior in both linear and nonlinear regimes. The effects of multipolar mode decomposition on linear optical properties have recently been reported by several groups [71, 153, 154, 162–167]. It was observed that coupling between the resonant nanoparticles placed in a close proximity allows for a substantial enhancement of both electric and magnetic fields via hybridization of individual electric and magnetic modes, and it gives an additional degree of freedom to engineer the directional scattering. However, the effect of hybridized modes supported by dielectric dimers on their nonlinear optical properties remains unknown.

Here we provide numerical and experimental studies of THG from symmetric silicon nanodimer. The nanodimer exhibits enhanced nonlinear conversion efficiency of $\approx 2 \times 10^{-6}$ compared to $\approx 1 \times 10^{-7}$ of single disk [155]. We demonstrate the control of directionality of the third-harmonic radiation due to the multipolar interference effects and near-field enhancement. More specifically, we demonstrate that geometry-dependent multipolar modes in silicon dimers allows effectively shaping and switching of the nonlinear third harmonic radiation pattern, its intensity and directionality, as presented schematically in Figure 3.9 where an insert shows an SEM image of one of the fabricated Si dimer samples.

3.4.1 Experimental and numerical techniques

We fabricate the dimer samples from polycrystalline silicon on a fused silica substrate (500 μm) using the electron-beam lithography (EBL). Each nanodimer is created by two identical silicon nanodisks, as shown in the insert in Figure 3.9. We fabricate a

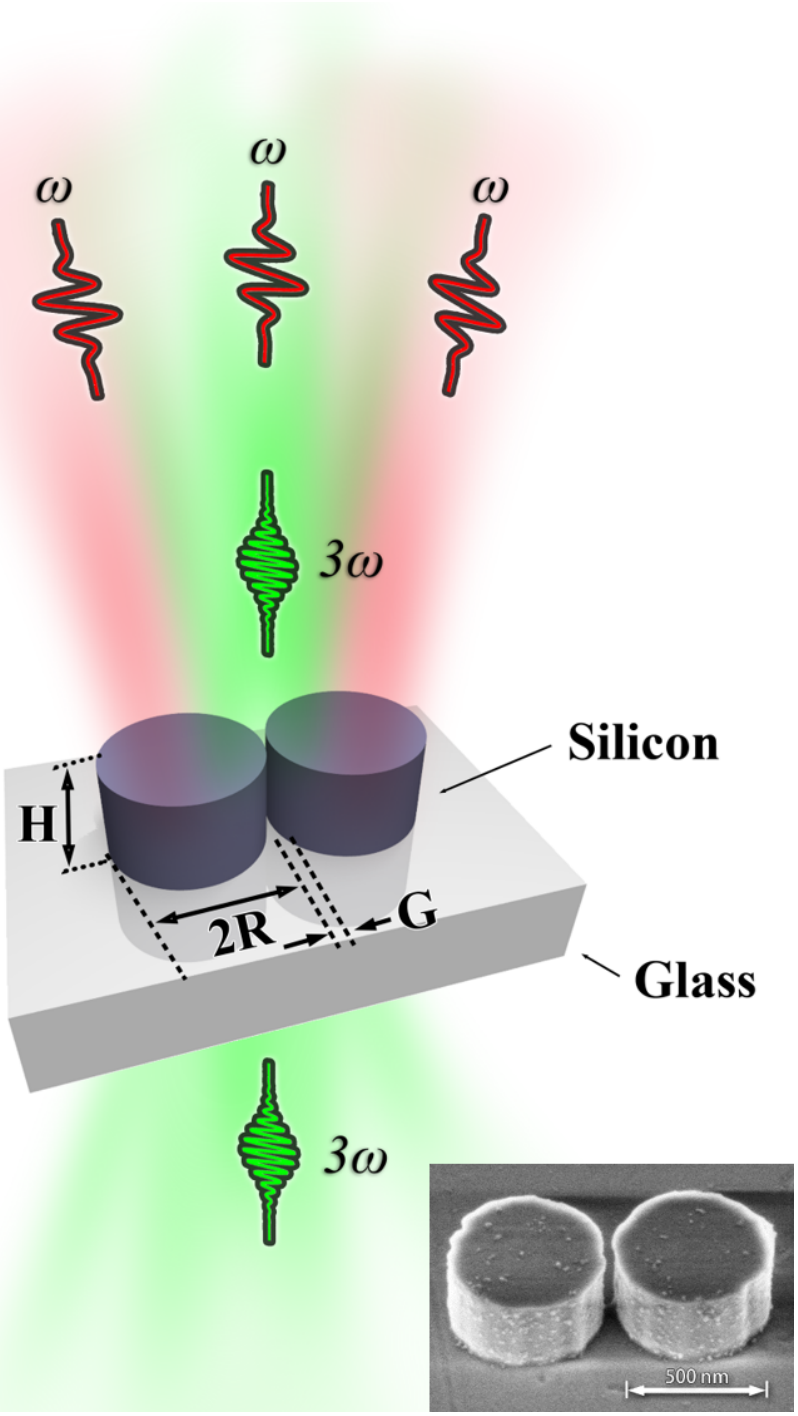

Figure 3.9: Schematic of a third-harmonic generation in our system. A dimer nanoantenna is composed of two silicon nanodisks. Inset: SEM image of the dimer.

wide range of dimers with varying disk radii ranging from 200 nm to 300 nm. The dimers have an identical height of $H = 300$ nm, and each dimer has a well-controlled gap between the neighbors of $G = 20$ nm. For the nonlinear experiments, we place an isolated nanodimer in the focal spot of two confocal air objective lenses. The numerical apertures of these lenses (NA= 0.85 of the forward collecting objective, and NA= 0.9 of the pumping /backward collecting objective) corresponds to the allowed collecting half-angles of 58 and 64 degrees for the third-harmonic emission, respectively. We optically pump the dimer with a femtosecond laser with 1556 nm central wavelength and control the pump polarization. We use two cooled CCD cameras to detect the third-harmonic radiation, its power and directionality diagram. More details on this method of optical characterization can be found in Section 3.2.3.

To design dimers and predict their linear and nonlinear optical properties, we apply the wavelength-dependent complex-value refractive index of silicon [168], and perform numerical simulations using finite element method (FEM) solver of COMSOL Multiphysics, following the method described in Refs. [72, 159, 160]. To achieve the high nonlinear THG conversion with single symmetric silicon dimer, we are primarily guided by the resonant enhancement of the local fields at the fundamental wavelength (FW). Therefore, we first study the linear scattering characteristics at our laser operating wavelength 1556 nm. To optimize the geometry, we scan the radius R for fixed disks thickness of $H = 300$ nm and constant interparticle gap $G = 20$ nm, as shown in Figure 3.10. The plotted scattering efficiency per one disk is defined as $Q_{sca} = C_{sca}/S_0$, where C_{sca} is the scattering cross section and $S_0 = \pi R^2$ is the area of the disk. We further characterize the optical scattering features by multipolar expansion.

We perform the multipolar decomposition using the polarization currents induced inside the nanoparticles. We choose this method over the decomposition of the scattered fields as the presence of a substrate makes it difficult to rigorously perform multipolar analysis using the scattered fields. When calculating

the contributions associated with each multipole, the fields are considered to radiate into air, which makes the sum over multipoles contributions (defined as Total Qsca here) to be lower than the actual case [166].

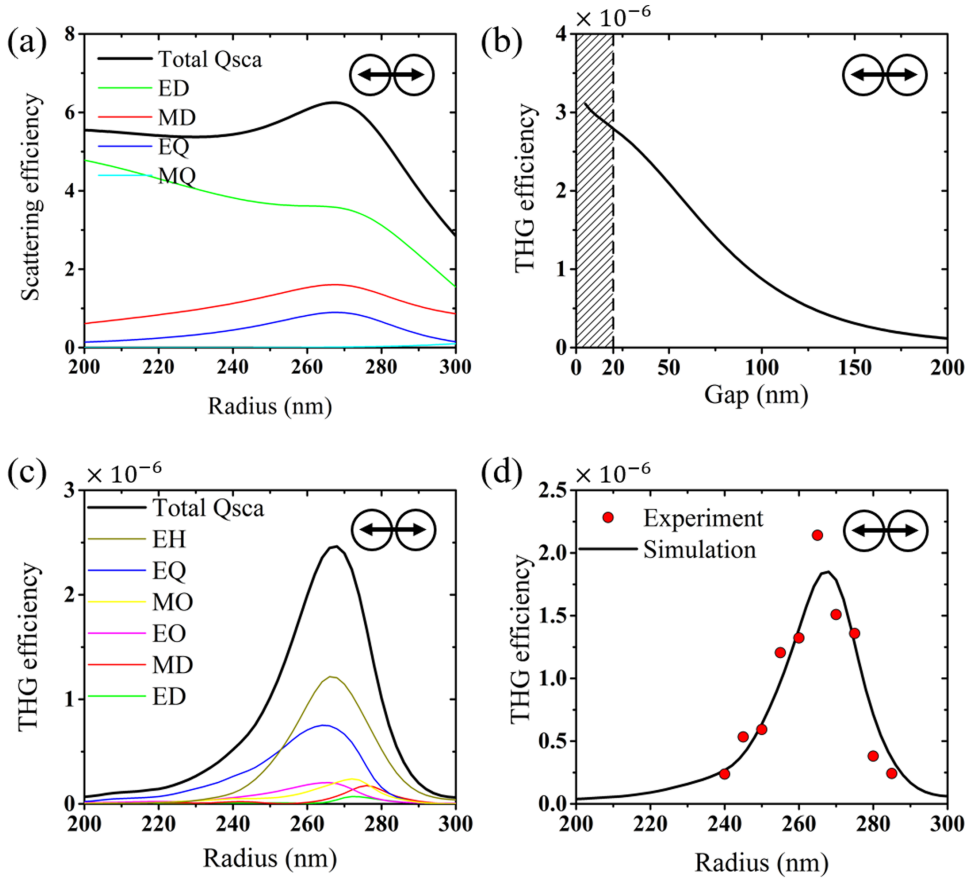

Figure 3.10: (a) Calculated total linear scattering efficiency (black curve) of the silicon dimer nano antenna with fixed gap size $G = 20$ nm and varying disk radius. Contributions of leading multipoles in the multipolar decomposition of the calculated electromagnetic field are shown in colored curves. (b) Dependence of the THG conversion efficiency on the gap size at fixed radius $R = 270$ nm. (c) Calculated THG efficiency versus radius and its multipole contributions. (d) Experimentally measured (dots) and calculated (line) portion of the total THG efficiency captured by the two collecting objectives. The results shown are for the fixed gap $G = 20$ nm and varying disk radius. Abbreviations: E – electric, M – magnetic, D – dipole, Q – quadrupole, O – octupole, H – hexdecapole. Insets show the polarization of pump.

As can be seen in Figure 3.10(a), the largest scattering efficiency occurs for $R = 270$ nm, being determined mainly by contributions from the electric dipole (ED), magnetic dipole (MD), and electric quadrupole (EQ).

Next, the nonlinear polarization induced inside the nanoparticles is used as an input for the next electromagnetic simulations at the TH frequency to obtain the generated TH field. For

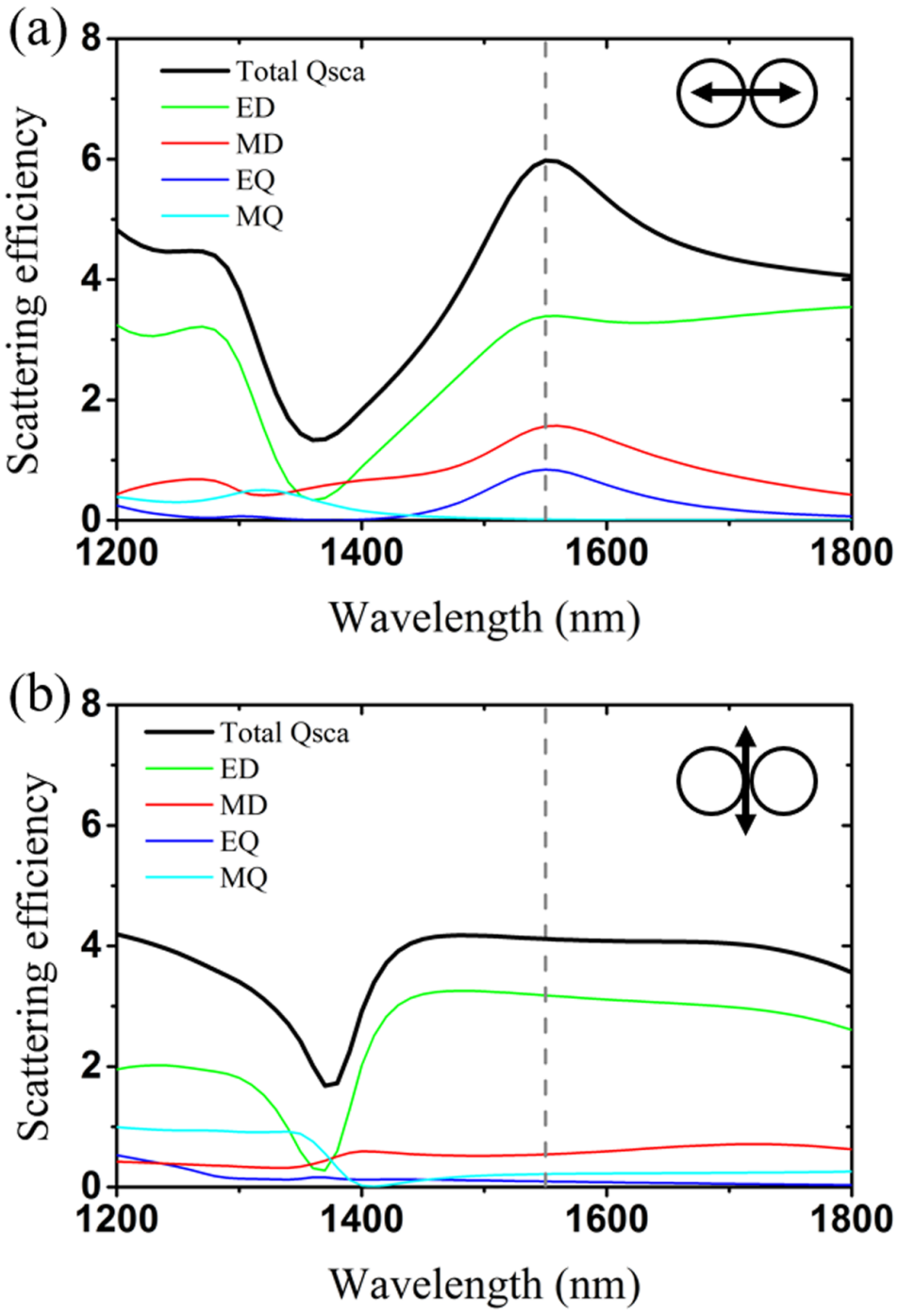

Figure 3.11: (a) Calculated linear scattering efficiency and related multipolar decomposition for a silicon dimer with $R = 270$ nm and $G = 20$ nm excited by horizontally polarized polarized (a) and vertically polarized (b) pump laser beams, respectively.

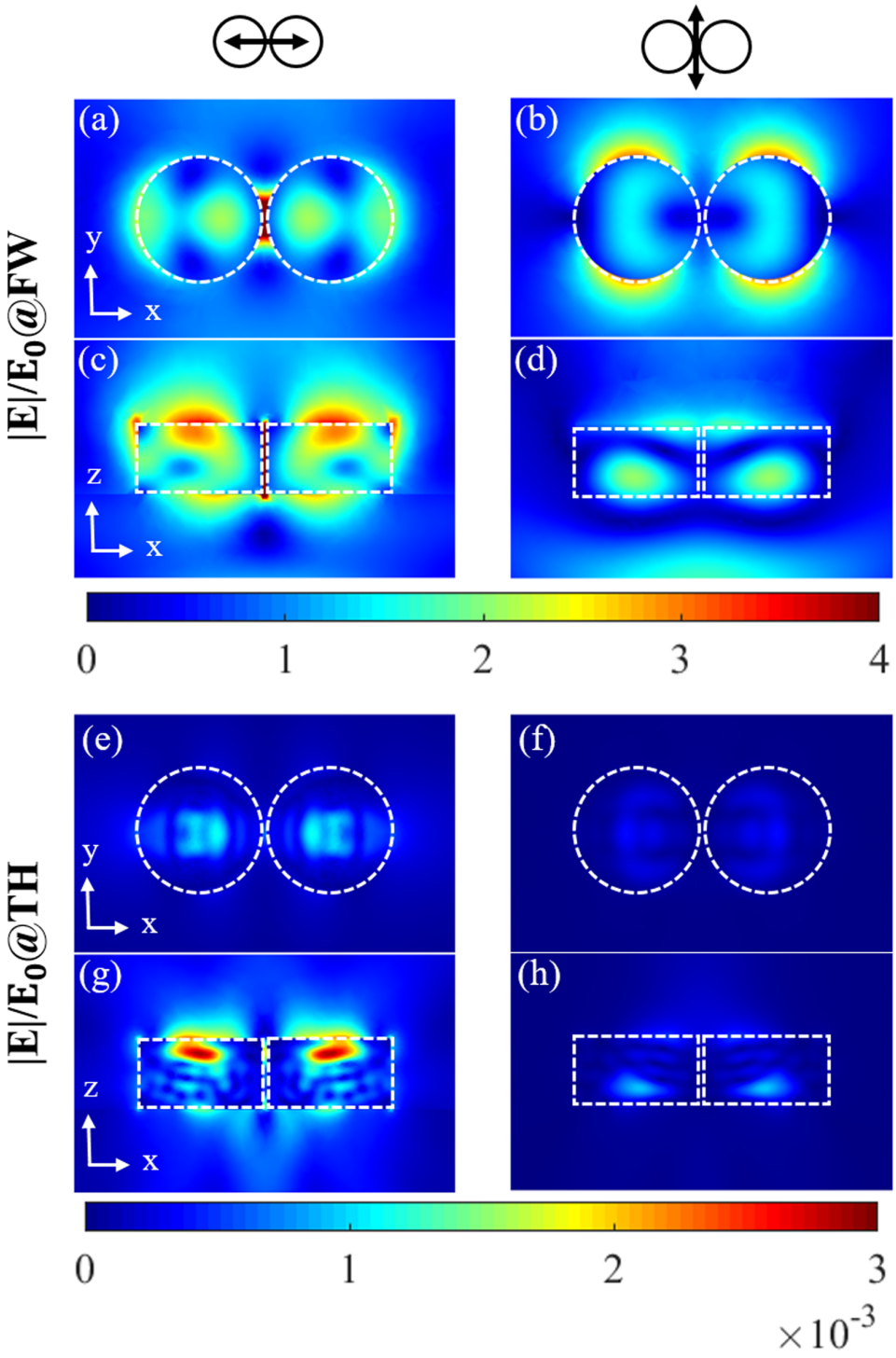

Figure 3.12: Top and side views of the electric field distributions at fundamental wavelength (FW) and third harmonic (TH) in the silicon dimer antenna for two polarizations. The antenna has 270 nm disk radius and 20 nm interparticle gap.

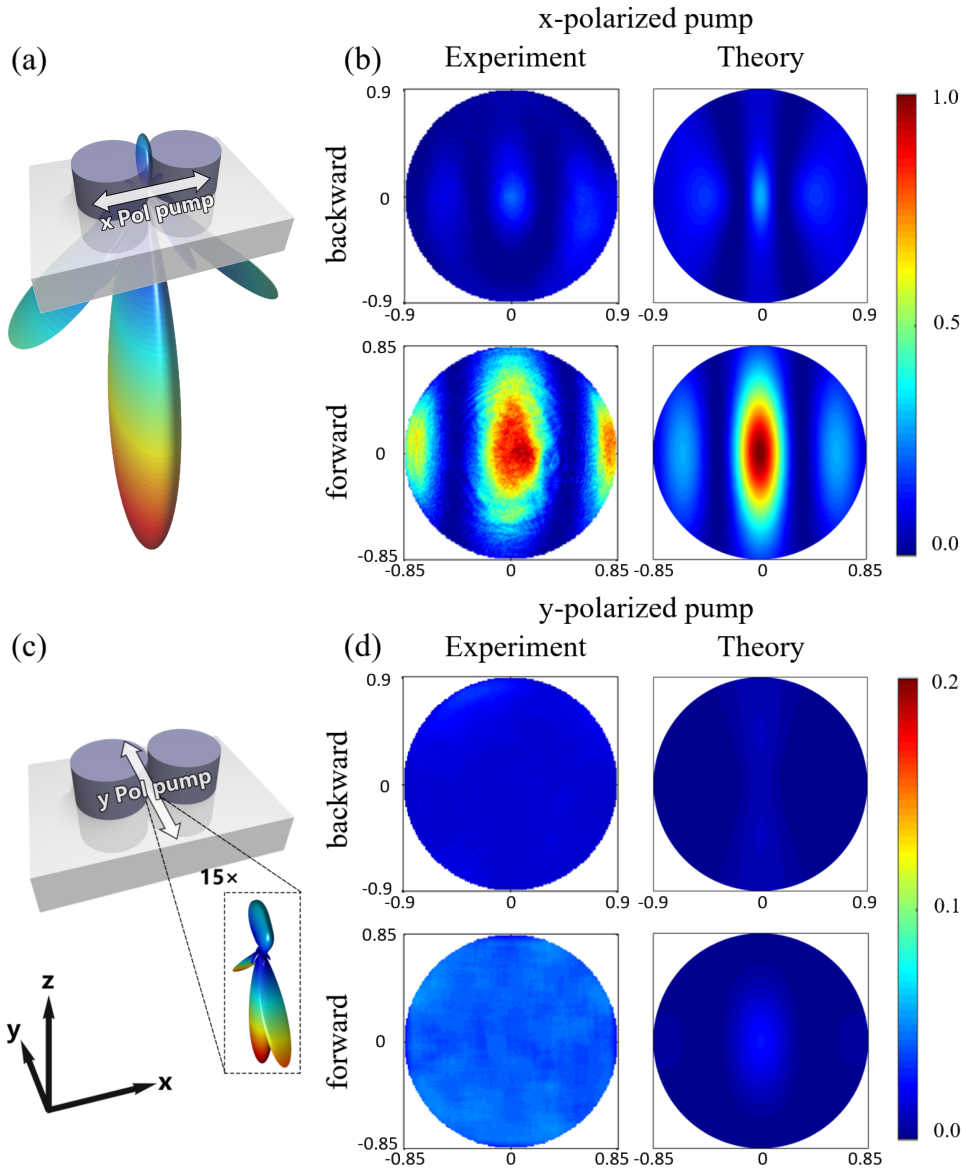

Figure 3.13: Radiation patterns of THG for x (a,b) and y (c,d) polarized excitations. (a,c) Calculated three-dimensional directionality of TH emission. (b,d) Two-dimensional projections of three-dimensional directionalities measured and calculated within the numerical apertures of the objectives. The projections are shown in forward and backward directions with respect to the direction of pump. The axes of plots in (b) and (d) are the sine of radiation angle. The collecting angle is limited to numerical apertures of 0.85 and 0.9 for forward and backward objectives. In (b) the color is normalized to the peak value of forward radiation, demonstrating the contrast ratio of the unidirectional TH emission. Since the THG signal excited by x-polarized pump is more than 20 times stronger than that by y-polarized pump, in (d) the color scale is set to 0.2 of that in (b), increasing the apparent intensity of radiation with y-polarized pump 5 times so that the pattern of the much weaker THG signal by y-polarized pump can be seen.

centrosymmetric materials, such as silicon, THG is an essentially bulk phenomenon with negligible surface contribution [169]. Here, we take into account only volume nonlinearities of silicon, and neglect its surface nonlinearities as of minor importance. Figure 3.10(b) shows the rising trend of THG conversion efficiency at $R = 270$ nm with decreasing the gap size. Due to the precision limit of the EBL fabrication process, we use $G = 20$ nm to robustly create the nanodimer without linking the gap between the two disks by fabrication fluctuations. Figure 3.10(c) shows the contributions from each multipole radiated at TH. The largest THG conversion efficiency also occurs at $R = 270$ nm, corresponding to the typical resonant profile at the fundamental wavelength.

3.4.2 Control of nonlinear radiation

We measure the THG efficiency from our samples with increasing disk radii at fixed gap size $G = 20$ nm. We calibrate the cameras with a power meter. The measured THG conversion efficiency is shown with red solid dots in Figure 3.10(d). The maximum efficiency reaches 2×10^{-6}. We also calculate the THG efficiency within the numerical apertures of the collecting objectives as utilized in our experiment. The respective theoretical dependence is plotted with a solid line. The position of the maximum THG conversion efficiency in Figure 3.10(d) overlaps with the peak of the calculated linear scattering efficiency in Figure 3.10(a).

Figure 3.11(a-b) show the computed linear scattering spectra for the dimer with the optimized disk radius $R = 270$ nm. We assume light normally incident from the air side with linear polarization that is either horizontal (a) or vertical (b). In Figure 3.11 we see a pronounced peak in the scattering for horizontal polarization that is not present for vertical polarization. This modification of the scattering spectrum arises from coupling between the nanoparticles in the dimer. The spectral position of the peak matches the pump wavelength of our laser.

The far-field spectra are dominated by the following multipoles: ED, MD and EQ in Figure 3.11(a) and ED, MD and

magnetic quadrupole (MQ) in Figure 3.11(b). All of them stem from hybridization of electric and magnetic dipolar resonances of single scatterers, being qualitatively the same as described in Refs. [162, 164]. Remarkably, the modes of coupled particles are known to play important role in the analysis of the nonlinear response for both plasmonic [170, 171] and dielectric [160] nanostructures.

The calculated electric near-field distributions at the fundamental and harmonic wavelengths for x and y polarized irradiance are depicted in Figure 3.12. The FW near-field distributions are clearly seen to be determined by hybridized modes associated with electric and magnetic dipolar excitations inside the discs [163, 164, 167] as shown in Figure 3.12(a). For x-polarized pump, the electric-field hotspot naturally occurs in the gap between two silicon nanodiscs [166]. Strong field localization in coupled nanoantennas and electric field enhancement furthermore stimulate the nonlinear response in the nanoparticles. THG is predominantly governed by magnetic dipoles in linear regime [159, 160], as reflected in the symmetry of the generated linear field in Figure 3.12(c), also shown in Figure Figure 3.10(a). The THG field is shown in Figure 3.12(g) and its multiple analysis result is shown in Figure 3.10(c), where the EH and EQ modes are the major contributors.

Because of the different physics as compared to second harmonic generation (SHG) in coupled metal nanoparticles [170–172], no localization to the gap and far-field silencing [171] of the nonlinear response is observed. As follows from Figs. Figure 3.11 and Figure 3.12, the linear scattering is quite sensitive to the polarization of the impinging light. The magnitude of the electric near-field and the induced magnetic dipole moments are stronger for x-polarized pump promoting the largest coupling strength. Being raised to the third power in the nonlinear regime, this effectively switches THG on/off as the pump polarization is changed from x to y.

To observe these phenomena in experiment, we measure the third-harmonic radiation patterns by capturing their directionality diagrams. This is done in forward and backward direc-

tions with respect to the direction of pump. For this we project onto the camera's back-focal plane (Fourier space) images of our objective lenses. We perform matching numerical simulations where calculated TH far-field intensity distribution is projected onto the back focal plane [75, 173]. As shown in Figure 3.13, the experimentally measured directionality of THG has the forward to backward ratio around 11:1, indicating highly directional nonlinear harmonic generation. The highly directional nonlinear scattering in Figure 3.13(a) is defined by two higher-order electric multipoles EQ and EH. Numerical simulations predict a remarkable polarization-dependent contrast in nonlinear signal: the third-harmonic power for x-polarized pump is more than 30 times larger than the power for the y-polarized pump. The experimental measurements for the y-polarized pump appear below the noise level, but there is at least a 20:1 distinction ratio.

3.5 SHG in III-V nanostructures

Shaping the radiation and polarization patterns of second harmonic generation (SHG), including achieving unidirectional harmonic generation or nonlinear generation of beams of complex polarization is also studied in our research. We obtained efficient SHG from a dielectric AlGaAs nanoantenna and demonstrate the possibility of shaping the second harmonic (SH) radiation pattern in forward and backward directions as well as its polarization state. (Briefly demonstrated in Figure 3.14 and more details can be found in [72,73]) In particular, we prove that the SHG emission has a complex spatial distribution of its polarization state, which, for a specific size of the nanoantennas, leads to the generation of cylindrical vector beams of radial polarization. The properties of our SHG nanoantennas are enabled thanks to a new AlGaAs platform, which allows for simultaneous forward and backward radiation. Our results demonstrate for the first time to our knowledge the functional beam and polarization shaping of nonlinear second harmonic emission from dielectric nanoantennas. This represents a fundamental step for

the manipulation of the angular emission of AlGaAs nanoantennas, which will foster future studies toward the goal of precision engineering of their nonlinear radiation pattern.

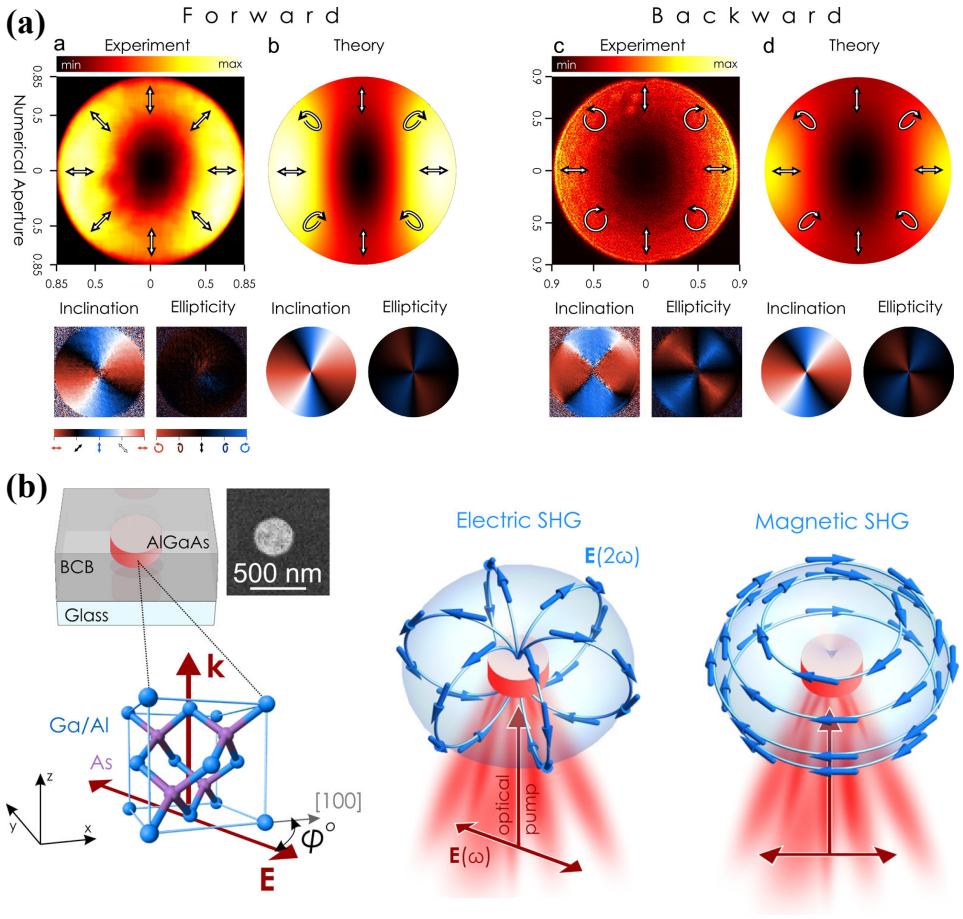

Figure 3.14: (a) Directionality and polarization diagrams of the SH signal. Top row: directionality diagrams in a,b forward and c,d backward directions. a,c Experimental measurements and b,d theoretical calculations. Arrows visualize the polarization states. Bottom row: experimentally retrieved a,c and theoretically calculated b,d polarization inclination angles and ellipticity for the directionality cases of the top row. The incident beam is linearly polarized along the vertical direction. (b) Left: Schematic structure and SEM image of fabricated individual AlGaAs nanoantenna. Crystalline structure of AlGaAs and relative directions of optical pump propagation k and electric field E. Right: Concept images of distinct polarization patterns of electric and magnetic second harmonics for the simplest cases of dipolar radiation.

We also observed directly the nonlinear optical magnetism in AlGaAs nanoantennas by analyzing the polarization states of the nonlinear emission. Our experiments are supported by the multipolar field decomposition. We have demonstrated a control over a continuous transition between electric and magnetic nonlinear responses by tuning polarization of the optical pump (see Figure 3.14(b)).

3.6 Summary

We have studied both by theory and experiment the radiation pattern and nonlinear harmonic generation from nano structures. From that the multipolar resonance is analyzed and used to control the directionality and polarization dependency of the nonlinear generation. Negative refractive index, magnetic resonance mode and enhanced nonlinear process are closely related. This chapter emphasis the experiment technique to verify the multipole nature of the resonance. Using the back-focal plane analysis, we find the magnetic dipole mode is about similar contribution as the electric dipole mode. With linear simulation and experiment of measuring negative refractive index, we prove the same cause of nonlinear enhancement from different perspectives. The phase modulation will be discussed in Chapter 4 and the current list of researched properties of nonlinear nanostructures is given in Table 3.1.

Table 3.1: Study of Nonlinear Nanostructures

	Theory	Experiment
Radiation pattern	✓	✓
Multipole Resonance	✓	✓
Directionality	✓	✓
Polarization	✓	✓
Phase Modulation	See Chapter 4	See Chapter 4

Nonlinear Wavefront Control

4.1 Introduction

The recently highlighted and rapidly expanding interest to optical metasurfaces is explained by many unique opportunities for functional flat optics and optical elements which would allow high-precision control over light wavefront transmission, reflection, and polarization [2]. The next important breakthrough is expected with nonlinear metasurfaces which are considered to bring a paradigm shift to nonlinear optics [174]. The exploitation of nonlinear optical response of metasurfaces is expected to revolutionize the subwavelength photonics enhancing substantially the nonlinear response of natural materials that can be combined with an efficient control of a nonlinear phase. Here we study metasurfaces based on Mie-resonant nanostructures that have recently been suggested as an important pathway to enhance nonlinear efficiency beyond any limits introduced by plasmonics [66, 175, 176]. The important question in that field is how to employ low-loss dielectric nanoparticles for creating high-efficient functional nonlinear metasurfaces.

We suggest a novel concept of resonant phase accumulation in dielectric metasurfaces when both electric and magnetic Mie multipoles are excited simultaneously with comparable amplitudes. Being assembled into a planar structure, the dielectric resonators allow for the creation of smooth phase gradients for the generation of the third-harmonic field. In order to achieve the desirable high nonlinear conversion efficiency as well as the full range phase control, more degrees of freedom of parameters are considered in the design process. An artificial intelligence (AI) assisting approach (Briefly discussed in Section 4.2) is used

to guide the numerical calculations so that the solutions can be reached swiftly.

To demonstrate our result, the experimental measurements of the nonlinear phase modulating metadevices are shown in Section 4.3 specifically as the first example of a functional nonlinear metasurface for the generation of the third-harmonic signal in any desired direction. It is demonstrated that our nonlinear metasurface produces phase gradients in a full 0–2π phase range providing 92% diffraction efficiency for the nonlinear wavefront control. This work is already submitted in February 2018. Other functionality including nonlinear flat lens, nonlinear donut beam generation, nonlinear polarization multiplexing and nonlinear holograms are also studied and pending drafting. Overall I lead the nonlinear wavefront control projects in term of numerical calculation for designing and experimental measurements.

4.2 Intelligent Photonic Designing

For complex design of delicate nanostructures, the number of design parameters might increase. The search space will grow by a power relation to the parameter number (degrees of freedom). Two parameters with 100 samplings will only need 10^4 calculations, while 4 parameters with same sampling number will result in 10^8 calculations. This will quickly deplete the computing power even with supercomputers, as CPU power only grow proportionally to CPU cores (even less if intercommunication between cores is considered). The time consumption will be unacceptable using a parameter sweep. Another prospect is data analysis. For low degrees of freedom it is possible to run rough sweeps and check the results to locate the region of interest. However degrees of freedom larger than 3 will result in higher dimension (>4) dataset and thus is very hard to visualize or understand. The so called AI is what can calculate the gradient of fitness in high dimension and find the quick path for calculation toward optimization.

Deep learning, and other types of machine learning methods have drawn great attention after the news of AlphaGo win-

ning human Go masters event. Following that there is a trending research phenomenon that various types of artificial intelligences being utilized in nanophotonic designing. From optimizing nanostructures [177], designing metasurfaces [178], to performing complicated phase retrieval [179], intelligent methods are more and more often used. The definition of the term AI is ambiguous. Recently it is brought to attention by the success of Deep learning. But in fact, the programs that runs themselves for automatic optimization fall into the AI category. Within Deep-learning, where multiple layers of coefficients are tuned to gradually simplify the complex problems, there is also similar multidimensional problems where some kind of intelligent gradient descent methods are used. In my intelligent photonic designing approach, similar gradient descent methods are used to guide numerical simulations. Sketch of the artificial intelligence (AI) assisted design method for the nonlinear phase modulation is shown in Figure 4.1, where the intelligent assist program is used to guide the COMSOL multiphysics simulation in search of optimized parameters for the phase-only modulation. I write the algorithms in a MATLAB program that controls and analyses the COMSOL simulations with a protocol called Livelink.

For the ease of easy demonstration, the AI-assisted design result of a super high THG conversion efficiency metasurface is shown in Figure 4.2. There is only one design fitness objective: in this case the efficiency. The 4D parameters are shown by plotting the fitness vs each three combinations of parameters in a 3D grid. The fitness is represented by the size of the sphere. In this way the 5D data of the result can be somehow visualized. These calculations can be correlated to the theoretic predictions in [180] and we are planning to perform experiments in the near future.

4.3 Nonlinear Phase Modulating Meta-devices

The exploitation of the nonlinear optical response of metasurfaces opens up new degrees of freedom and offers a paradigm shift in nonlinear optics [174, 181]. Nonlinear metasurfaces are expected to revolutionize subwavelength photonics by enhancing

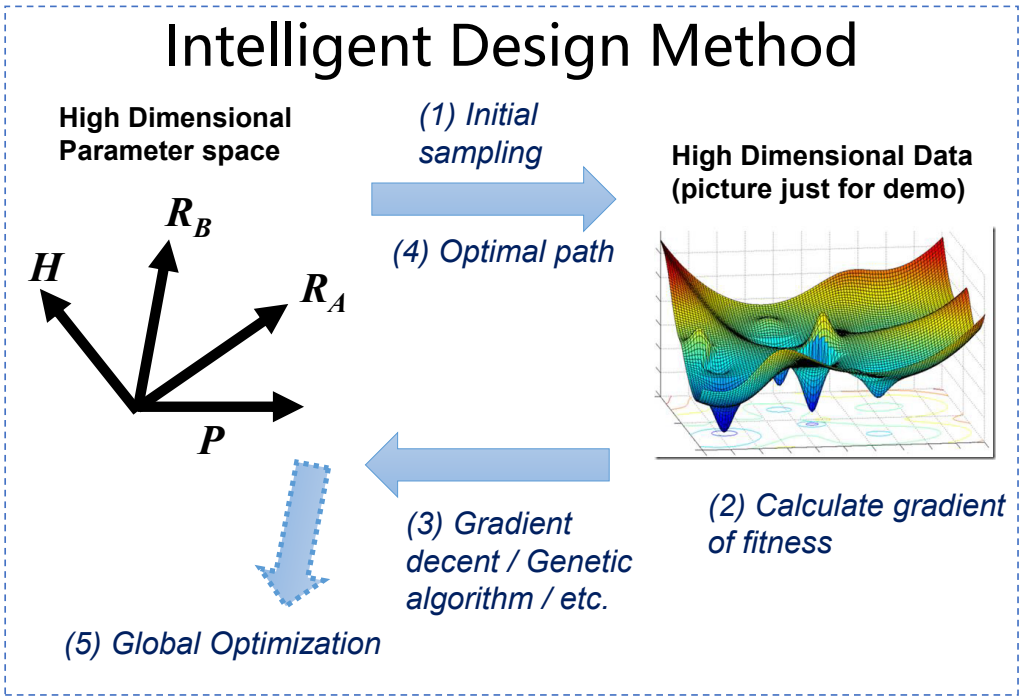

Figure 4.1: Workflow of the AI assisted designing. (1) Initial random samplings are calculated within the parameter space and pre-defined boundaries. (2) The performance of the nanostructures based on the design requirements are quantified using multi-objective fitness function. (3) The fitness values vs parameters hold a certain relationship and their gradients are calculated and analyzed using suitable methods. (4) Optimal path for next-step calculations are given by the AI, so that a fast convergence to optimal can be quickly reached. (5) After several iterations, the optimization of design can be reached.

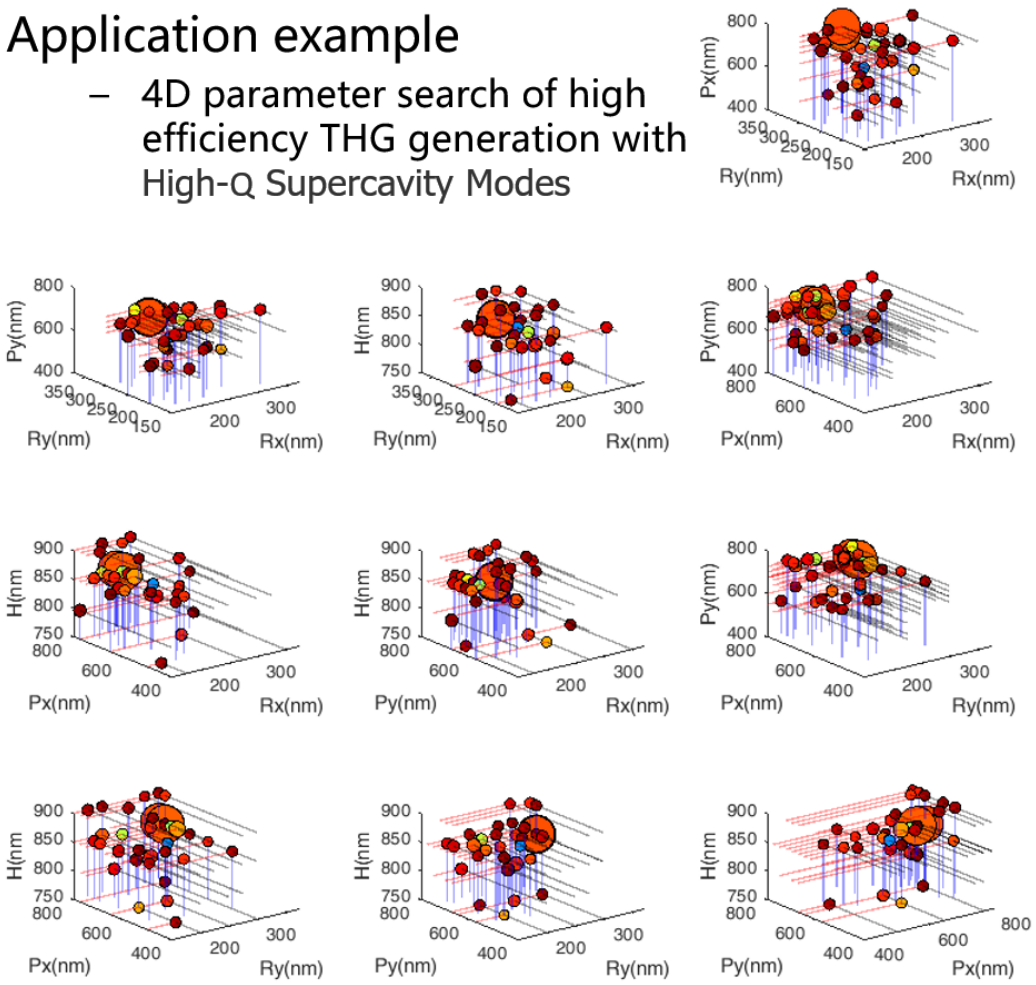

Figure 4.2: AI-assist design example: 4D parameter search of high efficiency THG generation with high-Q supercavity modes. Each picture shows the fitness function versus three out of the five parameters Rx, Ry, Px, Py and H. This is an example for visualizing the high dimensional parameter optimization. The shown case is a snapshot of the whole process. The reason of showing this is to demonstrate the difficulty for human eyes to find the optimization point when there are more than 2 parameters as the variable of the function.

substantially the nonlinear response of natural materials combined with efficient control of the phase of the nonlinear wave. Here we suggest a general approach for arbitrarily engineering the wavefront of parametric waves generated by a nonlinear metasurface and demonstrate it for a highly-efficient nonlinear metasurface generating the third-harmonic signal in a desired direction.

To demonstrate our approach, we designed a silicon-based metasurface assembled from a set of 10 different elliptical nanopillar resonators, each of them providing similar conversion efficiency but accumulating a different phase for the third-harmonic signal spanning the full 0–2π range. While all previous demonstrations [17–22, 174, 181] of nonlinear wavefront control with plasmonic metasurfaces relied on geometric phase, here we achieve wavefront control via resonant phase accumulation in the dielectric metasurface when both electric and magnetic Mie multipoles are excited simultaneously with comparable amplitudes. Geometric phase is a special term which means phase tuning by rotating the same meta-particle. It can provide versatile and broadband operation, but with low efficiency. The resonance phase modulation has an optimum operating wavelength and can be highly efficient. When assembled into a planar structure, these dielectric resonators allow the creation of smooth phase gradients in the generated third-harmonic field. As an example, here we demonstrate a nonlinear beam deflector that generates a third-harmonic beam at a selected angle with respect to the direction of the pump beam.

4.3.1 General Theoretical Approach

Here we employed a set of silicon nanopillars as building blocks for our nonlinear metasurfaces. We required each nanopillar to provide highly-efficient third-harmonic generation (THG) with forward directionality. We further required that the different pillars would provide similar amplitudes of the third-harmonic (TH) but different phases ranging from 0 to 2π. This could be achieved via the interplay between the Mie resonances of a single nanopillar at both the pump wavelength and the TH wavelength.

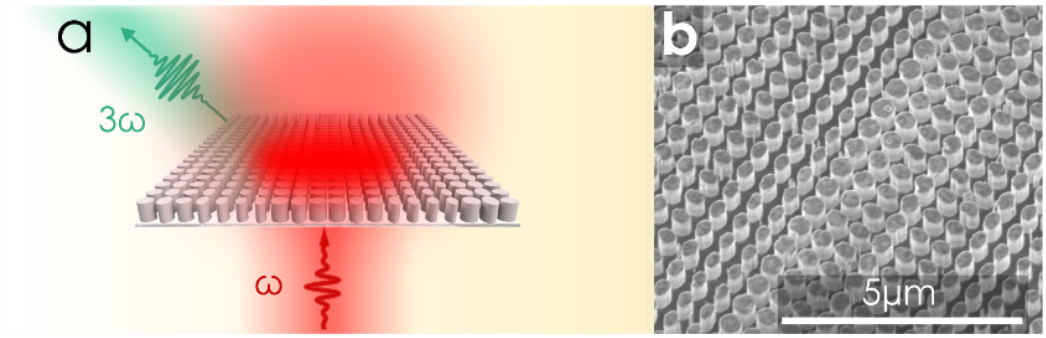

Figure 4.3: Nonlinear functional metasurface. (a) Concept image of a nonlinear beam planar deflector based on a dielectric metasurface assembled from a set of ten different silicon nanopillars. (b) Scanning electron microscope image of the fabricated highly efficient beam-deflector metasurface.

We employ the multipolar analysis known to be a powerful tool for engineering the wavefront of linear metadevices [30]. We extend this approach of the wavefront control to the case of nonlinear response. We consider pillars that at the pump wavelength support electric and magnetic dipole Mie resonances. Correspondingly, at the TH wavelength they support several higher-order multipoles as their optical volume increases. This yielded an analytical treatment for the intensity of the third harmonic in both the forward (F) and backward (B) directions in terms of multipoles having even or odd parity with respect to the vertical reflection symmetry (Vertical means the symmetric line passes through from top to bottom):

$$B = \left| E_{even}^{(3\omega)} - E_{odd}^{(3\omega)} \right|^2 \tag{4.1}$$

$$F = \left| E_{even}^{(3\omega)} + E_{odd}^{(3\omega)} \right|^2 \tag{4.2}$$

where $E_{even(odd)}^{(3\omega)}$ is the TH electric field generated by all even (odd) multipoles. Eq. (4.1) suggests that the necessary condition for high-efficient forward directionality requires the balance between the even and odd multipoles.

$$E_{even}^{(3\omega)} = E_{odd}^{(3\omega)} = |E|\, e^{i\varphi} \tag{4.3}$$

Therefore, the total field of the third harmonic in the forward

direction $E^{(3\omega)}$ is

$$E^{(3\omega)} = E^{(3\omega)}_{even} + E^{(3\omega)}_{odd} = 2\,|E|\,e^{i\varphi} \tag{4.4}$$

In this study it is not fully study for the off-axis radiation of the nonlinear phase modulation. Paraxial approximation for the phase modulating as well as its applications. By shaping the pillar geometry, a full 2π phase coverage with uniform amplitude can be achieved keeping high forward directionality at the same time. Importantly, as the nano-cylinders are optically resonant at both the pump wavelength, and the TH, the multipolar resonances at the TH are inevitably of higher order multipoles making the decomposition to go beyond the dipole and quadrupole approximations. The balance of multipoles with opposite parities required by Eq. (4.3) leading to the unidirectional pattern represents the generalized Huygens condition [5,62,64] extended to the case of nonlinear harmonic generation.

Alongside these theoretical considerations we performed full-wave nonlinear simulations using the finite element method solver of COMSOL Multiphysics. We note that calculations of third-harmonic are computer-intensive as they require at least a 3^3 times finer mesh compared to linear calculations. Moreover, to find the best geometries, our calculations considered 4-dimensional parameter space (comprising pillar height, two elliptical axes, and the unit cell size), resulting in large total volume of the 4D parameter space. To minimize the demand for computing power we implemented the gradient descent method in the COMSOL calculations Section 4.2. This method analyses the calculated data sets and learns how to find the quickest route to optimization and is commonly used in machine intelligence, in particular, as a subset of the deep-learning method. Details of numerical simulations are provided in Methods: Numerical calculations. The resulting design is a set of particles with a height of 617 nm in a square array with 550 nm period, and elliptical cross-section with the axes values ranging between 320 nm and 535 nm [see Figure 4.4 for the details of the nanopillar geometry]. This range of geometrical parameters allows a full 2 phase coverage in the THG to be achieved whilst maintaining similar amplitudes.

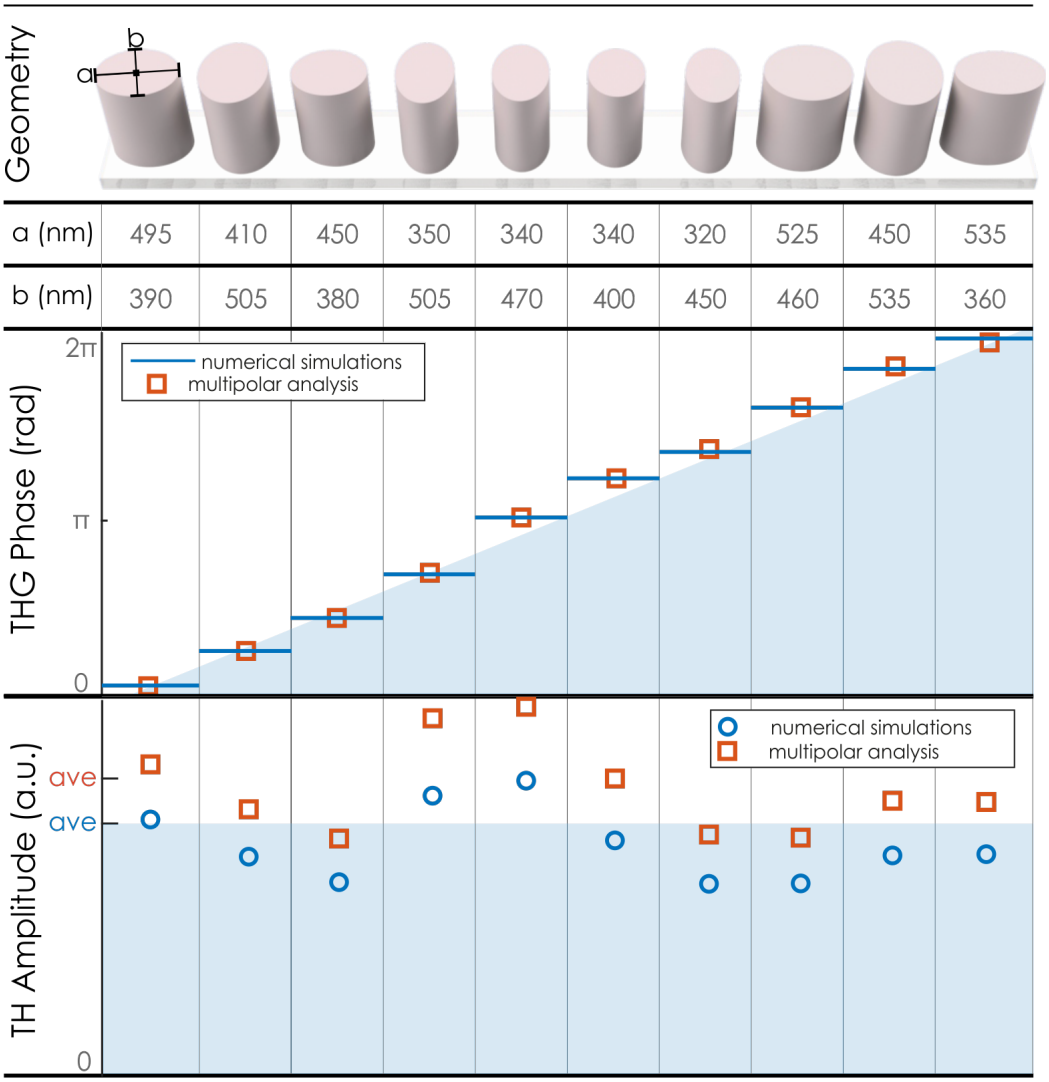

Figure 4.4: Geometries, nonlinear phases, and THG amplitudes of nanopillar meta-atoms. Shown are geometrical sizes, and corresponding analytical and numerical results on the phase and amplitude of the total electric field of the third harmonic in the forward. The results are for the optimal pump wavelength of 1615 nm and linear polarization of the pump along a-axis.

We compare our analytical and numerical results (shown in Figure 4.4) and find that calculations of phases of the TH are in a perfect agreement. Calculations of amplitudes have a small and consistent offset that we associate with the effect of the substrate. Our analysis shows that at the pump wavelength the pillars forward-scattering is dominated by 1st order multipoles: electric and magnetic dipoles, and correspondingly the third-harmonic is dominated by first 3 orders of multipoles: electric and magnetic dipoles, quadrupoles and octupoles [see details in the supporting information of [182]]. Importantly, the sum of contributions of all even multipoles to the TH is similar to the sum of contributions of all odd multipoles. Thus, our system allows to satisfy Eqs. (4.3) and (4.4) and to achieve the generalized Huygens condition in nonlinear regime, which provides a full 2 phase coverage combined with the similar TH amplitude in the forward direction for all the nanopillars (see Figure 4.4). Full-phase coverage combined with nearly the same intensity of forward-generated TH allows for an efficient arbitrary complex wavefront shaping in nonlinear regime.

4.3.2 Experimental Demonstration

To demonstrate the capabilities for nonlinear wavefront control, we fabricated a nonlinear beam deflector: a metasurface that generates a beam of light at the third harmonic wavelength propagating at an angle to the k-vector of the pump. Similar to common demonstrations in linear meta-optics [183–185], this nonlinear beam deflector serves as a canonical example of wavefront control. To achieve this, we arranged the 10-pillar set into a supercell that created a linear phase gradient at the THG wavelength (see Figure 4.4). The supercell was then arranged into a periodic array [see Figure 4.3(a)]. Such a metasurface directs the TH mainly in a direction determined by $|k_x/k_0| = \lambda_{TH}/\left(10 \cdot period\right) = 0.098$, where k_0 and k_x are the full length and in-plane projection of the TH wave-vector, λ_{TH} is the TH wavelength.

We fabricated the nonlinear beam deflector from amorphous silicon on a glass substrate using electron beam lithography (details in Methods: Sample fabrication). An electron microscope

image of the fabricated structure is shown in Figure 4.3(b). To generate the TH signal, we pumped the metasurface at a wavelength of 1615 nm with femtosecond pulses from an optical parametric amplifier pumped by a mode-locked Ytterbium laser. To observe the directionality of the TH and to measure the beam deflection we imaged the back-focal plane onto a camera (details in Methods: nonlinear optics setup). Nearly-perfect TH beam deflection was observed at an angle of $\theta = 5.6°$ (where $\sin(\theta) = |k_x/k_0| = 0.098$) relative to the direction of pump with 92% diffraction efficiency (see Figure 4.5). Importantly, virtually zero TH was generated along the direction of pump (i.e. into the zero diffraction order).

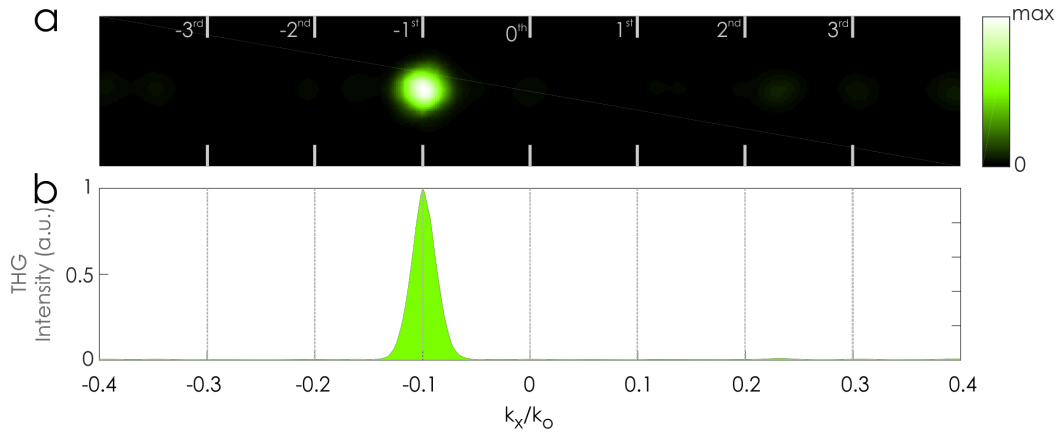

Figure 4.5: Experimental nonlinear beam deflection. (a) Back-focal plane image of forward THG. 92% of THG is directed into the designed angle $\theta = 5.6°$, where k_x/k_0=-0.098. (b) Cross section of experimental back-focal plane image normalized to its maximum.

We then studied the performance of the metasurface as the pump wavelength was tuned from 1330 nm to 1750 nm, the range available from our optical parametric amplifier. Directionality curves, similar to Figure 4.5(b), were experimentally retrieved as the pump wavelength was varied, and then combined into the diagram in Figure 4.6(b). The colour space (HSL colormap) is used to represent the TH directionality and wavelength information where the hue (H) shows true colour of TH for given wavelength, saturation (S) is 1, and lightness (L) corresponds to the normalized TH intensity at each wavelength. The complimentary theoretical calculation is shown in Figure 4.6(a). The calculation took both the amplitudes and phases of the TH into account across the spectral range [shown in Figure 4.6(d)(e)].

We can see that around the optimal wavelength of 1615 nm the only diffraction order clearly visible was the -1st order. As the pump wavelength deviated from its optimal value, other diffraction orders appear in the directionality diagram. From this we could extract the variation of the diffraction efficiency with wavelength by calculating the ratio of power in the -1st order to the summed power in all directions.[see Figure 4.6(c)] . We observe good correspondence between theoretically calculated and experimentally measured diffraction efficiencies of the wavefront control.

Methods

Sample fabrication. The silicon metasurface shown in Figure 4.3 was fabricated on a 4 inch fused silica wafer 500 μm thick. First, a 617 nm polycrystalline silicon layer was deposited onto the substrate by low-pressure chemical vapor deposition (LPCVD). Subsequently, a thin layer of an electron-resist PMMA A4 950 was spin-coated onto the sample, followed by electron-beam lithography (JEOL 100 eV) and development. After this, a 20 nm Cr film was evaporated onto the sample, followed by the lift-off process to generate a Cr mask. Reactive-ion etching (RIE) was used to transfer the Cr mask pattern into the silicon film. Finally, the residual Cr mask was removed via wet Cr etching. Finally, the sample was cleaned with oxygen plasma.

Nonlinear optics setup. For nonlinear optical measurements, we pumped the metasurfaces with an optical parametric amplifier (MIROPA-fs-M from Hotlight Systems) tunable across the range from 1330-1750 nm and generating 300 fs duration pulses at a repetition rate of 21 MHz and average power ranging from 100-300mW. The metasurface was mounted on a three-dimensional stage, and was placed at normal incidence in the focal region of two confocal Olympus Plan N objective lenses. A low-NA lens was used to focus the pump (NA=0.1, 4x). The THG was collected using a lens with NA= 0.4. The beam was focused from the front side of the sample. To detect the TH radiation, we used a cooled CCD camera (Starlight Xpress Ltd, SXVR-H9). The TH signal was separated from the pump using shortpass fil-

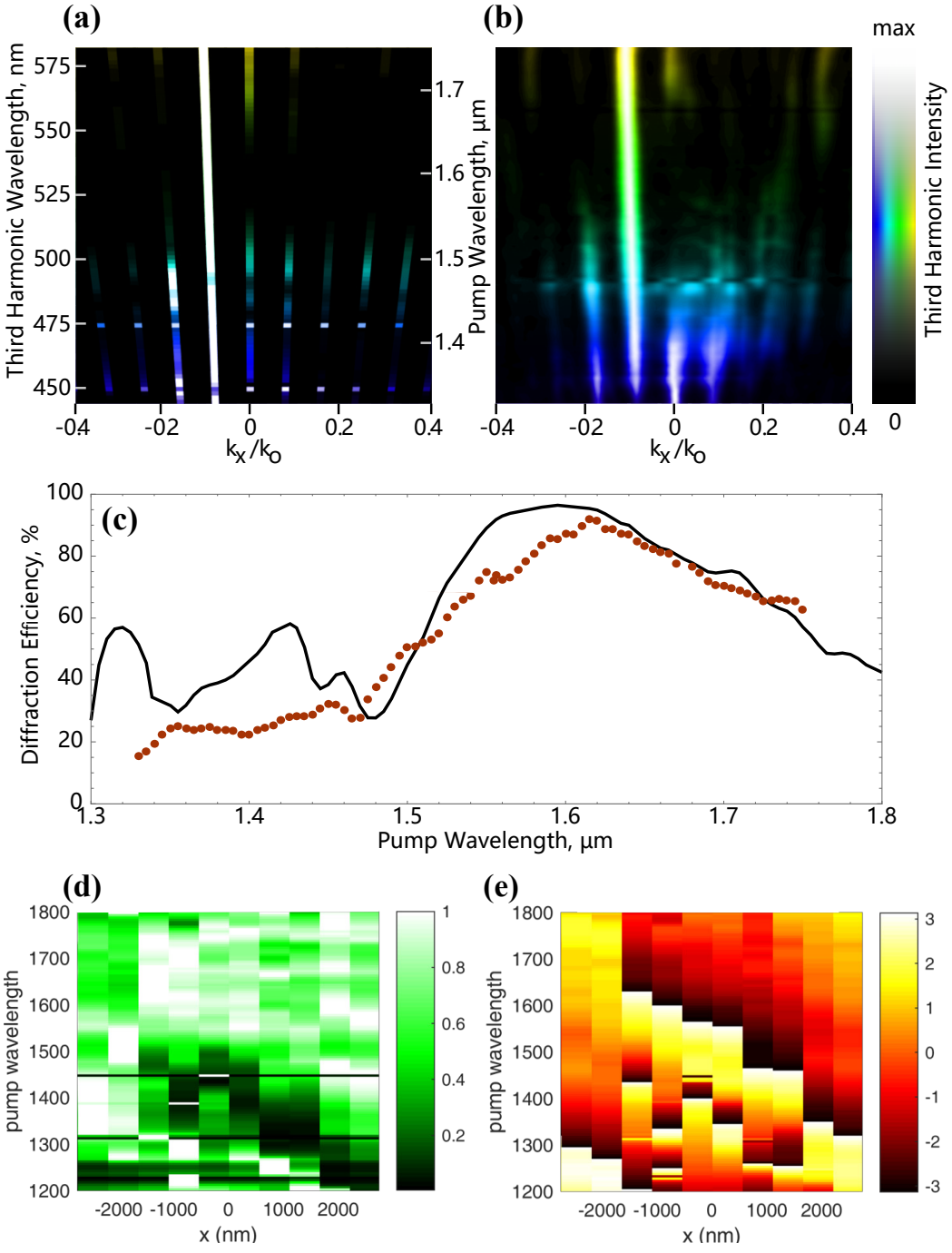

Figure 4.6: Spectral performance of the nonlinear metasurface. (a) Theoretically calculated and (b) experimentally measured directionality diagrams resolved spectrally. Images show true colours of the TH for different wavelength. (c) Diffraction efficiency spectrum defined as the percentage of forward-generated third harmonic directed into the -1st order. Shown are theory (solid) and experiments (dots). Numerical Calculation of the spectral response of the amplitude (d) and phase (e) of the 10 element supercell in the grating.

ter (Thorlabs FESH0650). A pair of confocal lenses were used to transfer the back-focal plane image of the TH radiation onto the camera. The spectrum of the pump beam is cleared up by a dichroic mirror and long-pass infrared filters (Thorlabs FEL 1000 and FELH1150) before the first objective. The setup is similar to what is shown in Figure 3.2.

Numerical calculations. For numerical simulations of the nonlinear amplitudes and phases of the forward-scattered TH wave, we used the finite-element-method solver in COMSOL Multiphysics in the frequency domain. All calculations were realized for a single nanopillar of a specic size on a semi-infinite substrate with periodic boundary conditions mimicking a square array. We employed the approach based on an undepleted pump approximation, using two steps to calculate the radiated nonlinear emission. First, we simulated the linear scattering at the fundamental wavelength, and then obtained the nonlinear polarization induced inside the nanopillar. Then, we employed this as a source for the electromagnetic simulation at the harmonic wavelength to obtain the generated TH field. The nonlinear susceptibility tensor $\chi^{(3)}_{xxxx}$ was considered as a constant scalar value $2.45 \times 10^{-19} m^2/V^2$ [186].

4.3.3 Other Nonlinear Meta-devices

Nonlinear Special Lenses Other functionality of the nonlinear metasurface and be achieved with different types of nonlinear phase profile. For instance we can use the parabolic phase profile Eq. (4.5) described in polar coordinate to create the nonlinear flat lenses Figure 4.7(a)(c).

$$\phi_{donut}(r,\theta) = \frac{2\pi}{\lambda}\left[\sqrt{r^2+f^2} - f\right] + \phi_0 \tag{4.5}$$

By superpositioning a vortex phase profile Eq. (4.6) with the lens, we can control the TH to form a donut beam. The calculated phase mask and the experimentally measured results are as shown in Figure 4.7(b)(d). The propagation of the donut beam is measured by capturing the beam profile in different Z locations.

The results are compiled and shown in Figure 4.7(e).

$$\phi_{donut}(r,\theta) = \frac{2\pi}{\lambda}\left[\sqrt{r^2+f^2}-f\right]+\theta+\phi_0 \tag{4.6}$$

Nonlinear Hologram We also try to create nonlinear holographic display using the same principle described in Section 4.3.1. For such practical application, it is necessary to consider the performance terms of the signal intensity and image quality. From Section 3.2.1 it can be derived that the apparent nonlinear conversion efficiency $\eta = P_{TH}/P_{pump}$ is strongly depending on the peak pump intensity, which is related to the peak pump power P_{pump} and its size R, as shown in Eq. (4.7). β_1 is the coefficient for the cubic relationship.

$$\begin{aligned} I_{TH} &= \beta_1 I_{pump}^3 \\ P_{TH}/R^2 &= \beta_1 P_{pump}^3/R^6 \\ P_{TH} &= \beta_1 P_{pump}^3/R^4 \\ \eta = P_{TH}/P_{pump} &= \beta_1 P_{pump}^2/R^4 \end{aligned} \tag{4.7}$$

From Chapter 2 it is also known that the image quality will be enhanced with large hologram size, which should match the pump beam size R. Therefore the two performance factors, image intensity and quality, has a reciprocal relationship with each other. We can rewrite the equation in respect to the peak pump power in Eq. (4.8). For given nanostructures, the effective nonlinear susceptibility $\chi_{eff}^{(3)}$ is fixed. The CCD sensitivity also have a stable detection sensitivity. Assuming that the hologram can focus the TH signal into a small spot so only the total THG power is related to the detection. Then the peak pump power required in relation to the pump beam size R can be written as $P_{pump} \propto R^{\frac{4}{3}}$, see in Figure 4.8(f). β_2 is the simplification of the coefficients.

$$P_{pump} = \left(\frac{\pi^2 c^2 \varepsilon_0^2}{16}\right)^{\frac{1}{3}} \frac{(P_{TH})^{\frac{1}{3}} R^{\frac{4}{3}}}{\left(\chi_{eff}^{(3)}\right)^{\frac{2}{3}}} = \beta_2 \frac{(P_{TH})^{\frac{1}{3}} R^{\frac{4}{3}}}{\left(\chi_{eff}^{(3)}\right)^{\frac{2}{3}}} \tag{4.8}$$

We can see that with increasing hologram size the pump power requirement is in a 4/3 power relationship. Therefore we fabri-

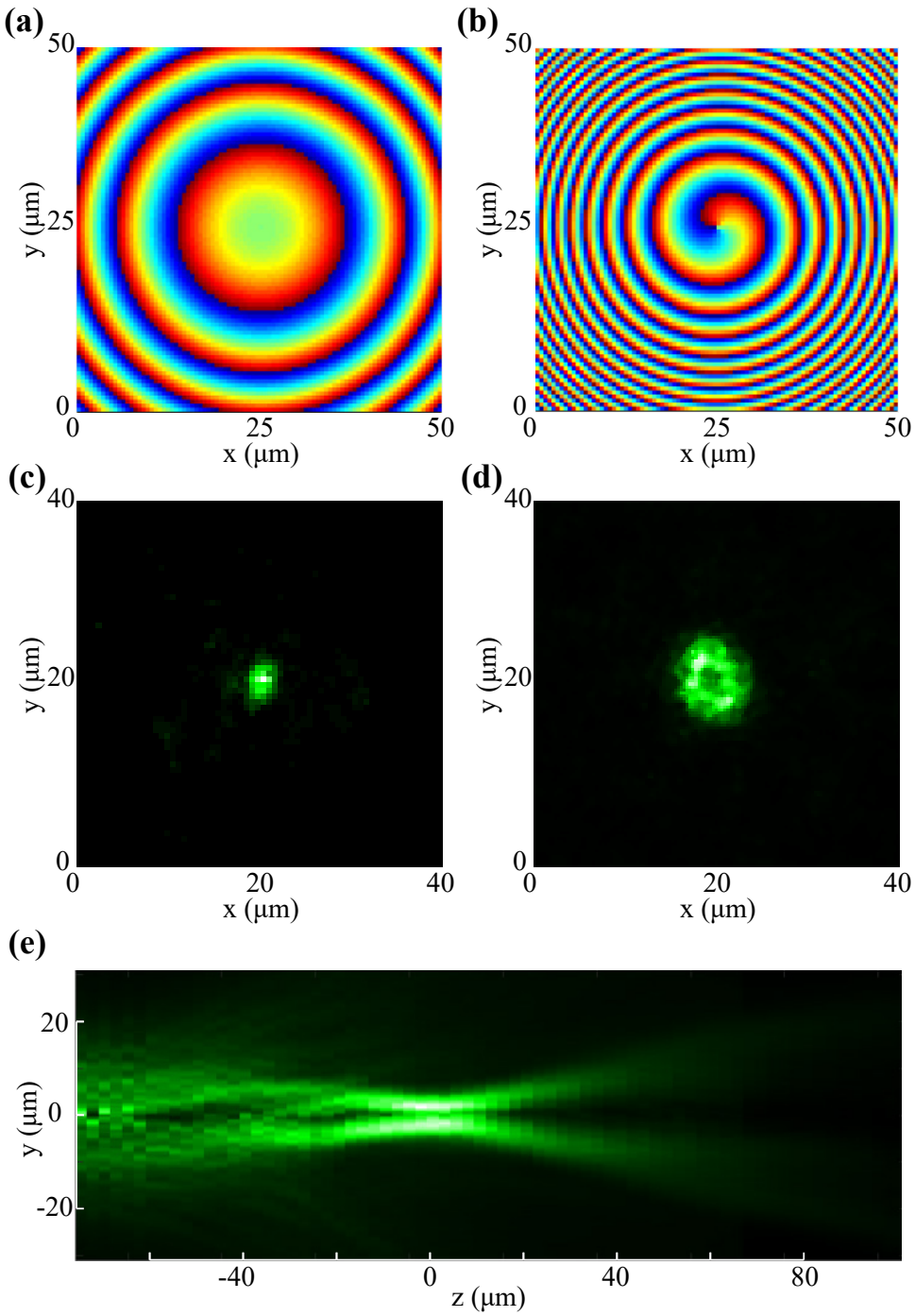

Figure 4.7: Nonlinear special lenses. Theoretically calculated phasemask for nonlinear (a) flat lens and (b) donut beam. Experimentally measured focus spot of the nonlinear lens (c) and donut beam (d). (e)The yz plane cross-section of the TH donut beam, measured by capturing the beam profiles along the propagation axis

cated only a 50x50 resolution nonlinear hologram about 30 μm in dimension as the test sample. Both the Gaussian beam profile and the THG conversion efficiencies are considered in the calculation to create the intensity map shown in Figure 4.8(a). The phasemask is shown in Figure 4.8(c) for generating the smiley face image as predicted in Figure 4.8(d). The experimentally recorded nonlinear hologram display can be found in Figure 4.8(f). The measured result is not perfect but gives a good proof for the functionality of our resonance type of phase modulation in nonlinear processes. Further improvements can be done with more optimization of nanostructures with enhanced $\chi^{(3)}_{eff}$, larger hologram resolution and better fabrication techniques to reduce approximation effects.

Nonlinear Polarization Multiplexing Previous discussion about the nonlinear phase modulation are all based on the same linear polarization for both pump laser and TH signals. However the non-symmetry shape of the elliptical pillar shape will also support polarization multiplexing. To demonstrate this we fabricate a sample that is composed of pillar array of identical shapes that has $1/4\pi$ phase difference and similar amplitude for the THG for vertical and horizontal linear polarized bases. This nonlinear birefringent property should generate circular polarized TH with a linear polarized pump, in a sense similar to quarter waveplate in linear optics. We qualify its performance by measuring the Stokes parameters of the TH and quantified the "roundness" by a goodness function. The goodness function means the higher the function value, the more likely the nonlinear birefringent property should generate circular polarized TH with linear polarized pump. The measured spectral response of the sample is shown in Figure 4.9. The linear polarization of the pump is rotated by an achromatic half waveplate at an angle α. The pump wavelength is tuned with the MIROPA laser. We can see that at certain point in the figure the goodness reached near unity, representing a perfect conversion to circular polarized TH.

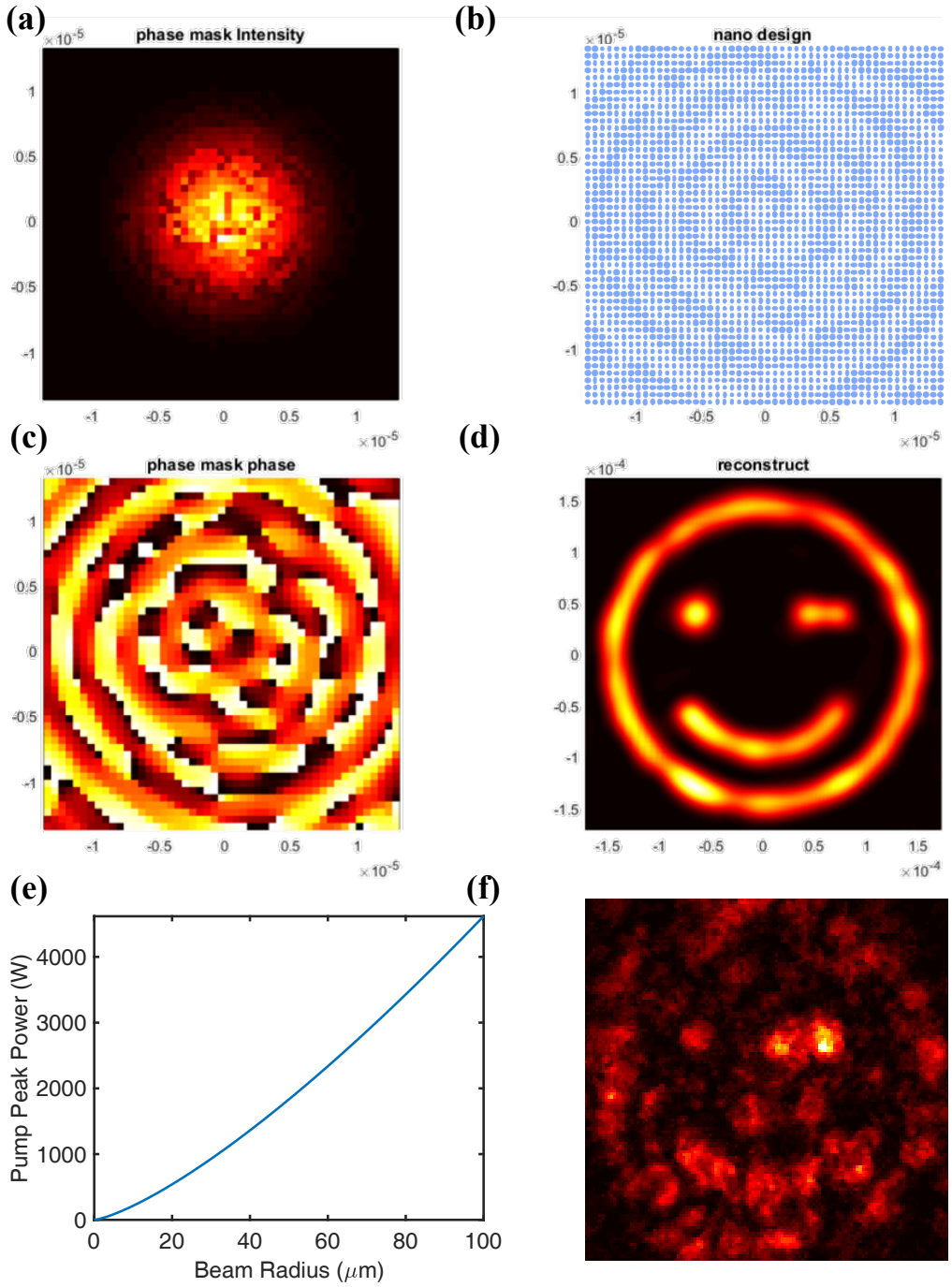

Figure 4.8: Nonlinear hologram. (a) The THG intensity of the hologram considering the Gaussian beam profile as well as the TH efficiency of the nanostructures. (b) Geometries of the nanostructures in the nonlinear meta-hologram. (c) Calculated phasemask for the smiley face display. (d) Predicted image construction. (e) The peak pump power requirement regarding the hologram size. (f) The measured holographic display (a-d unit in meter, f, size not measured)

.

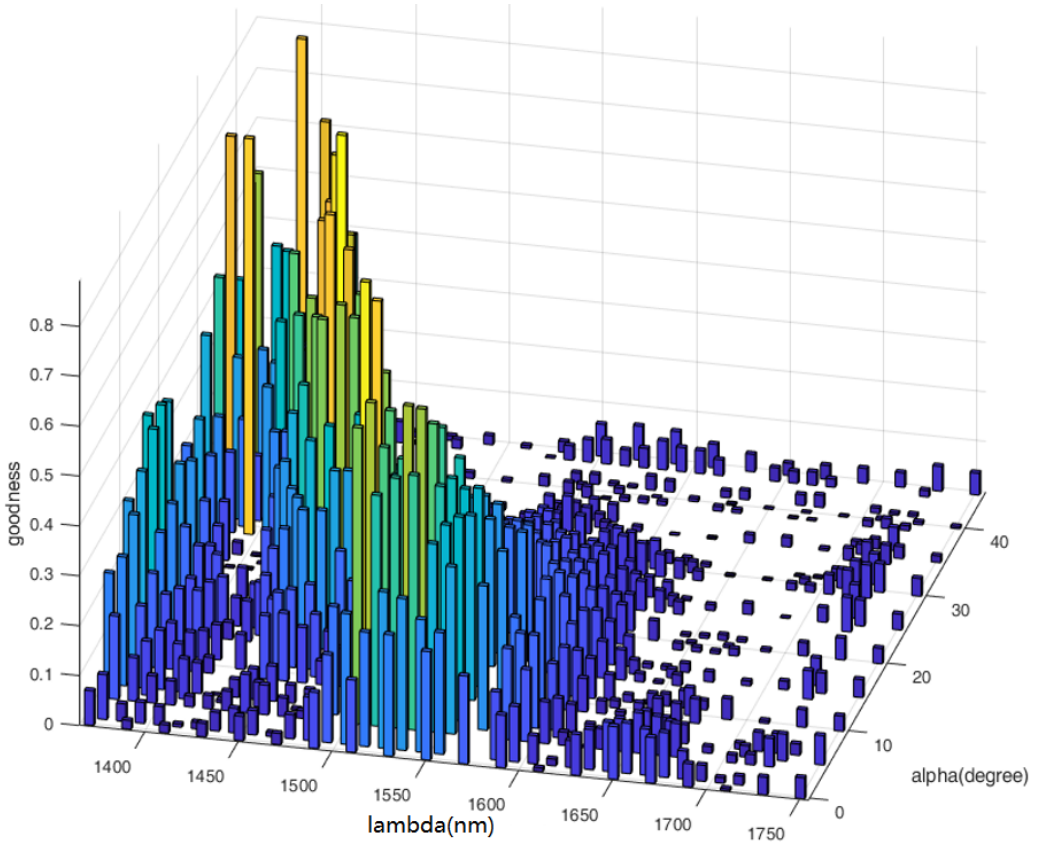

Figure 4.9: Nonlinear polarization multiplexing. The measured goodness of nonlinear quarter waveplate versus pump wavelength and the angle between the linear polarization axis to the sample axis

.

4.4 Summary

We have presented a general theoretical approach and experimental platform for nonlinear wavefront control with highly-efficient nonlinear dielectric metasurfaces. Our approach is based on the generalized Huygens principle extended to nonlinear optics. This allows creating arbitrary phase gradients and wavefronts in nonlinear optics via multipolar nanophotonics, by excitation of electric and magnetic Mie multipoles. Based on our concept, we have designed and demonstrated experimentally the first nonlinear all-dielectric metasurface that generates the third harmonic signal with 92% precision in its wavefront control. Importantly, we suggest a general approach for engineering an arbitrary wavefront of parametric wave generated by a metasurface. It is believed that our results open up new horizons for the development of active and passive optical nanoscale metadevices [16] including low-threshold nanolasers, biosensors, on-chip parametric amplifiers, and nanophotonics quantum circuits.

Conclusion and Outlook

In conclusion, this PhD thesis resolves the key challenges to achieve advanced wavefront control in both linear and nonlinear regimes using all-dielectric metasurfaces. We find out that the generalized Huygens' principle gives the direction of highly efficient meta-atoms for phase modulation. The holographic method can be used to calculate how to assemble the meta-atoms for arbitrary complicated phase profile of the wavefront. The multipolar resonance in all-dielectric metasurfaces can be tuned to enable efficient nonlinear generation as well as full-range phase modulation. These resonances are calculated using AI-guided numerical simulations for nonlinear processes in order to quickly find out the optimized parameters of the nanostructures. The nonlinear optics setup that utilizing confocal microscopy and back focal plane imaging methods can be used to experimentally measure the performances of our metadevices. We experimentally demonstrate our results with broadband spectral measurements and find a good agreement with our theoretic predictions and analyses. The results indicates that our methodology is successful and can be extended to further researches in the future.

The study of advanced wavefront control in linear and nonlinear optics is expected to pave the way to integrated photonic computing and nanophotonic quantum circuitry. Metallic metasurfaces have already been demonstrated to control transmission, reflection, and polarization of light waves, and they offer unique opportunities for functional and ultra-compact photonic structures. All-dielectric metasurfaces have revealed a great potential to advance further the efficiencies and performances of metadevices. Full range phase modulation and near-unity

transmission of meta-atoms can be designed by using the generalized Huygens' principle. Combined with holographic techniques, these meta-atoms can form the advanced and complex wavefront controlling meta-holograms that can be extended to operate in the nonlinear regime. Nonlinear meta-holograms are expected to revolutionize subwavelength photonics by enhancing substantially the nonlinear response of natural materials combined with an efficient control of the phase of a nonlinear wave. Combination of these breakthroughs in linear and nonlinear nanophotonics might incubate the emergence of practical metadevices in cutting-edge technologies.

From optical telecommunication to miniature high-resolution displays, from satellite flat optics to neural endoscope sensors, the applications of holographic metasurfaces are countless as the advanced wavefront control offers an arbitrary beam shape modulation. Optical FFT co-processors, optical matrix operations and photonic neural networks are within the grasp of the meta-holograms. The extension to nonlinear optics can produce efficient photon to photon interactions with the versatile and highly efficient frequency conversions, that can open up the ways to nonreciprocal emissions, quantum-optics channels in three-dimensional space and other applications. A bold prediction can be made that the revolutionary optics computing devices will be achieved with further investigation and investments on the advanced wavefront control in linear and nonlinear optics.

References

1. C. M. Soukoulis and M. Wegener, "Past achievements and future challenges in the development of three-dimensional photonic metamaterials," *Nature Photonics*, vol. 5, pp. 523–530, jul 2011. (cited on page 4)

2. N. Yu and F. Capasso, "Flat optics with designer metasurfaces," *Nature Materials*, vol. 13, pp. 139 EP –, Jan 2014. Review Article. (cited on pages 5, 19, and 77)

3. D. Lin, P. Fan, E. Hasman, and M. L. Brongersma, "Dielectric gradient metasurface optical elements," *Science*, vol. 345, pp. 298–302, jul 2014. (cited on page 5)

4. A. Arbabi, Y. Horie, M. Bagheri, and A. Faraon, "Dielectric metasurfaces for complete control of phase and polarization with subwavelength spatial resolution and high transmission," *Nature Nanotechnology*, vol. 10, pp. 937 EP –, Aug 2015. (cited on pages 5, 6, and 19)

5. S. Kruk, B. Hopkins, I. I. Kravchenko, A. Miroshnichenko, D. N. Neshev, and Y. S. Kivshar, "Invited article: Broadband highly efficient dielectric metadevices for polarization control," *APL Photonics*, vol. 1, p. 030801, jun 2016. (cited on pages 5, 6, 20, 31, and 84)

6. P. Genevet, F. Capasso, F. Aieta, M. Khorasaninejad, and R. Devlin, "Recent advances in planar optics: from plasmonic to dielectric metasurfaces," *Optica*, vol. 4, p. 139, jan 2017. (cited on page 6)

7. N. Yu, P. Genevet, M. A. Kats, F. Aieta, J.-P. Tetienne, F. Capasso, and Z. Gaburro, "Light propagation with phase discontinuities: Generalized laws of reflection and refraction," *Science*, vol. 334, pp. 333–337, sep 2011. (cited on page 7)

8. E. Karimi, S. A. Schulz, I. D. Leon, H. Qassim, J. Upham, and R. W. Boyd, "Generating optical orbital angular momentum at visible wavelengths using a plasmonic metasurface," *Light: Science & Applications*, vol. 3, pp. e167–e167, may 2014. (cited on page 7)

9. G. Zheng, H. Mühlenbernd, M. Kenney, G. Li, T. Zentgraf, and S. Zhang, "Metasurface holograms reaching 80% efficiency," *Nature Nanotechnology*, vol. 10, pp. 308 EP –, Feb 2015. (cited on pages 7 and 19)

10. Y. Yang, I. I. Kravchenko, D. P. Briggs, and J. Valentine, "All-dielectric metasurface analogue of electromagnetically induced transparency," *Nature Communications*, vol. 5, p. 5753, dec 2014. (cited on page 7)

11. M. Khorasaninejad, W. T. Chen, R. C. Devlin, J. Oh, A. Y. Zhu, and F. Capasso, "Metalenses at visible wavelengths: Diffraction-limited focusing and subwavelength resolution imaging," *Science*, vol. 352, pp. 1190–1194, jun 2016. (cited on pages 7 and 41)

12. D. Wen, F. Yue, G. Li, G. Zheng, K. Chan, S. Chen, M. Chen, K. F. Li, P. W. H. Wong, K. W. Cheah, E. Yue Bun Pun, S. Zhang, and X. Chen, "Helicity multiplexed broadband metasurface holograms," *Nature Communications*, vol. 6, pp. 8241 EP –, Sep 2015. Article. (cited on pages 7 and 19)

13. D. Lin, P. Fan, E. Hasman, and M. L. Brongersma, "Dielectric gradient metasurface optical elements," *Science*, vol. 345, pp. 298–302, jul 2014. (cited on pages 6 and 19)

14. P. Albella, R. A. de la Osa, F. Moreno, and S. A. Maier, "Electric and magnetic field enhancement with ultralow heat radiation dielectric nanoantennas: Considerations for surface-enhanced spectroscopies," *ACS Photonics*, vol. 1, pp. 524–529, may 2014. (cited on page 6)

15. S. Jahani and Z. Jacob, "All-dielectric metamaterials," *Nature Nanotechnology*, vol. 11, pp. 23–36, jan 2016. (cited on page 6)

16. N. Zheludev and Y. Kivshar, "From metamaterials to metadevices," *Nature Materials*, vol. 11, no. 11, pp. 917–924, 2012. cited By 594. (cited on pages 6 and 96)

17. G. Li, S. Chen, N. Pholchai, B. Reineke, P. W. H. Wong, E. Y. B. Pun, K. W. Cheah, T. Zentgraf, and S. Zhang, "Continuous control of the nonlinearity phase for harmonic generations," *Nat. Mater.*, vol. 14, no. 6, pp. 607–612, 2015. (cited on pages 6, 56, and 82)

18. E. Almeida, O. Bitton, and Y. Prior, "Nonlinear metamaterials for holography," *Nature Communications*, vol. 7, p. 12533, aug 2016. (cited on pages 6 and 82)

19. M. Tymchenko, J. S. Gomez-Diaz, J. Lee, N. Nookala, M. A. Belkin, and A. Alù, "Gradient nonlinear pancharatnam-berry metasurfaces," *Physical Review Letters*, vol. 115, nov 2015. (cited on pages 6 and 82)

20. E. Almeida, G. Shalem, and Y. Prior, "Subwavelength nonlinear phase control and anomalous phase matching in plasmonic metasurfaces," *Nature Communications*, vol. 7, p. 10367, jan 2016. (cited on pages 6, 9, and 82)

21. S. Keren-Zur, O. Avayu, L. Michaeli, and T. Ellenbogen, "Nonlinear beam shaping with plasmonic metasurfaces," *ACS Photonics*, vol. 3, pp. 117–123, dec 2015. (cited on pages 6 and 82)

22. W. Ye, F. Zeuner, X. Li, B. Reineke, S. He, C.-W. Qiu, J. Liu, Y. Wang, S. Zhang, and T. Zentgraf, "Spin and wavelength multiplexed nonlinear metasurface holography," *Nature Communications*, vol. 7, p. 11930, jun 2016. (cited on pages 6, 9, and 82)

23. M. Kauranen and A. V. Zayats, "Nonlinear plasmonics," *Nat. Photon.*, vol. 6, no. 11, pp. 737–748, 2012. (cited on page 8)

24. M. Celebrano, X. Wu, M. Baselli, S. Großmann, P. Biagioni, A. Locatelli, C. D. Angelis, G. Cerullo, R. Osellame,

B. Hecht, L. Duò, F. Ciccacci, and M. Finazzi, "Mode matching in multiresonant plasmonic nanoantennas for enhanced second harmonic generation," *Nature Nanotech*, vol. 10, pp. 412–417, apr 2015. (cited on pages 8 and 48)

25. J. Lee, M. Tymchenko, C. Argyropoulos, P.-Y. Chen, F. Lu, F. Demmerle, G. Boehm, M.-C. Amann, A. Alù, and M. A. Belkin, "Giant nonlinear response from plasmonic metasurfaces coupled to intersubband transitions," *Nature*, vol. 511, pp. 65–69, jul 2014. (cited on page 8)

26. S. Kruk, M. Weismann, A. Y. Bykov, E. A. Mamonov, I. A. Kolmychek, T. Murzina, N. C. Panoiu, D. N. Neshev, and Y. S. Kivshar, "Enhanced magnetic second-harmonic generation from resonant metasurfaces," *ACS Photon.*, vol. 2, no. 8, pp. 1007–1012, 2015. (cited on pages 9, 50, and 62)

27. M. R. Shcherbakov, D. N. Neshev, B. Hopkins, A. S. Shorokhov, I. Staude, E. V. Melik-Gaykazyan, M. Decker, A. A. Ezhov, A. E. Miroshnichenko, I. Brener, A. A. Fedyanin, and Y. S. Kivshar, "Enhanced third-harmonic generation in silicon nanoparticles driven by magnetic response," *Nano Lett.*, vol. 14, no. 11, pp. 6488–6492, 2014. (cited on pages 9 and 56)

28. B. Hopkins, D. S. Filonov, A. E. Miroshnichenko, F. Monticone, A. Alù, and Y. S. Kivshar, "Interplay of magnetic responses in all-dielectric oligomers to realize magnetic fano resonances," *ACS Photonics*, vol. 2, pp. 724–729, may 2015. (cited on page 9)

29. M. R. Shcherbakov, P. P. Vabishchevich, A. S. Shorokhov, K. E. Chong, D.-Y. Choi, I. Staude, A. E. Miroshnichenko, D. N. Neshev, A. A. Fedyanin, and Y. S. Kivshar, "Ultrafast all-optical switching with magnetic resonances in nonlinear dielectric nanostructures," *Nano Letters*, vol. 15, pp. 6985–6990, sep 2015. (cited on page 9)

30. S. Kruk and Y. Kivshar, "Functional meta-optics and nanophotonics governed by mie resonances," *ACS Photon-*

ics, vol. 4, pp. 2638–2649, nov 2017. (cited on pages 8 and 83)

31. D. Smirnova and Y. Kivshar, "Multipolar nonlinear nanophotonics," *Optica*, vol. 3, no. 11, pp. 1241–1255, 2016. cited By 37. (cited on pages 8, 44, and 63)

32. G. Grinblat, Y. Li, M. P. Nielsen, R. F. Oulton, and S. A. Maier, "Enhanced third harmonic generation in single germanium nanodisks excited at the anapole mode," *Nano Letters*, vol. 16, pp. 4635–4640, jun 2016. (cited on page 8)

33. L. Wang, S. Kruk, L. Xu, M. Rahmani, D. Smirnova, A. Solntsev, I. Kravchenko, D. Neshev, and Y. Kivshar, "Shaping the third-harmonic radiation from silicon nanodimers," *Nanoscale*, vol. 9, no. 6, pp. 2201–2206, 2017. (cited on pages 8 and 44)

34. J. Leuthold, C. Koos, and W. Freude, "Nonlinear silicon photonics," *Nature Photonics*, vol. 4, pp. 535–544, jul 2010. (cited on page 8)

35. Y. Yang, W. Wang, A. Boulesbaa, I. I. Kravchenko, D. P. Briggs, A. Puretzky, D. Geohegan, and J. Valentine, "Nonlinear fano-resonant dielectric metasurfaces," *Nano Letters*, vol. 15, pp. 7388–7393, oct 2015. (cited on page 8)

36. M. Roser and H. Ritchie, "Technological progress." (cited on page 10)

37. "Logic technologies - ibm." (cited on page 11)

38. W. Chen, K. M. Beck, R. Bucker, M. Gullans, M. D. Lukin, H. Tanji-Suzuki, and V. Vuletic, "All-optical switch and transistor gated by one stored photon," *Science*, vol. 341, pp. 768–770, jul 2013. (cited on pages 13 and 14)

39. M.-L. Ren, J. S. Berger, W. Liu, G. Liu, and R. Agarwal, "Strong modulation of second-harmonic generation with very large contrast in semiconducting CdS via high-field domain," *Nature Communications*, vol. 9, jan 2018. (cited on pages 13 and 14)

40. H. Choi, M. Heuck, and D. Englund, "Self-similar nanocavity design with ultrasmall mode volume for single-photon nonlinearities," *Physical Review Letters*, vol. 118, may 2017. (cited on pages 13 and 14)

41. C. Reimer, M. Kues, P. Roztocki, B. Wetzel, F. Grazioso, B. E. Little, S. T. Chu, T. Johnston, Y. Bromberg, L. Caspani, D. J. Moss, and R. Morandotti, "Generation of multiphoton entangled quantum states by means of integrated frequency combs," *Science*, vol. 351, pp. 1176–1180, mar 2016. (cited on pages 13 and 14)

42. Y. Shen, N. C. Harris, S. Skirlo, M. Prabhu, T. Baehr-Jones, M. Hochberg, X. Sun, S. Zhao, H. Larochelle, D. Englund, and M. Soljačić, "Deep learning with coherent nanophotonic circuits," *Nature Photonics*, vol. 11, pp. 441–446, jun 2017. (cited on pages 13 and 15)

43. N. T. Shaked, S. Messika, S. Dolev, and J. Rosen, "Optical solution for bounded NP-complete problems," *Applied Optics*, vol. 46, p. 711, jan 2007. (cited on page 15)

44. A. J. Macfaden, G. S. D. Gordon, and T. D. Wilkinson, "An optical fourier transform coprocessor with direct phase determination," *Scientific Reports*, vol. 7, oct 2017. (cited on page 15)

45. D. GABOR, "A new microscopic principle," *Nature*, vol. 161, pp. 777 EP –, May 1948. (cited on page 19)

46. B. Wang, F. Dong, Q.-T. Li, D. Yang, C. Sun, J. Chen, Z. Song, L. Xu, W. Chu, Y.-F. Xiao, Q. Gong, and Y. Li, "Visible-frequency dielectric metasurfaces for multiwavelength achromatic and highly dispersive holograms," *Nano Letters*, vol. 16, no. 8, pp. 5235–5240, 2016. PMID: 27398793. (cited on page 19)

47. M. Khorasaninejad, A. Ambrosio, P. Kanhaiya, and F. Capasso, "Broadband and chiral binary dielectric metaholograms," *Science Advances*, vol. 2, no. 5, 2016. (cited on page 19)

48. X. Li, L. Chen, Y. Li, X. Zhang, M. Pu, Z. Zhao, X. Ma, Y. Wang, M. Hong, and X. Luo, "Multicolor 3d meta-holography by broadband plasmonic modulation," *Science Advances*, vol. 2, no. 11, 2016. (cited on page 19)

49. A. Arbabi, Y. Horie, A. J. Ball, M. Bagheri, and A. Faraon, "Subwavelength-thick lenses with high numerical apertures and large efficiency based on high-contrast transmitarrays," *Nature Communications*, vol. 6, pp. 7069 EP –, May 2015. Article. (cited on page 19)

50. X. Ni, A. V. Kildishev, and V. M. Shalaev, "Metasurface holograms for visible light," *Nature Communications*, vol. 4, pp. 2807 EP –, Nov 2013. Article. (cited on page 19)

51. L. Huang, X. Chen, H. Mühlenbernd, H. Zhang, S. Chen, B. Bai, Q. Tan, G. Jin, K.-W. Cheah, C.-W. Qiu, J. Li, T. Zentgraf, and S. Zhang, "Three-dimensional optical holography using a plasmonic metasurface," *Nature Communications*, vol. 4, pp. 2808 EP –, Nov 2013. Article. (cited on page 19)

52. J. Lin, P. Genevet, M. A. Kats, N. Antoniou, and F. Capasso, "Nanostructured holograms for broadband manipulation of vector beams," *Nano Letters*, vol. 13, no. 9, pp. 4269–4274, 2013. PMID: 23915192. (cited on page 19)

53. W. T. Chen, K.-Y. Yang, C.-M. Wang, Y.-W. Huang, G. Sun, I.-D. Chiang, C. Y. Liao, W.-L. Hsu, H. T. Lin, S. Sun, L. Zhou, A. Q. Liu, and D. P. Tsai, "High-efficiency broadband meta-hologram with polarization-controlled dual images," *Nano Letters*, vol. 14, no. 1, pp. 225–230, 2014. PMID: 24329425. (cited on page 19)

54. P. Genevet and F. Capasso, "Holographic optical metasurfaces: a review of current progress," *Reports on Progress in Physics*, vol. 78, no. 2, p. 024401, 2015. (cited on page 19)

55. J. B. Herzog, M. W. Knight, and D. Natelson, "Thermoplasmonics: Quantifying plasmonic heating in single

nanowires," *Nano Letters*, vol. 14, pp. 499–503, Feb 2014. (cited on page 19)

56. Z. Liu, W. Hou, P. Pavaskar, M. Aykol, and S. B. Cronin, "Plasmon resonant enhancement of photocatalytic water splitting under visible illumination," *Nano Letters*, vol. 11, pp. 1111–1116, Mar 2011. (cited on page 19)

57. Y. Yang, W. Wang, P. Moitra, I. I. Kravchenko, D. P. Briggs, and J. Valentine, "Dielectric meta-reflectarray for broadband linear polarization conversion and optical vortex generation," *Nano Letters*, vol. 14, pp. 1394–1399, feb 2014. (cited on page 19)

58. J. B. Mueller, N. A. Rubin, R. C. Devlin, B. Groever, and F. Capasso, "Metasurface polarization optics: Independent phase control of arbitrary orthogonal states of polarization," *Physical Review Letters*, vol. 118, mar 2017. (cited on page 19)

59. M. I. Shalaev, J. Sun, A. Tsukernik, A. Pandey, K. Nikolskiy, and N. M. Litchinitser, "High-efficiency all-dielectric metasurfaces for ultracompact beam manipulation in transmission mode," *Nano Letters*, vol. 15, pp. 6261–6266, aug 2015. (cited on page 19)

60. S. Slussarenko, A. Alberucci, C. P. Jisha, B. Piccirillo, E. Santamato, G. Assanto, and L. Marrucci, "Guiding light via geometric phases," *Nature Photonics*, vol. 10, pp. 571–575, aug 2016. (cited on page 19)

61. C. Pfeiffer and A. Grbic, "Metamaterial huygens' surfaces: Tailoring wave fronts with reflectionless sheets," *Physical Review Letters*, vol. 110, may 2013. (cited on page 20)

62. M. Decker, I. Staude, M. Falkner, J. Dominguez, D. N. Neshev, I. Brener, T. Pertsch, and Y. S. Kivshar, "High-efficiency dielectric huygens' surfaces," *Advanced Optical Materials*, vol. 3, pp. 813–820, feb 2015. (cited on pages 20 and 84)

63. K. E. Chong, L. Wang, I. Staude, A. R. James, J. Dominguez, S. Liu, G. S. Subramania, M. Decker, D. N. Neshev, I. Brener,

and Y. S. Kivshar, "Efficient polarization-insensitive complex wavefront control using huygens' metasurfaces based on dielectric resonant meta-atoms," *ACS Photonics*, vol. 3, pp. 514–519, mar 2016. (cited on pages 20, 21, and 38)

64. L. Wang, S. Kruk, H. Tang, T. Li, I. Kravchenko, D. N. Neshev, and Y. S. Kivshar, "Grayscale transparent metasurface holograms," *Optica*, vol. 3, p. 1504, dec 2016. (cited on pages 20, 21, 38, and 84)

65. O. Graydon, "Efficient holograms," *Nature Photonics*, vol. 11, pp. 76–76, feb 2017. (cited on pages 20 and 21)

66. A. I. Kuznetsov, A. E. Miroshnichenko, M. L. Brongersma, Y. S. Kivshar, and B. Luk'yanchuk, "Optically resonant dielectric nanostructures," *Science*, vol. 354, p. aag2472, nov 2016. (cited on pages 20, 38, 62, and 77)

67. E. Gilbert, "Star wars-style holograms one step closer to being in the palm of your hand." (cited on page 21)

68. K. Matsushima and T. Shimobaba, "Band-limited angular spectrum method for numerical simulation of free-space propagation in far and near fields," *Optics Express*, vol. 17, p. 19662, oct 2009. (cited on pages 22 and 24)

69. F. Shen and A. Wang, "Fast-fourier-transform based numerical integration method for the rayleigh-sommerfeld diffraction formula," *Applied Optics*, vol. 45, p. 1102, feb 2006. (cited on page 23)

70. R. Gerchberg and A. Saxton W. O., "A practical algorithm for the determination of phase from image and diffraction plane pictures," vol. 35, pp. 237–250, 11 1971. (cited on page 25)

71. L. Wang, A. Shorokhov, P. Melentiev, S. Kruk, M. Decker, C. Helgert, F. Setzpfandt, A. Fedyanin, Y. Kivshar, and D. Neshev, "Multipolar third-harmonic generation in fishnet metamaterials," *ACS Photonics*, vol. 3, no. 8, pp. 1494–1499, 2016. cited By 9. (cited on pages 44 and 63)

72. R. Camacho-Morales, M. Rahmani, S. Kruk, L. Wang, L. Xu, D. Smirnova, A. Solntsev, A. Miroshnichenko, H. Tan, F. Karouta, S. Naureen, K. Vora, L. Carletti, C. De Angelis, C. Jagadish, Y. Kivshar, and D. Neshev, "Nonlinear generation of vector beams from algaas nanoantennas," *Nano Letters*, vol. 16, no. 11, pp. 7191–7197, 2016. cited By 37. (cited on pages 44, 63, 65, and 73)

73. S. S. Kruk, R. Camacho-Morales, L. Xu, M. Rahmani, D. A. Smirnova, L. Wang, H. H. Tan, C. Jagadish, D. N. Neshev, and Y. S. Kivshar, "Nonlinear optical magnetism revealed by second-harmonic generation in nanoantennas," *Nano Letters*, vol. 17, pp. 3914–3918, may 2017. (cited on pages 44 and 73)

74. M. Lippitz, M. A. van Dijk, and M. Orrit, "Third-harmonic generation from single gold nanoparticles," *Nano Lett.*, vol. 5, pp. 799–802, apr 2005. (cited on page 45)

75. L. Novotny and B. Hecht, *Principles of Nano-Optics*. New York: Cambridge University Press, 2007. (cited on pages 45 and 72)

76. M. Kasperczyk, S. Person, D. Ananias, L. D. Carlos, and L. Novotny, "Excitation of magnetic dipole transitions at optical frequencies," *Phys. Rev. Lett.*, vol. 114, apr 2015. (cited on page 45)

77. J. Jackson, *Classical electrodynamics*. Moskow: Mir, 1965. (cited on pages 46 and 47)

78. C. F. Bohren and D. R. Huffman, *Absorption and Scattering of Light by Small Particles*. New York: Wiley, 1983. (cited on page 46)

79. J. I. Dadap, J. Shan, and T. F. Heinz, "Theory of optical second-harmonic generation from a sphere of centrosymmetric material: small-particle limit," *J. Opt. Soc. Am. B*, vol. 21, no. 7, p. 1328, 2004. (cited on page 46)

80. J. Petschulat, A. Chipouline, A. Tünnermann, T. Pertsch, C. Menzel, C. Rockstuhl, and F. Lederer, "Multipole non-

linearity of metamaterials," *Phys. Rev. A*, vol. 80, p. 063828, dec 2009. (cited on page 46)

81. S. Mühlig, C. Menzel, C. Rockstuhl, and F. Lederer, "Multipole analysis of meta-atoms," *Metamaterials*, vol. 5, pp. 64–73, jun 2011. (cited on page 46)

82. G. Gonella and H.-L. Dai, "Determination of adsorption geometry on spherical particles from nonlinear Mie theory analysis of surface second harmonic generation," *Phys. Rev. B*, vol. 84, p. 121402, sep 2011. (cited on page 46)

83. P. Grahn, A. Shevchenko, and M. Kaivola, "Electromagnetic multipole theory for optical nanomaterials," *New J. Phys.*, vol. 14, p. 093033, sep 2012. (cited on page 46)

84. W. Liu, A. E. Miroshnichenko, D. N. Neshev, and Y. S. Kivshar, "Broadband unidirectional scattering by magnetoelectric core–shell nanoparticles," *ACS Nano*, vol. 6, pp. 5489–5497, jun 2012. (cited on page 47)

85. S. G. Rodrigo, H. Harutyunyan, and L. Novotny, "Coherent control of light scattering from nanostructured materials by second-harmonic generation," *Phys. Rev. Lett.*, vol. 110, p. 177405, apr 2013. (cited on page 47)

86. I. Staude, A. E. Miroshnichenko, M. Decker, N. T. Fofang, S. Liu, E. Gonzales, J. Dominguez, T. S. Luk, D. N. Neshev, I. Brener, and Y. Kivshar, "Tailoring directional scattering through magnetic and electric resonances in subwavelength silicon nanodisks," *ACS Nano*, vol. 7, pp. 7824–7832, sep 2013. (cited on pages 47 and 63)

87. Y. H. Fu, A. I. Kuznetsov, A. E. Miroshnichenko, Y. F. Yu, and B. Luk'yanchuk, "Directional visible light scattering by silicon nanoparticles," *Nat. Commun.*, vol. 4, p. 1527, feb 2013. (cited on pages 47 and 63)

88. E. Poutrina, A. Rose, D. Brown, A. Urbas, and D. R. Smith, "Forward and backward unidirectional scattering from plasmonic coupled wires," *Opt. Express*, vol. 21, no. 25, p. 31138, 2013. (cited on page 47)

89. A. E. Krasnok, C. R. Simovski, P. A. Belov, and Y. S. Kivshar, "Superdirective dielectric nanoantennas," *Nanoscale*, vol. 6, no. 13, p. 7354, 2014. (cited on page 47)

90. D. A. Smirnova, I. V. Shadrivov, A. E. Miroshnichenko, A. I. Smirnov, and Y. S. Kivshar, "Second-harmonic generation by a graphene nanoparticle," *Phys. Rev. B*, vol. 90, p. 035412, jul 2014. (cited on page 47)

91. R. B. Davidson II, J. I. Ziegler, G. Vargas, S. M. Avanesyan, Y. Gong, W. Hess, and R. F. Haglund Jr., "Efficient forward second-harmonic generation from planar archimedean nanospirals," *Nanophotonics*, vol. 4, p. 2, jan 2015. (cited on page 47)

92. D. Dregely, K. Lindfors, M. Lippitz, N. Engheta, M. Totzeck, and H. Giessen, "Imaging and steering an optical wireless nanoantenna link," *Nat. Commun.*, vol. 5, p. 5354, jul 2014. (cited on page 47)

93. I. Liberal, I. Ederra, R. Gonzalo, and R. W. Ziolkowski, "Superbackscattering from single dielectric particles," *J. Opt.*, vol. 17, p. 072001, jun 2015. (cited on page 47)

94. M. Kerker, D.-S. Wang, and C. L. Giles, "Electromagnetic scattering by magnetic spheres," *J. Opt. Soc. Am. B*, vol. 73, no. 6, p. 765, 1983. (cited on page 47)

95. W. Liu, J. Zhang, B. Lei, H. Ma, W. Xie, and H. Hu, "Ultra-directional forward scattering by individual core-shell nanoparticles," *Opt. Express*, vol. 22, no. 13, p. 16178, 2014. (cited on page 47)

96. I. M. Hancu, A. G. Curto, M. Castro-López, M. Kuttge, and N. F. van Hulst, "Multipolar interference for directed light emission," *Nano Lett.*, vol. 14, pp. 166–171, jan 2014. (cited on page 47)

97. R. R. Naraghi, S. Sukhov, and A. Dogariu, "Directional control of scattering by all-dielectric core-shell spheres," *Opt. Lett.*, vol. 40, no. 4, p. 585, 2015. (cited on page 47)

98. R. Alaee, R. Filter, D. Lehr, F. Lederer, and C. Rockstuhl, "A generalized kerker condition for highly directive nanoantennas," *Opt. Lett.*, vol. 40, no. 11, p. 2645, 2015. (cited on page 47)

99. J. Li, N. Verellen, D. Vercruysse, T. Bearda, L. Lagae, and P. V. Dorpe, "All-dielectric antenna wavelength router with bidirectional scattering of visible light," *Nano Letters*, vol. 16, pp. 4396–4403, June 2016. (cited on pages 47 and 52)

100. S. Roke, M. Bonn, and A. V. Petukhov, "Nonlinear optical scattering: The concept of effective susceptibility," *Phys. Rev. B*, vol. 70, p. 115106, sep 2004. (cited on page 47)

101. K. O'Brien, H. Suchowski, J. Rho, A. Salandrino, B. Kante, X. Yin, and X. Zhang, "Predicting nonlinear properties of metamaterials from the linear response," *Nat. Mater.*, vol. 14, pp. 379–383, feb 2015. (cited on pages 47 and 48)

102. D. A. Smirnova, A. B. Khanikaev, L. A. Smirnov, and Y. S. Kivshar, "Multipolar third-harmonic generation driven by optically induced magnetic resonances," *ACS Photonics*, may 2016. (cited on page 48)

103. R. W. Boyd, *Nonlinear Optics, 3rd ed.* New York: Elsevier, 2008. (cited on page 48)

104. K. Thyagarajan, S. Rivier, A. Lovera, and O. J. Martin, "Enhanced second-harmonic generation from double resonant plasmonic antennae," *Opt. Express*, vol. 20, p. 12860, may 2012. (cited on page 48)

105. M. Navarro-Cia and S. A. Maier, "Broad-band near-infrared plasmonic nanoantennas for higher harmonic generation," *ACS Nano*, vol. 6, pp. 3537–3544, apr 2012. (cited on page 48)

106. H. Aouani, M. Navarro-Cia, M. Rahmani, T. P. H. Sidiropoulos, M. Hong, R. F. Oulton, and S. A. Maier, "Multiresonant broadband optical antennas as efficient tunable nanosources of second harmonic light," *Nano Lett.*, vol. 12, pp. 4997–5002, sep 2012. (cited on page 48)

107. P. Ginzburg, A. Krasavin, Y. Sonnefraud, A. Murphy, R. J. Pollard, S. A. Maier, and A. V. Zayats, "Nonlinearly coupled localized plasmon resonances: Resonant second-harmonic generation," *Phys. Rev. B*, vol. 86, p. 085422, aug 2012. (cited on page 48)

108. F. Bassani and V. Lucarini, "General properties of optical harmonic generation from a simple oscillator model," *Nouv Cim D*, vol. 20, pp. 1117–1125, jul 1998. (cited on page 48)

109. E. Poutrina, D. Huang, Y. Urzhumov, and D. R. Smith, "Nonlinear oscillator metamaterial model: numerical and experimental verification," *Opt. Express*, vol. 19, p. 8312, apr 2011. (cited on page 48)

110. R. C. Miller, "Optical second harmonic generation in piezoelectric crystals," *Appl. Phys. Lett.*, vol. 5, no. 1, p. 17, 1964. (cited on page 48)

111. C. Garrett and F. Robinson, "Miller's phenomenological rule for computing nonlinear susceptibilities," *IEEE J. Quantum Electron*, vol. 2, pp. 328–329, aug 1966. (cited on page 48)

112. J. Butet and O. J. F. Martin, "Evaluation of the nonlinear response of plasmonic metasurfaces: Miller's rule, nonlinear effective susceptibility method, and full-wave computation," *J. Opt. Soc. Am. B*, vol. 33, p. A8, dec 2015. (cited on page 48)

113. M. Hentschel, T. Utikal, H. Giessen, and M. Lippitz, "Quantitative modeling of the third harmonic emission spectrum of plasmonic nanoantennas," *Nano Lett.*, vol. 12, pp. 3778–3782, jul 2012. (cited on page 48)

114. B. Metzger, M. Hentschel, M. Lippitz, and H. Giessen, "Third-harmonic spectroscopy and modeling of the nonlinear response of plasmonic nanoantennas," *Opt. Lett.*, vol. 37, p. 4741, nov 2012. (cited on page 48)

115. B. Metzger, T. Schumacher, M. Hentschel, M. Lippitz, and H. Giessen, "Third harmonic mechanism in complex plas-

monic Fano structures," *ACS Photonics*, vol. 1, pp. 471–476, jun 2014. (cited on page 48)

116. R. Czaplicki, J. Mäkitalo, R. Siikanen, H. Husu, J. Lehtolahti, M. Kuittinen, and M. Kauranen, "Second-harmonic generation from metal nanoparticles: Resonance enhancement versus particle geometry," *Nano Lett.*, vol. 15, pp. 530–534, jan 2015. (cited on page 48)

117. D. de Ceglia, M. A. Vincenti, C. D. Angelis, A. Locatelli, J. W. Haus, and M. Scalora, "Role of antenna modes and field enhancement in second harmonic generation from dipole nanoantennas," *Opt. Express*, vol. 23, p. 1715, jan 2015. (cited on page 48)

118. G. D. Bernasconi, J. Butet, and O. J. F. Martin, "Mode analysis of second-harmonic generation in plasmonic nanostructures," *J. Opt. Soc. Am. B*, vol. 33, p. 768, mar 2016. (cited on page 48)

119. C. Ciracì, E. Poutrina, M. Scalora, and D. R. Smith, "Origin of second-harmonic generation enhancement in optical split-ring resonators," *Phys. Rev. B*, vol. 85, p. 201403, May 2012. (cited on page 50)

120. E. Poutrina, D. Huang, Y. Urzhumov, and D. R. Smith, "Nonlinear oscillator metamaterial model: numerical and experimental verification," *Opt. Express*, vol. 19, pp. 8312–8319, Apr 2011. (cited on page 50)

121. S. Kujala, B. K. Canfield, M. Kauranen, Y. Svirko, and J. Turunen, "Multipole interference in the second-harmonic optical radiation from gold nanoparticles," *Phys. Rev. Lett.*, vol. 98, p. 167403, Apr 2007. (cited on page 50)

122. G. Bachelier, I. Russier-Antoine, E. Benichou, C. Jonin, and P.-F. Brevet, "Multipolar second-harmonic generation in noble metal nanoparticles," *J. Opt. Soc. Am. B*, vol. 25, pp. 955–960, Jun 2008. (cited on page 50)

123. M. Zdanowicz, S. Kujala, H. Husu, and M. Kauranen, "Effective medium multipolar tensor analysis of second-

harmonic generation from metal nanoparticles," *New J. Phys.*, vol. 13, no. 2, p. 023025, 2011. (cited on page 50)

124. M. J. Huttunen, J. Mäkitalo, G. Bautista, and M. Kauranen, "Multipolar second-harmonic emission with focused gaussian beams," *New J. Phys.*, vol. 14, no. 11, p. 113005, 2012. (cited on page 50)

125. F. A. Bovino, M. C. Larciprete, C. Sibilia, G. Váró, and C. Gergely, "Evidence of multipolar response of bacteriorhodopsin by noncollinear second harmonic generation," *Opt. Express*, vol. 20, pp. 14621–14631, Jun 2012. (cited on page 50)

126. T. H. Taminiau, S. Karaveli, N. F. van Hulst, and R. Zia, "Quantifying the magnetic nature of light emission," *Nat. Commun.*, vol. 3, p. 979, 2012. (cited on page 52)

127. I. M. Hancu, A. G. Curto, M. Castro-López, M. Kuttge, and N. F. van Hulst, "Multipolar interference for directed light emission," *Nano Lett.*, vol. 14, no. 1, pp. 166–171, 2014. (cited on page 52)

128. S. S. Kruk, M. Decker, I. Staude, S. Schlecht, M. Greppmair, D. N. Neshev, and Y. S. Kivshar, "Spin-polarized photon emission by resonant multipolar nanoantennas," *ACS Photon.*, vol. 1, no. 11, pp. 1218–1223, 2014. (cited on page 52)

129. D. Vercruysse, X. Zheng, Y. Sonnefraud, N. Verellen, G. D. Martino, L. Lagae, G. A. E. Vandenbosch, V. V. Moshchalkov, S. A. Maier, and P. V. Dorpe, "Directional fluorescence emission by individual v-antennas explained by mode expansion," *ACS Nano*, vol. 8, pp. 8232–8241, July 2014. (cited on page 52)

130. K. Bennemann, *Non-linear Optics in Metals*. International Series of Monographs on Physics, Clarendon Press, 1998. (cited on page 52)

131. J. I. Dadap, J. Shan, K. B. Eisenthal, and T. F. Heinz, "Second-harmonic rayleigh scattering from a sphere of centrosym-

metric material," *Phys. Rev. Lett.*, vol. 83, pp. 4045–4048, Nov 1999. (cited on page 52)

132. E. Makeev and S. Skipetrov, "Second harmonic generation in suspensions of spherical particles," *Opt. Commun.*, vol. 224, no. 1, pp. 139 – 147, 2003. (cited on page 52)

133. J. Mäkitalo, S. Suuriniemi, and M. Kauranen, "Enforcing symmetries in boundary element formulation of plasmonic and second-harmonic scattering problems," *J. Opt. Soc. Am. A*, vol. 31, pp. 2821–2832, Dec 2014. (cited on page 52)

134. D. A. Smirnova, A. B. Khanikaev, L. A. Smirnov, and Y. S. Kivshar, "Multipolar third-harmonic generation driven by optically-induced magnetic resonances," *ArXiv:physics.optics*, p. 1456313, 2016. (cited on page 52)

135. S. Viarbitskaya, O. Demichel, B. Cluzel, G. Colas des Francs, and A. Bouhelier, "Delocalization of nonlinear optical responses in plasmonic nanoantennas," *Phys. Rev. Lett.*, vol. 115, p. 197401, Nov 2015. (cited on page 52)

136. D. Wolf, T. Schumacher, and M. Lippitz, "Shaping the nonlinear near field," *Nat. Commun.*, vol. 7, p. 10361, 2016. (cited on page 52)

137. S. Zhang, W. Fan, N. C. Panoiu, K. J. Malloy, R. M. Osgood, and S. R. J. Brueck, "Experimental demonstration of near-infrared negative-index metamaterials," *Phys. Rev. Lett.*, vol. 95, p. 137404, Sep 2005. (cited on page 52)

138. G. Dolling, C. Enkrich, M. Wegener, C. M. Soukoulis, and S. Linden, "Simultaneous negative phase and group velocity of light in a metamaterial," *Science*, vol. 312, no. 5775, pp. 892–894, 2006. (cited on page 52)

139. K. M. Dani, Z. Ku, P. C. Upadhya, R. P. Prasankumar, S. R. J. Brueck, and A. J. Taylor, "Subpicosecond optical switching with a negative index metamaterial," *Nano Lett.*, vol. 9, no. 10, pp. 3565–3569, 2009. (cited on page 52)

140. A. Minovich, J. Farnell, D. N. Neshev, I. McKerracher, F. Karouta, J. Tian, D. A. Powell, I. V. Shadrivov, H. Hoe Tan, C. Jagadish, and Y. S. Kivshar, "Liquid crystal based nonlinear fishnet metamaterials," *Appl. Phys. Lett.*, vol. 100, no. 12, p. 121113, 2012. (cited on page 52)

141. E. Kim, F. Wang, W. Wu, Z. Yu, and Y. Shen, "Nonlinear optical spectroscopy of photonic metamaterials," *Phys. Rev. B*, vol. 78, p. 113102, Sep 2008. (cited on page 52)

142. J. Reinhold, M. R. Shcherbakov, A. Chipouline, V. I. Panov, C. Helgert, T. Paul, C. Rockstuhl, F. Lederer, E.-B. Kley, A. Tünnermann, A. A. Fedyanin, and T. Pertsch, "Contribution of the magnetic resonance to the third harmonic generation from a fishnet metamaterial," *Phys. Rev. B*, vol. 86, p. 115401, Sep 2012. (cited on page 52)

143. A. Minovich, D. N. Neshev, D. A. Powell, I. V. Shadrivov, M. Lapine, I. McKerracher, H. T. Hattori, H. H. Tan, C. Jagadish, and Y. S. Kivshar, "Tilted response of fishnet metamaterials at near-infrared optical wavelengths," *Phys. Rev. B*, vol. 81, p. 115109, Mar 2010. (cited on page 53)

144. D. R. Smith, S. Schultz, P. Markoš, and C. M. Soukoulis, "Determination of effective permittivity and permeability of metamaterials from reflection and transmission coefficients," *Phys. Rev. B*, vol. 65, p. 195104, Apr 2002. (cited on pages 54 and 55)

145. S. S. Kruk, Z. J. Wong, E. Pshenay-Severin, K. O'Brien, D. N. Neshev, Y. S. Kivshar, and X. Zhang, "Magnetic hyperbolic optical metamaterials," *Nat. Commun.*, vol. 7, 2016. (cited on page 54)

146. M. Albooyeh, S. Kruk, C. Menzel, C. Helgert, M. Kroll, A. Krysinski, M. Decker, D. N. Neshev, T. Pertsch, C. Etrich, C. Rockstuhl, S. A. Tretyakov, C. R. Simovski, and Y. S. Kivshar, "Resonant metasurfaces at oblique incidence: interplay of order and disorder," *Sci. Reports*, vol. 4, p. 4484, 2014. (cited on page 55)

147. M. Lippitz, M. A. van Dijk, and M. Orrit, "Third-harmonic generation from single gold nanoparticles," *Nano Lett.*, vol. 5, no. 4, pp. 799–802, 2005. (cited on page 56)

148. H. Aouani, M. Rahmani, M. Navarro-Cia, and S. A. Maier, "Third-harmonic-upconversion enhancement from a single semiconductor nanoparticle coupled to a plasmonic antenna," *Nat. Nanotech.*, vol. 9, no. 4, pp. 290–294, 2014. (cited on page 56)

149. B. Metzger, T. Schumacher, M. Hentschel, M. Lippitz, and H. Giessen, "Third harmonic mechanism in complex plasmonic fano structures," *ACS Photon.*, vol. 1, no. 6, pp. 471–476, 2014. (cited on page 56)

150. P. N. Melentiev, A. E. Afanasiev, A. A. Kuzin, V. M. Gusev, O. N. Kompanets, R. O. Esenaliev, and V. I. Balykin, "Split hole resonator: A nanoscale uv light source," *Nano Letters*, vol. 16, no. 2, pp. 1138–1142, 2016. PMID: 26797270. (cited on page 58)

151. J. Jackson, *Classical Electrodynamics*. Wiley, 1998. (cited on page 60)

152. A. Kuznetsov, A. Miroshnichenko, Y. Fu, J. Zhang, and B. Lukyanchukl, "Magnetic light," *Scientific Reports*, vol. 2, 2012. cited By 384. (cited on page 63)

153. P. Albella, T. Shibanuma, and S. Maier, "Switchable directional scattering of electromagnetic radiation with subwavelength asymmetric silicon dimers," *Scientific Reports*, vol. 5, 2015. cited By 25. (cited on page 63)

154. T. Shibanuma, P. Albella, and S. Maier, "Unidirectional light scattering with high efficiency at optical frequencies based on low-loss dielectric nanoantennas," *Nanoscale*, vol. 8, no. 29, pp. 14184–14192, 2016. cited By 14. (cited on page 63)

155. M. Shcherbakov, D. Neshev, B. Hopkins, A. Shorokhov, I. Staude, E. Melik-Gaykazyan, M. Decker, A. Ezhov,

A. Miroshnichenko, I. Brener, A. Fedyanin, and Y. Kivshar, "Enhanced third-harmonic generation in silicon nanoparticles driven by magnetic response," *Nano Letters*, vol. 14, no. 11, pp. 6488–6492, 2014. cited By 156. (cited on page 63)

156. L. Carletti, A. Locatelli, D. Neshev, and C. De Angelis, "Shaping the radiation pattern of second-harmonic generation from algaas dielectric nanoantennas," *ACS Photonics*, vol. 3, no. 8, pp. 1500–1507, 2016. cited By 18. (cited on page 63)

157. V. Gili, L. Carletti, A. Locatelli, D. Rocco, M. Finazzi, L. Ghirardini, I. Favero, C. Gomez, A. Lemaître, M. Celebrano, C. De Angelis, and G. Leo, "Monolithic algaas second-harmonic nanoantennas," *Optics Express*, vol. 24, no. 14, pp. 15965–15971, 2016. cited By 25. (cited on page 63)

158. S. Liu, M. Sinclair, S. Saravi, G. Keeler, Y. Yang, J. Reno, G. Peake, F. Setzpfandt, I. Staude, T. Pertsch, and I. Brener, "Resonantly enhanced second-harmonic generation using iii-v semiconductor all-dielectric metasurfaces," *Nano Letters*, vol. 16, no. 9, pp. 5426–5432, 2016. cited By 41. (cited on page 63)

159. D. Smirnova, A. Khanikaev, L. Smirnov, and Y. Kivshar, "Multipolar third-harmonic generation driven by optically induced magnetic resonances," *ACS Photonics*, vol. 3, no. 8, pp. 1468–1476, 2016. cited By 27. (cited on pages 63, 65, and 72)

160. A. Shorokhov, E. Melik-Gaykazyan, D. Smirnova, B. Hopkins, K. Chong, D.-Y. Choi, M. Shcherbakov, A. Miroshnichenko, D. Neshev, A. Fedyanin, and Y. Kivshar, "Multifold enhancement of third-harmonic generation in dielectric nanoparticles driven by magnetic fano resonances," *Nano Letters*, vol. 16, no. 8, pp. 4857–4861, 2016. cited By 41. (cited on pages 63, 65, 71, and 72)

161. G. Grinblat, Y. Li, M. Nielsen, R. Oulton, and S. Maier, "Enhanced third harmonic generation in single germa-

nium nanodisks excited at the anapole mode," *Nano Letters*, vol. 16, no. 7, pp. 4635–4640, 2016. cited By 40. (cited on page 63)

162. P. Albella, M. Poyli, M. Schmidt, S. Maier, F. Moreno, J. Sáenz, and J. Aizpurua, "Low-loss electric and magnetic field-enhanced spectroscopy with subwavelength silicon dimers," *Journal of Physical Chemistry C*, vol. 117, no. 26, pp. 13573–13584, 2013. cited By 124. (cited on pages 63 and 71)

163. J. Yan, P. Liu, Z. Lin, H. Wang, H. Chen, C. Wang, and G. Yang, "Directional fano resonance in a silicon nanosphere dimer," *ACS Nano*, vol. 9, no. 3, pp. 2968–2980, 2015. cited By 62. (cited on pages 63 and 71)

164. U. Zywietz, M. Schmidt, A. Evlyukhin, C. Reinhardt, J. Aizpurua, and B. Chichkov, "Electromagnetic resonances of silicon nanoparticle dimers in the visible," *ACS Photonics*, vol. 2, no. 7, pp. 913–920, 2015. cited By 49. (cited on pages 63 and 71)

165. S. Kruk, M. Weismann, A. Bykov, E. Mamonov, I. Kolmychek, T. Murzina, N. Panoiu, D. Neshev, and Y. Kivshar, "Enhanced magnetic second-harmonic generation from resonant metasurfaces," *ACS Photonics*, vol. 2, no. 8, pp. 1007–1012, 2015. cited By 34. (cited on page 63)

166. R. Bakker, D. Permyakov, Y. Yu, D. Markovich, R. Paniagua-Domínguez, L. Gonzaga, A. Samusev, Y. Kivshar, B. Lukyanchuk, and A. Kuznetsov, "Magnetic and electric hotspots with silicon nanodimers," *Nano Letters*, vol. 15, no. 3, pp. 2137–2142, 2015. cited By 119. (cited on pages 63, 66, and 72)

167. J. van de Groep, T. Coenen, S. Mann, and A. Polman, "Direct imaging of hybridized eigenmodes in coupled silicon nanoparticles," *Optica*, vol. 3, no. 1, pp. 93–99, 2016. cited By 18. (cited on pages 63 and 71)

168. E. Palik *Handbook of Optical Constants of Solids*, 1985. cited By 17193. (cited on page 65)

169. J. Sipe, D. Moss, and H. Van Driel, "Phenomenological theory of optical second- and third-harmonic generation from cubic centrosymmetric crystals," *Physical Review B*, vol. 35, no. 3, pp. 1129–1141, 1987. cited By 531. (cited on page 66)

170. J. Berthelot, G. Bachelier, M. Song, P. Rai, G. Des Francs, A. Dereux, and A. Bouhelier, "Silencing and enhancement of second-harmonic generation in optical gap antennas," *Optics Express*, vol. 20, no. 10, pp. 10498–10508, 2012. cited By 58. (cited on pages 71 and 72)

171. G. Bernasconi, J. Butet, and O. Martin, "Mode analysis of second-harmonic generation in plasmonic nanostructures," *Journal of the Optical Society of America B: Optical Physics*, vol. 33, no. 4, pp. 768–779, 2016. cited By 18. (cited on pages 71 and 72)

172. J. Butet, S. Dutta-Gupta, and O. Martin, "Surface second-harmonic generation from coupled spherical plasmonic nanoparticles: Eigenmode analysis and symmetry properties," *Physical Review B - Condensed Matter and Materials Physics*, vol. 89, no. 24, 2014. cited By 21. (cited on page 72)

173. M. Lieb, J. Zavislan, and L. Novotny, "Single-molecule orientations determined by direct emission pattern imaging," *Journal of the Optical Society of America B: Optical Physics*, vol. 21, no. 6, pp. 1210–1215, 2004. cited By 217. (cited on page 72)

174. A. Krasnok, M. Tymchenko, and A. Alù, "Nonlinear metasurfaces: a paradigm shift in nonlinear optics," *Materials Today*, vol. 21, pp. 8–21, jan 2018. (cited on pages 77, 79, and 82)

175. I. Staude and J. Schilling, "Metamaterial-inspired silicon nanophotonics," *Nature Photonics*, vol. 11, pp. 274–284, apr 2017. (cited on page 77)

176. D. G. Baranov, D. A. Zuev, S. I. Lepeshov, O. V. Kotov, A. E. Krasnok, A. B. Evlyukhin, and B. N. Chichkov, "All-dielectric nanophotonics: the quest for better materials and fabrication techniques," *Optica*, vol. 4, p. 814, jul 2017. (cited on page 77)

177. V. Egorov, M. Eitan, and J. Scheuer, "Genetically optimized all-dielectric metasurfaces," *Optics Express*, vol. 25, p. 2583, feb 2017. (cited on page 79)

178. J. Hu, C.-H. Liu, X. Ren, L. J. Lauhon, and T. W. Odom, "Plasmonic lattice lenses for multiwavelength achromatic focusing," *ACS Nano*, vol. 10, pp. 10275–10282, oct 2016. (cited on page 79)

179. Y. Rivenson, Y. Zhang, H. Günaydın, D. Teng, and A. Ozcan, "Phase recovery and holographic image reconstruction using deep learning in neural networks," *Light: Science & Applications*, vol. 7, p. 17141, oct 2017. (cited on page 79)

180. M. V. Rybin, K. L. Koshelev, Z. F. Sadrieva, K. B. Samusev, A. A. Bogdanov, M. F. Limonov, and Y. S. Kivshar, "High- q supercavity modes in subwavelength dielectric resonators," *Physical Review Letters*, vol. 119, dec 2017. (cited on page 79)

181. G. Li, S. Zhang, and T. Zentgraf, "Nonlinear photonic metasurfaces," *Nature Reviews Materials*, vol. 2, p. 17010, mar 2017. (cited on pages 79 and 82)

182. L. Wang, S. Kruk, K. Koshelev, I. Kravchenko, B. Luther-Davies, and Y. Kivshar, "Nonlinear wavefront control with all-dielectric metasurfaces," *Nano Letters*, vol. 18, pp. 3978–3984, May 2018. (cited on page 86)

183. Y. F. Yu, A. Y. Zhu, R. Paniagua-Domínguez, Y. H. Fu, B. Luk'yanchuk, and A. I. Kuznetsov, "High-transmission dielectric metasurface with 2 pi phase control at visible wavelengths," *Laser & Photonics Reviews*, vol. 9, pp. 412–418, jun 2015. (cited on page 86)

184. E. Khaidarov, H. Hao, R. Paniagua-Domínguez, Y. F. Yu, Y. H. Fu, V. Valuckas, S. L. K. Yap, Y. T. Toh, J. S. K. Ng, and

A. I. Kuznetsov, "Asymmetric nanoantennas for ultrahigh angle broadband visible light bending," *Nano Letters*, vol. 17, pp. 6267–6272, sep 2017. (cited on page 86)

185. D. Sell, J. Yang, S. Doshay, R. Yang, and J. A. Fan, "Large-angle, multifunctional metagratings based on freeform multimode geometries," *Nano Letters*, vol. 17, pp. 3752–3757, may 2017. (cited on page 86)

186. N. K. Hon, R. Soref, and B. Jalali, "The third-order nonlinear optical coefficients of si, ge, and si1-xGex in the midwave and longwave infrared," *Journal of Applied Physics*, vol. 110, p. 011301, jul 2011. (cited on page 90)